Lehrstuhl E15
Univ.-Prof. Dr. F. von Feilitzsch
Institut für Astro-Teilchenphysik
der Technischen Universität München

Measurement of the Scintillation Light Quenching for Nuclear Recoils induced by Neutron Scattering in Detectors for Dark Matter Particles

Thomas Jagemann

Vollständiger Abdruck der von der Fakultät für Physik der Technischen Universität München zur Erlangung des akademischen Grades eines

Doktors der Naturwissenschaften

genehmigten Dissertation.

Vorsitzender:		Univ.- Prof. Dr. P. Ring
Prüfer der Dissertation:	1.	Univ.- Prof. Dr. F. von Feilitzsch
	2.	Hon.- Prof. Dr. G. Buschhorn

Die Dissertation wurde am 07.12.2004 bei der Technischen Universität München eingereicht und durch die Fakultät für Physik am 13.12.2004 angenommen.

Abstract

Weakly Interacting Massive Particles (WIMPs) have been proposed to constitute the cold dark matter, which is the dominant matter fraction in our galaxy as well as in the universe, at the same time being well motivated by supersymmetric extensions of the standard model of particle physics. Current experiments aiming at the detection of galactic WIMPs base on elastic scattering of WIMPs from atomic nuclei in suitably prepared detectors. The CRESST experiment established the simultaneous measurement of phonons and scintillation light induced by nuclear recoils in $CaWO_4$ crystals. While the different ratios of light yield and energy deposition (so-called Quenching Factors, QF) from electron and nuclear recoils provide a powerful tool for radioactive background discrimination, the individual determination of the Quenching Factors of oxygen, calcium and tungsten in $CaWO_4$ have not been measured so far. This knowledge is essential for the interpretation of the CRESST data in separating the potential WIMP signal from background induced by ambient neutrons.

At the tandem accelerator in Garching, Germany, a neutron scattering facility for the calibration of the detector response to nuclear recoils has been designed, set up and commissioned. A collimated mono-energetic neutron beam with an energy of 11 MeV was produced by an inverse (p,n) reaction. These neutrons are scattered in a central detector whose response to nuclear recoils is under investigation. The scattered neutrons are detected by mobile arrays of 40 neutron detectors in total. The nuclear recoil energy is fixed by fixing the scattering angle, allowing to determine QF as ratio between recoil energy and signal height in the central scintillation detector.

After the operational performance of this facility has been verified by the determination of the Quenching Factors of hydrogen in a NE213 and sodium in a NaI(Tl) scintillation detector at room temperature, for the first time the different Quenching Factors of the elements in the bulk of a $CaWO_4$ crystal were determined separately at room temperature. For the calibration of the Quenching Factors at low temperatures, a dilution refrigerator is integrated in the scattering facility and put into operation.

The objective of this work is the description of the experimental setup of the neutron scattering facility, the determination of Quenching Factors in NE213, NaI(Tl) and $CaWO_4$ scintillators and their relation to characteristics of ion stopping. This dissertation starts with an introduction into the search for Cold Dark Matter Particles, detection methods and the CRESST experiment in Chapter 1. Chapter 2 motivates the need for a detector calibration by neutron scattering and discusses the basic concept of such a scattering experiment. Starting with the planning of a scattering setup and ending with the interpretation of scattering data, a detailed knowledge about the fundamental nuclear reaction processes and their cross sections is mandatory. Chapter 3 gives a summary over the nuclear reaction that are involved, kinematic transformations that are indispensable for scattering calculations are summarized in Appendix A.

The nucleus, recoiling from the neutron deflection, generally leaves its original site together with tightly bound electrons of the inner atomic shells; the so-formed ion collides with atoms of the detector material and generates heat and electronic excitations during its stopping process. The variety of stopping processes together with a calculation of ion ranges and the fraction of ionization and phonons, generated during the slowing down of the ion, are described in Chapter 4. A part of the electronic excitation energy produced within the detector may be transferred to luminescence centres giving rise to a measurable scintillation signal. Scintillation processes for the luminophors used in this work together with a description of quenching processes are described in Chapter 5. After having built the theoretical fundament, the experimental setup is described in detail in Chapter 6: starting with an appropriate choice of a monoenergetic neutron source, the detection of neutrons is described, the geometry of the setup, followed by an explanation of the whole data acquisition assembly. A special section is devoted to the scintillation light detection from $CaWO_4$ due to the complexity of operations involved. With the facility being commissioned, Quenching Factors in NE 213, NaI(Tl) and $CaWO_4$ are measured. These results are presented and discussed in Chapter 7. An outlook with emphasis on the installation of a cryostat for measurements at low temperatures rounds off this work.

Contents

List of Figures

List of Tables

Chapter 1

Introduction

The physical nature of most of the gravitating mass in the universe is completely mysterious. The question of what makes up the mass density of the universe is one of the most fascinating and challenging problems, not only in astrophysics or within the scientific community, but also for wide sections of the population following the progress in this field with close attention and regarding this exciting area as one of the key projects in basic research.

1.1 Dark matter

The astrophysical evidence that luminous matter in the universe (stars, hydrogen clouds, X-ray gas in clusters, etc.) cannot account for the observed gravitationally induced dynamics on galactic scales is virtually as old as extragalactic astronomy [36]. It all started when Zwicky in 1933 derived the velocity dispersion of galaxies in the Coma cluster and estimated the cluster mass with the help of the virial theorem [55]. He concluded that the Coma cluster must contain far more dark than luminous matter, when he translated the luminosity of the galaxies into a corresponding mass. Since then an impressively large number of independent observations established the unavoidable reality of dark matter at a variety of scales (from individual galaxies to galaxy superclusters) and it became canonical that the universe is dominated by unknown forms of dark matter or by unfamiliar classes of dark astrophysical objects. The flat rotation curves of spiral galaxies provide perhaps the most direct and surely a very impressive evidence: the observation differs dramatically from the expectation based on the distribution of the luminous material. This is ascribed to the gravitational effect of dark matter.

A common measure for the contribution of a dark matter component is

its fraction Ω of the critical mass density ρ_c that indicates a flat universe: $\Omega_x = \rho_x/\rho_c$. It has been established that all the luminous matter in the universe is $\Omega_{\rm lum} \lesssim 0.01$ [15].

Models of the physical nature of dark matter are strongly constrained by calculations of big-bang nucleosynthesis. Within the standard big-bang picture the predicted abundances of light elements (e.g. deuterium as the most sensitive measure) depend only on the baryon number density relative to the number density of cosmic microwave background photons. Current results indicate a total (luminous and non-luminous) baryonic fraction $\Omega_{\rm b} = 4.5 \pm 0.5\%$. From primordial adiabatic density perturbations these and other cosmological relevant parameters like the total cosmic matter and energy density have been measured with splendid accuracy by the recent WMAP experiment, yielding a matter contribution to the overall cosmic energy density of only $\Omega_{\rm m} = 27 \pm 4\%$ [50], while $73 \pm 4\%$ are attributed to dark energy. What makes up the nonbaryonic fraction $\Omega_{\rm nbm} = \Omega_{\rm m} - \Omega_{\rm b} \approx 22\%$ remains unresolved to date.

1.2 WIMPs

Galactic phase space arguments together with compatibility studies of large scale cosmic structure formation imply the existence of completely new particles forming cold Dark Matter. A strongly favored class of candidates for this nonbaryonic dark matter are Weakly Interacting Massive Particles (WIMPs). Since several years a second giant branch of physics research has been involved: particle physics. Requiring a more weakly coupling to Z_0 than neutrinos an absolutely new view of physics beyond the particle-physics standard model is scrutinized: Supersymmetry. Supersymmetric extensions of the standard model of particle physics naturally motivate the existence of requisite particles in the form of neutralinos. Normal and supersymmetric particles differ by a quantum number called R-parity which may be conserved so that the lightest supersymmetric particle (LSP) would be stable. If the LSP is the lightest "neutralino", i.e. the lightest mass eigenstate of a general superposition of the neutral spin-$\frac{1}{2}$ fermions expected in this theory, namely the photino, Zino and the two Higgsinos, than we have a perfect theoretical candidate for WIMPs available.

1.3 Searches for Cold Dark Matter Particles

Neutralinos are Majorana fermions. In the early hot phase of the universe they are assumed to be in thermal equilibrium with all other elementary particles and radiation. As the universe expands and cools, the annihilation starts to dominate the reproduction and continues until the decreasing density of the universe makes encounters between Neutralinos improbable (depending on their annihilation cross section). Their cosmic relic density then is determined by freeze-out from thermal equilibrium rather than by an unknown cosmic particle-antiparticle asymmetry. Their interactions would be roughly, but not exactly, of the weak strength. In detail their annihilation and scattering cross sections depend on specific assumptions about a given supersymmetric model. The annihilation cross section is well determined by their required cosmological abundance. Of course the search for supersymmetric particles is one of the prime goals of experiments at future accelerators such as the LHC. The nonobservation of supersymmetric particles at current accelerators places stringent limits on the neutralino mass and interaction cross section. However, the theoretical cross section with respect to quarks (which determines the interaction rate in a dark matter direct detection experiment) is still subject to a considerable theoretical uncertainty, which ranges over at least 5 orders of magnitude, given current experimental constraints.

1.4 Direct detection

In the mid-1980s it became clear that even though WIMPs are by definition weakly interacting particles one can search for them in our galaxy by a variety of methods. The "direct" approach relies on elastic WIMP collisions with the nuclei of a suitable target.

The calculation of cross sections for this interaction is quite complex [12]: starting point is the WIMP–quark interaction, from where nuclear cross sections are derived by means of nuclear form factors. Within a nonrelativistic approximation and the assumption of Majorana type fermions the calculations get simpler and two types of interactions emerge: one is called spin–spin where the WIMP couples to the spin of the nucleus, the other one is called scalar since it only depends on the mass of the nucleus. Generally, the WIMP–nucleus cross section is the sum of these two terms.
The cross section for scalar coupling [12] can be written as

$$\sigma = \frac{4m_r^2}{\pi}[Zf_p + (A - Z)f_n]^2 \tag{1.1}$$

with m_r being defined in (A.32) is the reduced mass; f_p and f_n are coupling constants between neutralino and proton or neutron, respectively. A and Z are the atomic number and the number of protons. For the simplest case of interactions being the same for neutrons and protons, $f_p = f_n$, there will exist a total number of A scattering amplitudes which, for sufficiently low momentum transfer, will add in phase to give a coherent cross section $\propto A^2$ (details in [24]).

1.5 Detection method

Dark Matter WIMPs move with a typical galactic virial velocity of about 270 km/s. If their mass is in the range of 100-1000 GeV their energy transfer in such an elastic collision is expected to be of the order of several 10 keV (cf. Section 2.2). Therefore, the task is to identify such energy depositions in a macroscopic sample of a target material. Of the many ways that have been discussed to achieve this goal, three are of particular importance.

(1) One may search for an ionization signal in a semiconductor, e.g. in a germanium or silicon crystal. However, this approach is fundamentally limited by the absence of discrimination against radioactive background. Not only is it difficult to reject this background even partially, but also it cannot be measured independently of the signal (except by multiple scattering) and subtracted. Once the radioactive background cannot further be reduced, the sensitivity of the experiment does not improve with exposure.

(2) One may search for scintillation light, for example in NaI or in liquid xenon. By the use of pulse shape discrimination one can often distinguish nuclear recoils from electron recoils. Electron recoils stem from cosmic muons or radioactive contaminations of the detectors and their surroundings, they account for the majority of background events. The actual expected WIMP signal are nuclear recoils. The problem of neutron-induced nuclear recoils is discussed below. The DAMA collaboration [3] has recently claimed to having found the WIMP at the upper boundaries of the LSP parameter space by analyzing the annual modulation of a residual spectrum. This modulation signal represents less than 2% of the observed background, and although the group tried hard to control systematics at the required level their WIMP is now excluded partially by the results of an increasing number of competetive collaborations, with CDMS being the leading one. Nevertheless, at present, there are still ways out of this discrepancy since spin-dependent and spin-independent coupling to different target nuclei lead to different weights in cross section contributions. In addition, the origin of the modulated signal, if it was background, is still unknown. After all, the DAMA-WIMP has become

a leading light and stimulus for all other WIMP searches and has significantly contributed to the heat of the current debate. Overall, NaI experiments are susceptible to systematic errors on account of the small number of photoelectrons and the lack of power of pulse shape discrimination at the low energies of interest. Liquified noble gases (such as xenon) also emit scintillation light following particle interactions. A number of collaborations worldwide are constructing and beginning to operate dark matter detectors based on this technology. Initial experiments exploited variations in the scintillation pulse shape to discriminate electron (background) and nuclear (WIMP candidate, or neutron) recoils. Liquid xenon also allows to measure an ionization signal (providing an important tool for background discrimination, see below).

Nevertheless ionization or scintillation detectors suffer generally from low efficiencies for excitations through nuclear recoils (so-called Quenching, Section 2.3) as induced by WIMPs, leading to a minimum energy threshold of only about 20 keV.

(3) In order to address the problem of low efficiencies for scintillation or ionization at low excitation energies, one may focus on the primary WIMP-nucleus interaction in form of the direct reaction of a crystal lattice to nuclear recoils. The first relaxation step of the crystal leads to non-thermal phonons that subsequently decay to ballistic and later thermal phonons (heat). A new kind of detectors is capable to detect these phonons: cryogenic detectors. Here the target (for example a sapphire crystal) is cooled to very low temperatures of the order of 10 mK. Due to the low heat capacity at low temperatures the small amount of energy deposition of either thermal or nonthermal phonons leads to a measurable temperature increase in a thermally coupled thermometer or "bolometer" attached to the crystal. For example, a superconductor attached to the target is shifted toward the normal conducting phase by the temperature rise (see Section 1.7 for further details).

1.6 Background suppression

The main problem with a dark matter direct detection experiment is the extremely low expected signal rate. In detail it depends on the assumed WIMP properties and target material:

$$\dot{N} = N_a \dot{N}_b \, \sigma / F, \tag{1.2}$$

with N_a the number of target atoms with cross section σ, N_b the number of WIMPs penetrating the area F. A typical number is below 0.1 event kg^{-1}

day^{-1}, a counting-rate unit usually employed in this field. To reduce natural radioactive contaminations one has to use extremely pure materials. In addition, to reduce the background caused by cosmic rays requires these experiments to be located in laboratories deeply underground, as in the Soudan mine in Minnesota (USA) with a rock shielding of $\sim$ 2000 mwe or the Gran Sasso underground laboratory in Italy (3600 mwe).

A new idea for an active background discrimination is the combination of two of the three detection methods mentioned above as employed e.g. by the following experiments:

CRESST: **Scintillation** and *Phonons*

CDMS: Ionization and *Phonons*

XENON: **Scintillation** and Ionization

For example, consider a scintillation and phonon measurement: here the original disadvantage of a high quenching (low light yield for nuclear recoils) is suddenly turned into a very powerful discrimination against radioactive gamma- and beta-contamination which induce interactions with the electronic system of the absorber. Since the phonon signal in both cases (electronic or nuclear recoil) is approximately a measure for the total energy deposition, the scintillation signal at a given phonon (total) energy differs markedly and allows for discrimination of nuclear from electronic recoils.

The final limitation for discriminating detectors lies in the neutron background principally generating the same type of nuclear recoil events as WIMPs do. These neutrons stem from spontaneous fission of U-238, other environmental natural radioactive isotopes leading to (α,n) reactions with light elements, or cosmic muons interacting with the shielding rock or with the experimental structure itself. Rn on the detector surfaces contributes not only to an α-particle background, but also by polonium daughter nuclei, being implanted into the crystal surface and slowed down, by maybe looking the same way as recoiling nuclei in the bulk of the detector. Cleanroom operation and a muon veto combined with a passive neutron moderator such as polyethylen, both enclosing the whole experimental setup, fight effectively against this final frontier of exploring the WIMP parameter space.

1.7 The CRESST detector

CRESST [7] has developed cryogenic detectors based on scintillating $CaWO_4$ crystals. A single detector module consists of a 300 g cylindrical crystal,

operated as a cryogenic calorimeter, and a nearby but separate cryogenic detector optimized for the detection of scintillation photons. Since a nucleus and an electron or gamma of the same energy differ substantially in the yield of scintillation light, an effective background discrimination against gammas and electrons is obtained by the simultaneous measurement of the phonon and light signals. Among different scintillating crystals, $CaWO_4$ was selected because of its high light yield at low temperatures and the absence of a noticeable degradation of the light yield for events near the crystal surface, e.g. induced by deliquiscence or suffering from detector processing. Such a degradation, often found in coincident phonon-charge measurements and some scintillators, can cause difficulties as it may lead to a misidentification of electron/photon surface events as nuclear recoils. In addition, the large atomic mass (A = 183.9) of tungsten makes $CaWO_4$ a very favourable target for WIMPs with coherent interactions.

The schematic drawing of the CRESST double detector is shown in Figure 1.1. Phonon and light detector are operated at a temperature of about 10 mK and read out by optimized tungsten superconducting phase transition thermometers. At this temperature the tungsten thermometer is in the middle of its transition between the superconducting and the normal conducting state. Thus a small temperature rise of the thermometer leads to a relatively large rise of its resistance. This resistance ($\sim 0.3\,\Omega$) is measured by means of a two-armed parallel circuit carrying a total constant current of a few μA. One arm of the circuit is given by the superconducting film and the other consists of the input coil of a SQUID in series with a reference resistor (0.05 Ω). This arrangement provides a sensitive measurement of current changes: a rise in the thermometer resistance and such an increase in current through the SQUID coil is then observed as a rise in SQUID output voltage.

The experiment is run at the Laboratori Nazionali del Gran Sasso with a muon flux reduced by 10^6 to about $1/(m^2h)$ and is currently upgraded to enable the operation of 33 detector modules with a total active mass of 10 kg target material. The dual detector is capable of recoil discrimination down to an energy of about 10 keV. For the heaviest nucleus, tungsten, in the absorber crystal, the recoil energy is expected to reach up to about 40 keV, with rates below 0.1 event/(kg day) [7]. However, a reliable statement of WIMP exclusion or detection depends categorically on the knowledge about the detector response to tungsten nuclear recoils which is basically unknown up to now. The object of this work is the presentation of an investigation method to calibrate this response by neutron scattering. An overview about the conception is given in Chapter 2.

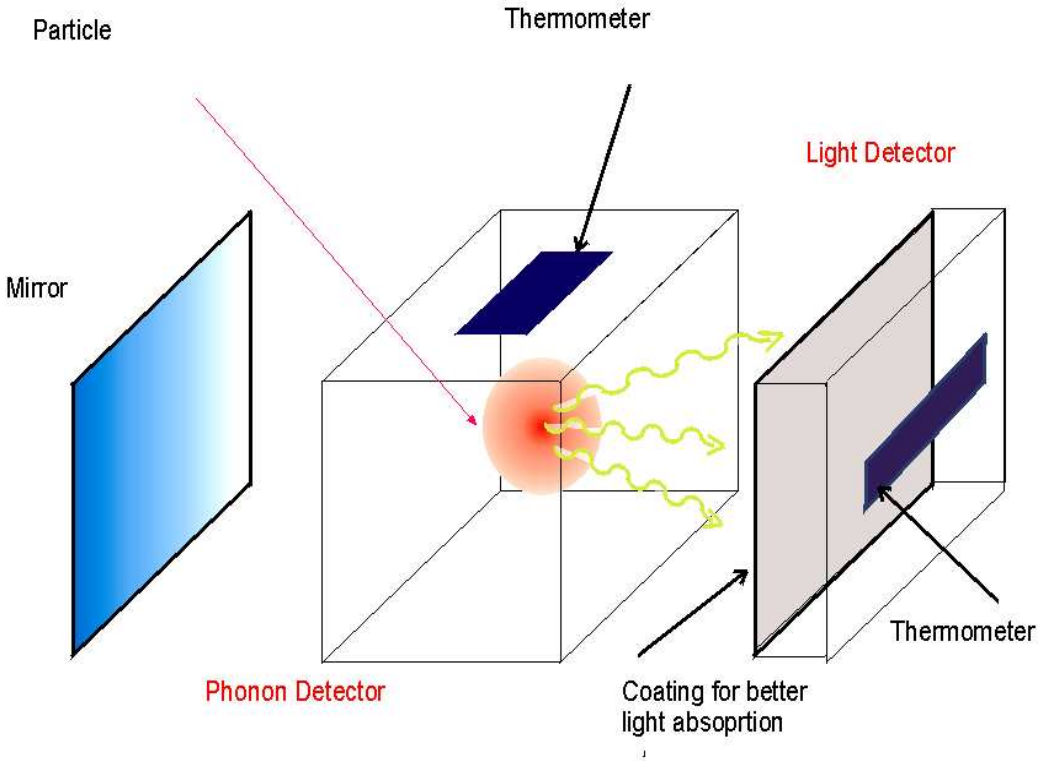

Figure 1.1: Schematic drawing of the CRESST detector: The combination of a cryogenic detector, essentially measuring total energy, and a scintillator, measuring light, can discriminate between nuclear and electron recoils by using the ratio of detected light to thermal energy (details in Section 2.3). The setup consists of two independent detectors. Each uses a tungsten superconducting phase transition thermometer with SQUID readout. The scintillating absorber is a $CaWO_4$ crystal and the light detector is a silicon wafer. The whole setup is surrounded by a reflecting foil for better light collection.

Chapter 2

Conception of the Scattering Experiment

The general task of this calibration experiment is the measurement of Quenching, i.e. the signal suppression occuring for nuclear recoil events as compared to electron recoil events. For the CRESST experiment, the relevant observable quantities are the phonon and the light signals, both originating at the same time from energy deposition of individual nuclear recoils.

2.1 Nuclear Recoil Generation

The stopping of ions in the detector can be studied by various methods:

- the direct bombardment of the detector with ions from an accelerator
- the implantation of α-particle sources on the surface of the detector or the surrounding material [1, 21]. When the α escapes the detector, the response of the detector to the recoiling daughter can be measured accurately.
- nuclear recoil generation by neutron scattering

The first two methods are not adequate if the detector response differs according to whether the interaction occurs close to the surface or in the bulk of the volume. For $CaWO_4$ there is no such severe surface effect as compared to ionization detectors (dead layer, Section 1.7), but up to now no systematic investigations of surface effects and local dependencies are performed. Local enhancements in the defect density, moreover close to the surface, can distort the scintillation yield. Also an effect called primary photon escape can lower the light yield during the dissipation process (Chapter 4).

Another drawback is that the ions are often very different from the detector material.

Neutron interactions have the advantage of occuring rather uniformly throughout the detector volumes. The recoil nuclei thus produced are very similar to those that would be induced by WIMP scattering.

2.2 Neutrons instead of WIMPs

Kinetic energy of a nucleus should be generated without simultaneous primary ionization which is unavoidably the case for bulk α-decay or recoil generation via charged projectiles. In these cases intermingling of scintillation efficiencies makes data interpretation difficult. Thus neutral particles are the best choice for nuclear recoil generation, but up to now we have not got a WIMP source available (which would otherwise be the inherent choice). Therefore, neutrons are used whose generation reactions, properties and detection methods are well known. It must be emphasized that for our purpose the type of interaction (weak in the case of WIMPs or strong in the case of neutrons) does not matter for we are only interested in the result of this interaction, i.e. the detection of the recoiling nucleus by its interaction with the crystalline absorber.

The calibration of WIMP detectors via neutrons should cover the energy range in which WIMP recoils are expected. Since SUSY- proposed WIMP masses are in the 10–1000 GeV range [24], the neutron velocity must be chosen 10–1000 times higher (classical calculation) in order to get the same momentum in the laboratory system. Galactic velocities are of the order of 10^{-3}c, therefore a neutron velocity around 10^{-1}c corresponding to a kinetic energy of the order of 10 MeV (cf. Section A.1) matches the goal. According to Eq. (A.33), typical recoil energies are below 100 keV.

2.3 Quenching

The easiest way to produce fast neutrons is the use of a Californium-251 or an Americium-Beryllium source. The continuous spectrum of the latter one is shown in Figure 7.1.

Figure 2.1 shows the response of the $CaWO_4$ double detector of CRESST to irradiation of gamma rays and neutrons. The light yield of neutron interactions, which in this case is dominated by oxygen recoils, is poorer than the light yield of gamma or beta interaction, i.e. the stopping of a fast electron produces more light than the stopping of a kicked-off nucleus. This effect is

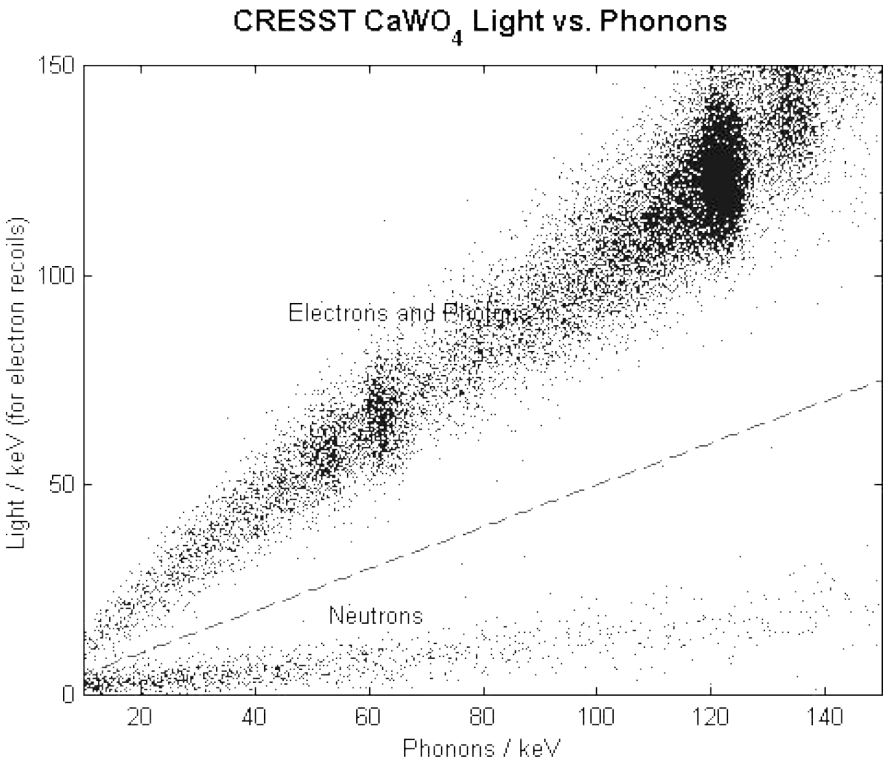

Figure 2.1: The CRESST $CaWO_4$ detector irradiated by a ^{57}Co gamma source (122 and 136 keV), a ^{90}Sr beta source and a ^{241}Am/Be neutron source. Also visible is a typical feature of small detectors: the occurrence of the tungsten $K_{\alpha 1}$ and K_{β_1} escape-lines (59 and 67 keV) originating from the 122 keV Co-line.

The lower light yield for nuclear recoils results in a clear separation of the neutron band from the gamma/beta signature ("electronic recoil band") providing powerful background discrimination. Special attention must be paid to the labels of the axes: Both light and phonon channels are each calibrated using the ^{57}Co lines in the electronic recoil band, i.e., $E_{light}/E_{phonon} \equiv 1$ for this band.

known for all scintillators and also for ionization detectors and is commonly called Quenching.

The basic method for measuring the Quenching factor Q of a detector is the following [39]: First the detector response is obtained using calibrated γ-ray sources. This yields the calibration of the signal amplitude in terms of an electron-equivalent energy, E_{ee}. In a second step, the detector is exposed to a source producing nuclear recoils with a known kinetic energy E_R. The

separation of the nuclear from the electronic recoil band gives rise to the definition of the Quenching factor:

$$QF = \frac{E_{\mathrm{ee}}}{E_{\mathrm{R}}} \tag{2.1}$$

2.4 Signature of Quenching in the CRESST Detector

The objective of a scattering experiment for the calibration of nuclear recoils can now be divided into two parts:

Tungsten Quenching: Considering Equation (1.1), the WIMP interaction cross section for spin independent interaction for different target elements are different, roughly $\sigma \propto A^2$. Thus tungsten recoils in $CaWO_4$ play the dominant role in detecting WIMPs by scalar interaction. Consequently, the Quenching factors of the different elements must be measured separately for confidential claims of the sensitivity of the CRESST experiment.

Heat Quenching: Without an absolute energy calibration it is impossible to exclude energy loss processes in the dissipation process that lead to a signal degradation in the phonon and photon channel of the CRESST detector, e.g. by energy storage in crystal defects or other long-life processes where the excitation energy is not thermalized within a time scale of the read-out [39]. Therefore proof is necessary that the phonon channel calibration from electron recoils also reflects the total energy deposition for nuclear recoils. Hence the question whether the phonon signal may be quenched, too, emphasizes the need for a calibration of the total recoil energy. For clarity, from now on the symbol Q' will be used to represent heat Quenching factors, and Q will be used for ionization or scintillation Quenching factors.

Answers to these challenging questions may likewise offer the opportunity for an enhancement of the performance of the CRESST data interpretation. In the recoil region of WIMP search, i.e. 10 keV $< E_R <$ 40 keV, ambient neutrons scatter from all target elements (see Figure 2.2) whereas WIMPs prefer tungsten. Let Q_O and Q_W be the scintillation Quenching factors of oxygen and tungsten, respectively, in this energy region. We consider the two following cases:

$Q_O \simeq Q_W$: WIMP events are located in the band that was defined beforehand from measurements like the one shown in Figure 2.1 or from ambient neutrons. Since oxygen recoils produce an amount of scintillation light that is well above zero ($Q_O > 0$), all recorded events that show comparatively little or no light at all can be discarded (such events have been observed in earlier CRESST runs and disappeared after a change in the crystal holder). The reduced amount of events in the underground recoil spectrum then increases the sensitivity. On the other hand, ambient neutrons will show the same recoil signature like WIMPs without the possibility of discrimination.

$Q_O > Q_W$: If the oxygen and tungsten recoil bands are well separated, events in the oxygen band provide a monitor for the ambient neutron flux. Converting this event rate to the expected tungsten recoil rate by the known macroscopic cross section ratio (Chapter 3) will break the final background limitation: neutrons that are not suppressed by the muon-veto and having passed all shields. As well, the result is a rise in sensitity of the CRESST setup. On the other hand, the separation of WIMP recoils from artificial signals (e.g. cracks) that produce no light is impossible.

In the following sections we will gradually investigate experimental conditions that allow the discrimination of different recoiling nuclei in $CaWO_4$ as well as a possible energy dependence of Quenching. Nuclear recoils will be generated by neutron scattering. We will start the discussion with a simple setup of a fast responding detector irradiated by a continuous neutron source. The complexity of the setup is raised when in the next steps slow detectors are used, inelastic scattering and accidental coincidences are taken into account, and when (at room temperature) only the scintillation light is measured instead of a combination of phonon and light signals. These complications require the use of a mono-energetic neutron source in order to fix the input energy, pulsing of the neutrons to establish time-of-flight measurements and fixing the recoil angle to correlate the energy transfer to the nuclei with the input energy of the neutrons.

2.5 Continuous spectrum

Now without any further experimental demands (like timing information, e.g.) let a neutron spectrum like the one shown in Figure 7.1 enter a crystal whose response is to be calibrated (in the following called “central detector”).

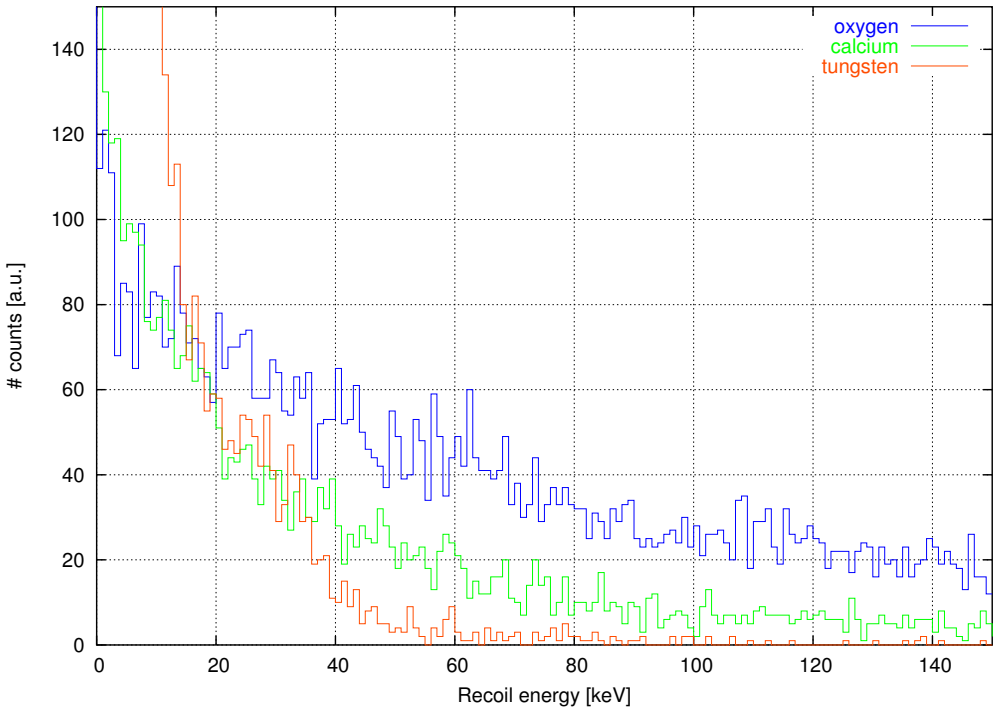

Figure 2.2: Simulated spectrum of a 40×40 mm^3 cylindrical $CaWO_4$–crystal irradiated by neutrons from an Am-Be source. The relative contribution of the different elements may also serve as an indication of neutron induced recoil spectra from (α,n) reactions in underground runs. Multiple scattering and inelastic processes are included, but do not change the characteristics of these spectra. Simulation data are taken from [48]. The respective cross sections are discussed in detail in Chapter 3.

If the measurement includes both light and phonon channels, if the resolution of the light channel is high enough and if the Quenching factor ratios Q/Q' (light to phonon) of the different elements are well separated, then a distribution of events like that in Figure 2.3 is expected. In this way it would be possible to determine the individual ratios of light to phonon Quenching Q/Q', but the (absolute) Quenching factor determination according to Equation (2.1) both in light and heat remains an open question. At present, the light resolution of the CRESST detectors still excludes such precise measurements [42]. However, the stopping of α-particles in the detector indicates a heat Quenching that is close to 1.

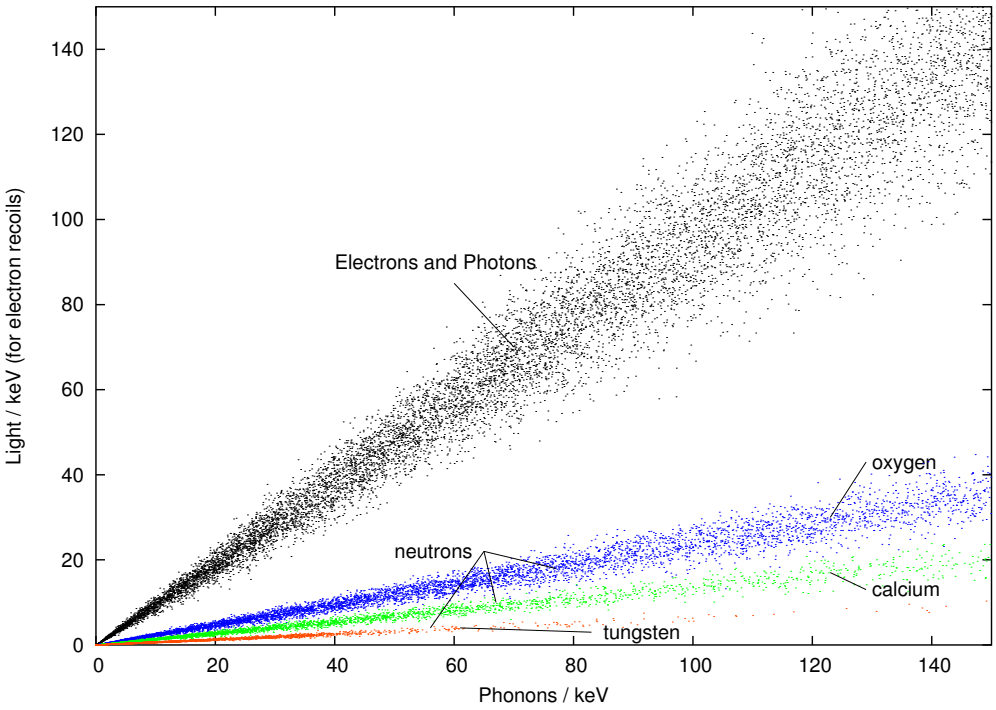

Figure 2.3: Simulated spectrum of a 40×40 mm^3 cylindrical $CaWO_4$–crystal irradiated by neutrons from an Am-Be-source (Figure 7.1). Compare this scatter plot with Figures 2.1 and 2.2. The Quenching factors for calcium and tungsten were chosen to be 0.6 and 0.3, respectively, of the oxygen Quenching factor (independent of energy). Energy resolution of the light channel is assumed to be 15 %. Gammas are randomly distributed by an exponential law, neutron data are taken from [48].

2.6 Monochromaticity of neutrons or Scattering of Neutrons at Fixed Angles?

As of yet the detector response is degenerate because for a certain recoil energy measured, neutrons with different incident energies scattered into different angles contribute: the faster the entering neutron the lower the scattering angle and vice versa for a given recoil energy. This degeneracy is no problem as long as the total recoil energy can be measured, since only the detector response to this recoil energy is of interest, independent on the kinematic details of the recoil generation. In a measurement at room temperature where the total energy deposition is unknown due to the lack of a phonon/heat measurement, the scintillation light measured in the central

detector and the energy of the scattered neutron are the only indicators of the kind of reaction that happened in the central detector. To break up this kinematic degeneracy in the setup two ways are open:

1. The energy of the incident or scattered neutrons can be fixed, allowing for all scattering angles.

2. The scattering angle (for single elastic scattering) can be fixed, allowing for a continuous energy distribution of the incident neutrons.

These two cases will be discussed in the following subsections.

2.6.1 Spectral edge

From Eq. (A.33) we can see that for a grazing incidence in which a neutron is deflected only slightly, the recoiling nucleus is kicked off almost perpendicular to the incoming neutron direction ($\vartheta \cong 90°$), and Eq. (A.33) predicts that the recoil energy is close to zero. At the other extreme, a head-on collision of the incoming neutron with a target nucleus will lead to a recoil in the same direction ($\vartheta \cong 0$), resulting in the maximum possible recoil energy given by Eq. (A.34). Because all scattering angles are allowed, in principle, a continuum of possible recoil energies between these extreme values can be expected. In the simplest case when the scattering process is isotropic in the center-of-mass-coordinate system, the expected recoil energy distribution is a simple rectangle. However, by varying maximum incident neutron energies and identifying the backscattering angle uniquely by the spectral recoil edge, it is possible to unfold the degeneracy. Figure 2.4 as an example shows the spectral edge of hydrogen recoils from 11 MeV neutrons in NE 213.

2.6.2 Fixed-angle scattering

Neutron scattering under a predefined angle breaks the degeneracy as well. The setup is accomplished (1) by adjusting the distance between neutron source and central detector in a way that the impact direction ("beamline") is well determined (reduction of the solid angle, cf. Section 6.3). (2) Then one or more neutron detectors are placed at a certain angle with respect to this neutron source beamline. Figure 2.5 shows the geometry of the setup. The outer neutron detectors are read out in coincidence with the central detector (Chapter 6 gives details). All our neutron detectors are specifically designed for neutron/gamma descrimination with fast response times in the order of several ns (Table 6.1), which is small compared to the neutron flight durations involved. Details are described in Section 6.2.

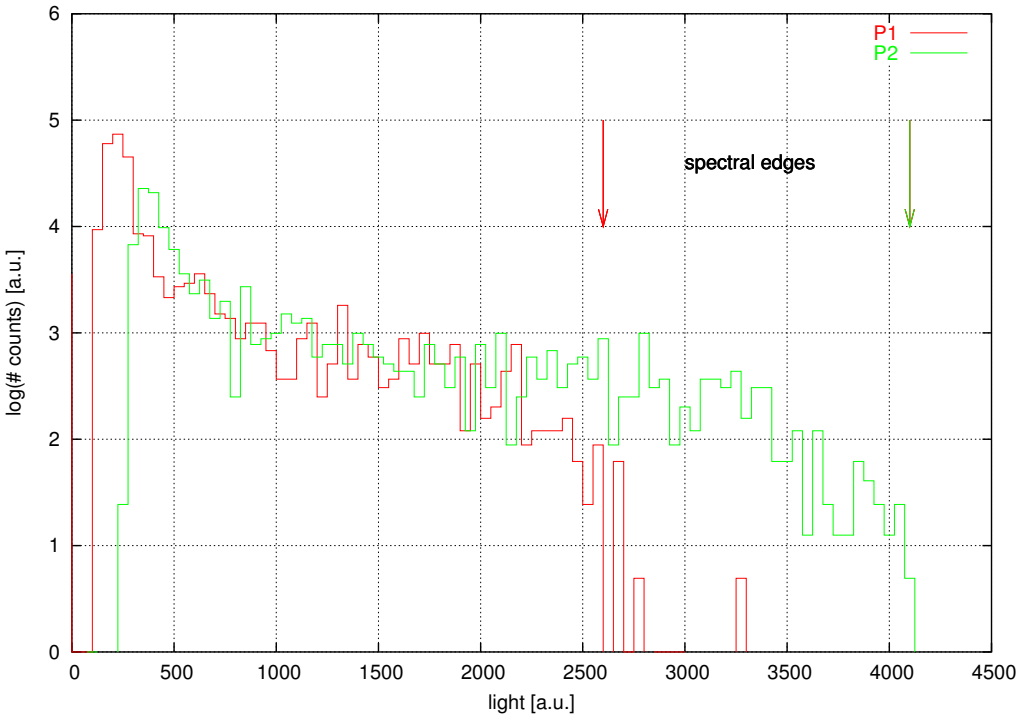

Figure 2.4: Proton recoil spectra of NE 213 induced by 11 MeV neutrons. Arrows mark the position of spectral edges. P1 and P2 are obtained with gate widths ("ports") that integrate the light output for n-/γ-discrimination (Subsection 6.2.2).

The result of this setup is a fixed dependency between impact energy and remaining energy of the scattered neutron for elastic recoils from a single element. Still, the recoil energy spectrum observed at a fixed angle is continuous as the input spectrum is continuous (cf. Section 7.1). If, for instance, only the scintillation signal in the central detector is measured and different target elements are involved, or if inelastic reactions are likely to take place, it is difficult or even impossible to extract information about different Quenching factors of different target elements from a continuous spectrum. Additional steps have to be taken to separate the light yield generated by the scattering from different target elements. Two further solutions are discussed in the following section: the fixing of the energy of neutrons that enter the central detector (monochromatic source) or the fixing of the point in time when these neutrons scatter (pulsed source).

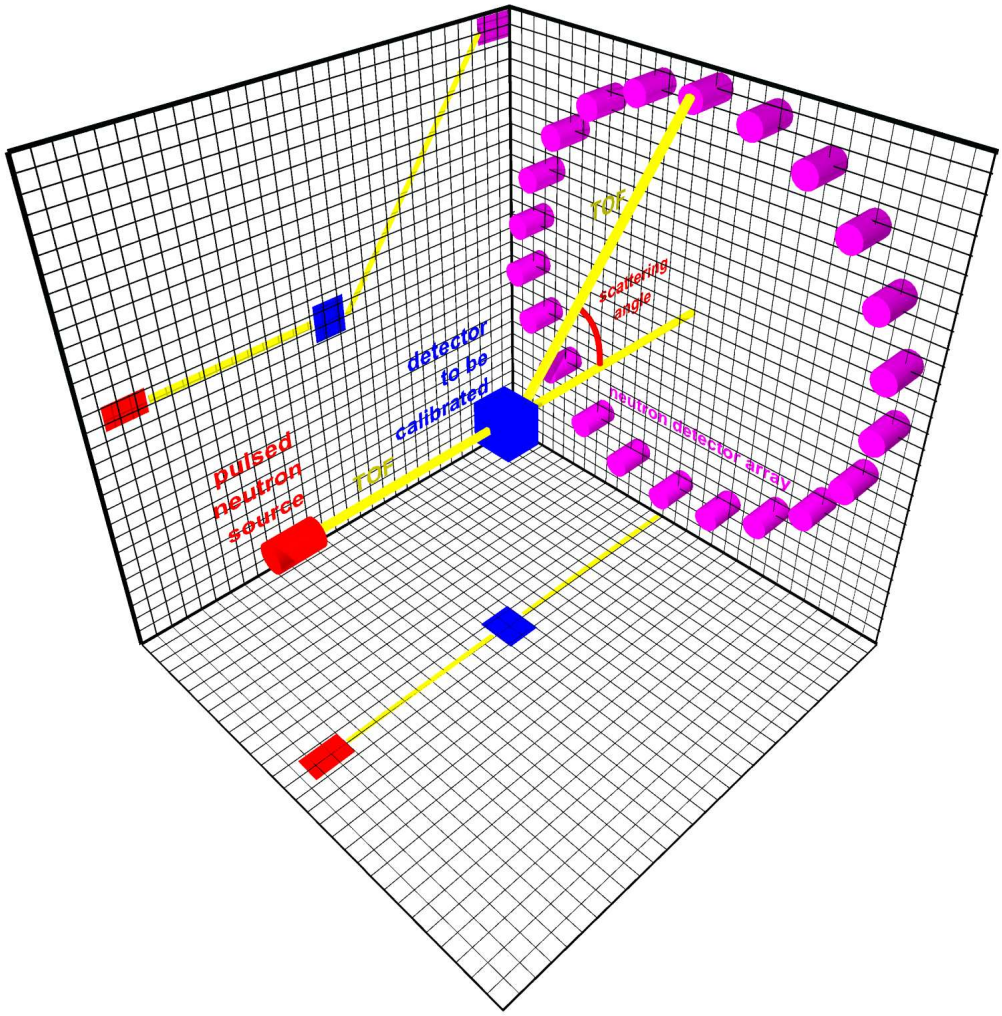

Figure 2.5: General scheme of the scattering setup: A pulsed neutron source irradiates the detector whose response is to be calibrated. Scattered neutrons are detected by the ring-shaped detector array, mounted under a common scattering angle with respect to the beam axis. ToF measurements between the source, the central and the neutron detectors provide information about incident and scattered neutrons.

2.7 Monochromaticity of Neutrons or Pulsed Neutrons?

The further procedure now depends on the signal timing resolution of the central detector in comparison with the neutron flight duration. In the case

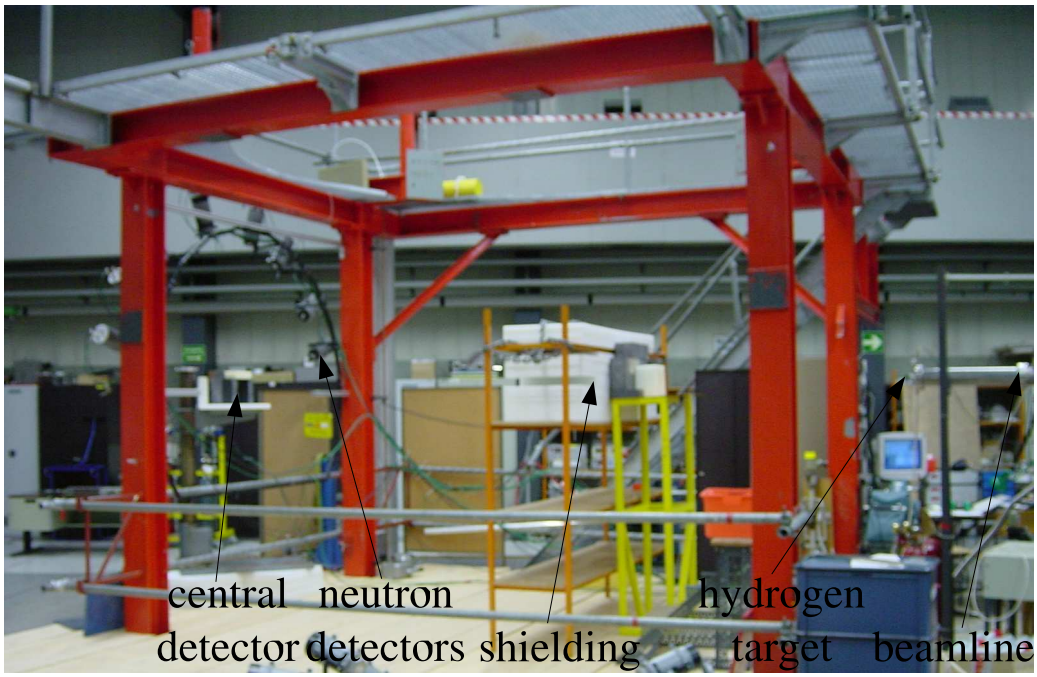

Figure 2.6: General scheme of the scattering setup: A pulsed neutron source irradiates the detector whose response is to be calibrated. Scattered neutrons are detected by the ring-shaped detector array, mounted under a common scattering angle with respect to the beam axis. ToF measurements between the source, the central and the neutron detectors provide information about incident and scattered neutrons.

of high resolution the energy of the scattered neutron can be determined by the time-of-flight ("ToF") between the central and the neutron detector. Then the sum of the energy deposition and the energy of the scattered neutron amounts to the total impact energy. Thus the complete energy balance is kinematically fixed. In this case the capability of neutron/gamma discrimination in the central detector would avoid further complications (of inelastic processes etc., see below). A room temperature measurement, where only the scintillation signal can be measured, is discussed in Section 7.1 for the case of a hydrogen-rich scintillator (NE213).

In the case when the timing resolution is poor, i.e. in the order of the neutron flight durations or worse (Figure 6.14), the only available information is the coincidence between central and neutron detector.

As long as the scintillation-light resolution is not as good as in Fig. 2.3, which is currently the case [42], this resolution restricts the determination of the Quenching Factor for different elements in one scintillator, and additional

steps must be taken to separate the response. From this point there are two ways out of this problem:

(1) Use of a mono-energetic neutron source (Subsection 6.1.1, no timing information)	(2) Use of a pulsed neutron beam (white spectrum)
Here the energy of the scattered neutron is not required to be measured (see below).	Here the timing information can be taken from the initial bunch.
The observation is performed for a fixed impact energy under a fixed scattering angle. The result is a correlation of the recoil energy with the measured scintillation signal in the central detector, allowing for a separate determination of QF for different target elements.	Separation of the QF of different elements is feasible as long as the energy of the scattered neutron correlates with the incident neutron energy, which is the case for elastic scattering.

Still, one of these solutions alone will not serve the purpose because of the following complications:

(a) Inelastic processes (n,n_1), (n,2n), etc. add to the spectra

(b) Beam-correlated accidental coincidences add to the spectra

Both contributions to those spectra that are expected for single elastic scattering of different target elements make the assignment of observed peaks in the scintillation signal to the individual kind of reaction (e.g. elastic scattering by O, Ca or W in $CaWO_4$) difficult, in particular since the different QF's for different elements are not yet known. These additional challenges are well addressed by a combination of the two separate solutions presented above: **a pulsed monoenergetic neutron beam** with independent measurement of the incident and the scattered neutron energies. This combination solves furthermore the complication arising if QF's of different elements have to be identified (if the QF's are different, the scintillation peak position from elastic scattering cannot be deduced from the calculated recoil energy ratios). The identification of the peak is now possible because the input energy is fixed and the energy of the scattered neutron is determined independently.

Figure 2.7 demonstrates the simulation of a measurement using a pulsed monoenergetic neutron source, at the same time fixing the scattering angle. Three event groups, attributed to elastic scattering on oxygen, calcium and tungsten, are well separated from each other. Also inelastic processes are included in the simulation.

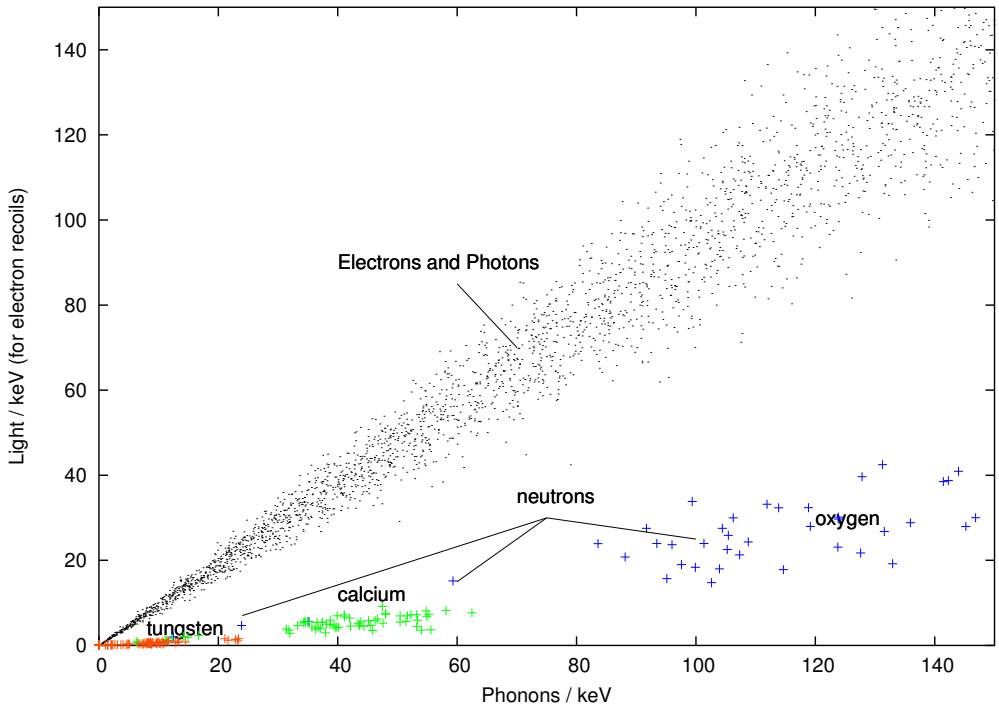

Figure 2.7: Simulated spectrum of a 40×40 mm^3 cylindrical $CaWO_4$–crystal irradiated by neutrons with energies 5 ± 0.5 MeV, scattered into $35 \pm 5°$. Compare this scatter plot with Figure 2.3 and Figure 2.1. The Quenching factors for calcium and tungsten were chosen to be 0.6 and 0.3, respectively, of the oxygen Quenching factor. The energy resolution of the light channel is assumed to be 15 %, the energy spread in the phonon channel is given by the energy spread of the neutron source and the detection uncertainty.

Still more complications will make data interpretation difficult: Beside nn-processes $\gamma\gamma$, γn and nγ will play a role.
These parasitic processes can be studied by:

- n/γ-discrimination by different pulseshapes in the neutron detectors
- n/γ-discrimination by Quenching in the central detector that is under investigation

- Different total time-of-flights (from the accelerator to the neutron detectors)

Chapter 3

Nuclear Interactions

The wealth of reactions that happen when fast neutrons strike a target composed of nuclei of different mass and charge calls for a detailed investigation of nuclear interactions that are important in the context of the calibration experiment. The following sections deal with the theoretical prediction of reaction cross sections. Model calculations that are available from different groups around the world working theoretically in this field, and Monte Carlo simulations performed in our institute using the Geant 4 code will be discussed. Various links to conditions of the local experimental setup and their influence on data acquisition and evaluation will be emphasized.

3.1 General considerations

The de-Broglie wave length λ of 11 MeV neutrons is 1.4 fm. Thus neutrons traversing a crystal will undergo refraction and diffraction at the atomic nuclei, the radii of which

$$R = r_0 A^{1/3} \tag{3.1}$$

($r_0 = 1.3 \pm 0.1$ fm) are only a small factor $l^{\max}$ greater than λ (l is the quantum number of the angular momentum). Table 3.1 gives a summary of basic nuclear properties of the isotopes in $CaWO_4$. Thus the corresponding impact parameters lead to angular momenta of only small integers l (in units of $\hbar$).

Potential ("shape elastic") scattering by tungsten nuclei for neutrons with energies of several MeV or more already exhibits giant resonances (Figure 3.1), where oxygen and calcium still show single narrow compound-nucleus (CN) resonances. At 11 MeV, however, the non-elastic total cross section

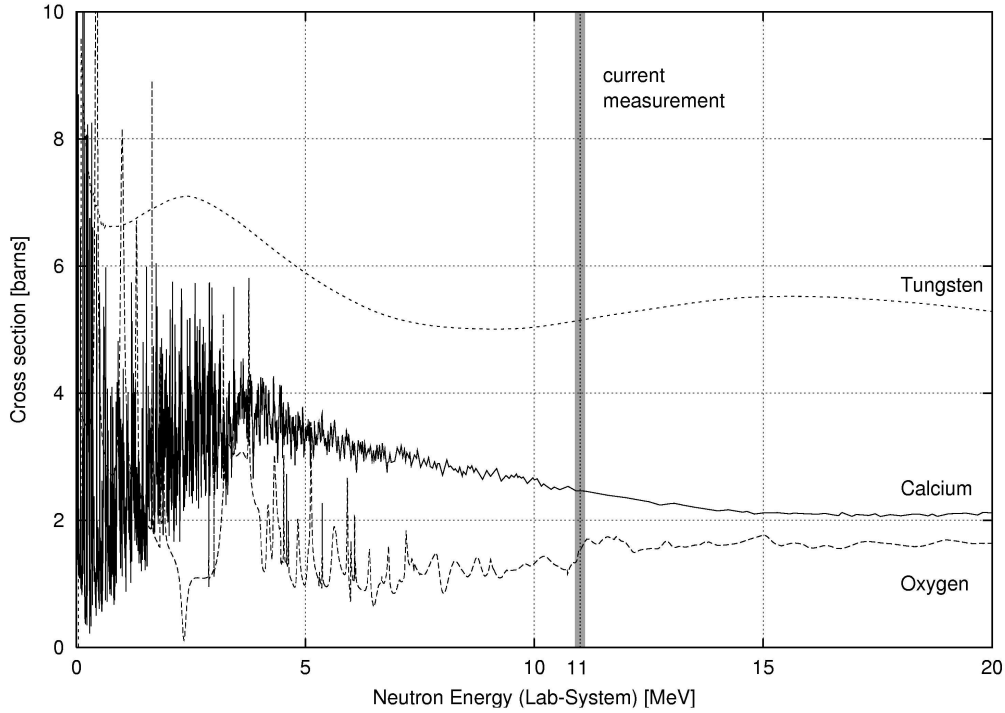

Figure 3.1: Total cross sections for neutrons scattered by the different elements in $CaWO_4$, derived from [23]. Different tungsten isotopes are weighted according to their natural abundance (Table 3.1). The shaded area comprises the region of current measurements (Table 3.2).

is dominated by intermediate resonances (so-called "pre-equilibrium emissions", see below) for all three elements.

The neutron energy of 11 MeV is by far high enough to activate nuclear excitations for all elements. Since ${}^{16}_{8}O_8$ and ${}^{40}_{20}Ca_{20}$ are both doubly magic nuclei, the energy of each first excitation level is separated by more than 3 MeV from the ground state (Table 3.1) and is thus well distinguishable by the measurement of the scattered neutron time-of-flight (*ToF*) in our setup. In the case of tungsten, where the naturally most abundant isotopes are even/even-nuclei, the number of paired nucleons bound above the last closed shell is high. Therefore these nuclei are deformed and give rise to low-lying rotational levels with an energy spacing in the order of 100 keV. These small energy losses for the scattered neutrons cannot be resolved by our ToF setup, so we will restrict the further discussion of reactions competing with elastic scattering to tungsten excitations from inelastic scattering.

	O-16	Ca-40	W-182	W-183	W-184	W-186
abundance [%]	100	97	26	14	31	29
nuclear radius R [fm]	3.3	4.4	7.4	7.4	7.4	7.4
S_n [keV]	15664	15641	8064	6191	7412	7194
S_p [keV]	12127	8328	7094	7222	7700	8404
1st excited level [keV]	6049	3353	100	46	111	123
$\sigma_{el,tot}$ [barns]	0.87	1.20	2.57	2.55	2.63	2.62

Table 3.1: Some important general properties of the isotopes in $CaWO_4$ crystals: Atomic number, relative natural abundance, nuclear radius R, neutron separation energy S_n, proton separation energy S_p, energy of the first excited state [17], total elastic cross section $\sigma_{el,tot}$ for 11 MeV neutrons [23]. The neutron separation energy is $S_n := M_N - M_{N-1} - M_n$, accordingly S_p.

3.2 Tungsten

Above 1 MeV, the total cross section for neutrons scattering from tungsten equals to a very good approximation twice the elastic cross section (Figure 3.2) indicating a "black" nucleus [29], i.e. every neutron that enters the nucleus within $\lambda \cdot l^{max}$ is expunged from the elastic channel and absorbed into one of the non-elastic channels summarized in Table 3.2.

As long as the incident neutron energy is lower than the neutron separation energy S_n, which amounts to 6-8 MeV for different tungsten isotopes (Table 3.1), only inelastic neutron scattering with radiative compound deexcitation will occur (Figure 3.3). But as soon as the threshold for particle emission is exceeded, such processes of strong interaction ([35] p. 36) will preferentially take place as compared to radiative deexcitation. For small excitation energies (high secondary neutron energies), direct processes and emissions during the pre-equilibrium compound formation phase are superimposed on the Maxwellian distribution of a thermal neutron evaporation spectrum stemming from the compound nucleus. Generally, the emission of one or more neutrons at higher energies is the leading deexcitation process below 20 MeV since protons cannot overcome (or even tunnel through) the additional Coulomb barrier of about 13 MeV to a significant extent (Table 3.1). The same holds for α-particle emission.

Experimentally all non-elastic reactions without neutron emission (e.g.

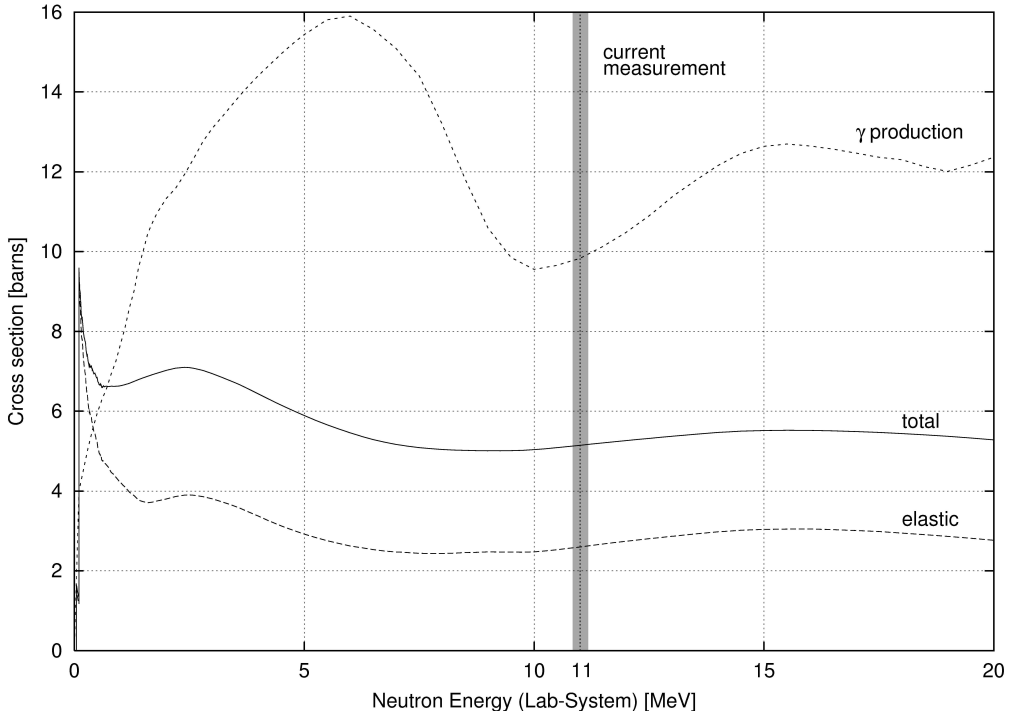

Figure 3.2: Principal cross sections for neutrons striking tungsten nuclei, derived from [23]: total and elastic cross section and the cross section for overall gamma production. The mean number of gammas produced per hit is greater than 1 leading to a cross section that even exceeds the total one. Major contributions to the photon production in descending order of occurrence are (n,2n), inelastic scattering and n-capture. Different tungsten isotopes are weighted according to their natural abundances (Table 3.1). The shaded area comprises the region of current measurements (see also Table 3.2).

(n,γ), (n,α), (n,p) etc.) either do not trigger the data acquisition and therefore do not contribute to the measured spectra since the trigger setup waits for particles escaping the crystal, or, in the case of one or more gammas escaping the crystal, are rejected by pulse shape discrimination. For secondary neutron emission (n,2n) both neutrons are slow enough due to the loss of neutron binding energy ($\sim$ 7 MeV) that they can easily be separated from elastically scattered neutrons via time-of-flight measurements. Summarizing, all non-elastic reactions from all elements can be well discriminated against elastic recoils by the experimental setup except for inelastic reactions that happen to tungsten. The further discussion will accordingly focus on inelastic contributions to tungsten recoils.

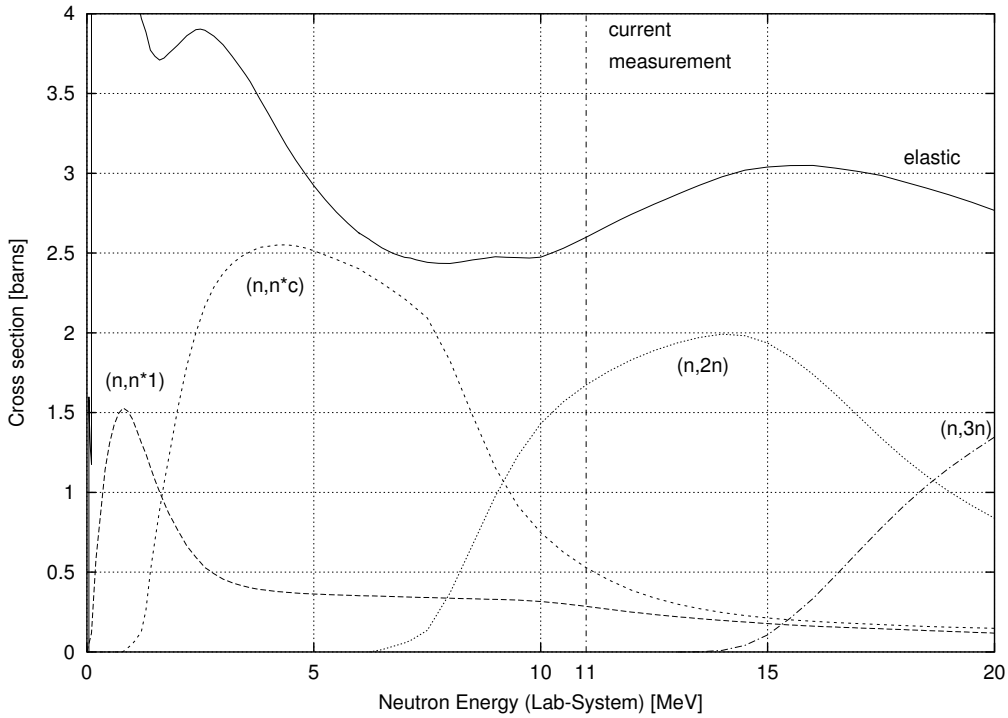

Figure 3.3: Elastic and main non-elastic cross sections for neutrons striking tungsten nuclei, derived from [23]. Different tungsten isotopes are weighted according to their natural abundances (Table 3.1). (n,n*1) ist the excitation of the individual first excited state, (n,n*c) is the corresponding excitation to levels above the individual first excited state (Table 3.2). The line at 11 MeV marks the region of current measurements .

3.3 Inelastic scattering

The following considerations are complicated by the fact that, of course, every tungsten isotope has its own excitation levels. Fig. 3.4 shows the excitation levels of $^{182}_{74}$W as an example. For a typical scattering setup with a ToF acceptance window open for 10 ns all neutrons that excite levels up to 4 MeV contribute to the measured spectrum. Electromagnetic transitions show individual levels with a mean spacing of 15 keV above 1 MeV, so one of more than 200 levels for each tungsten isotope may be involved after application of all experimentally feasible cuts. Each of these levels has got a different excitation probability and one or more de-excitation channels with different transition probabilities towards different lower-lying levels. Additionally each of those gammas that are emitted by the excited nucleus may deposit all, part or none of its energy inside the crystal. It is not only for this

σ [barn]	tot	el	non	in	(n,n1)	(n,n_c)	(n,2n)	(n,p)	(n,α)
O-16	1.52	0.87	0.65	0.35	0.03	–	–	0.01	0.29
Ca-nat	2.47	1.20	1.27	0.45	< 0.01	0.23	< 0.01	0.45	0.22
W-184	5.15	2.63	2.52	0.81	0.31	0.47	1.71	< 0.01	–

Table 3.2: Comparison between cross sections given in barns of dominant reactions of 11 MeV neutrons scattered by the isotopes in $CaWO_4$ [23]. Ca-nat is the weighted mean according to the natural abundance (Table 3.1). W-184 was chosen as representative for the different tungsten isotopes. σ_{tot} is the total cross section, σ_{el} is the total elastic cross section. σ_{non} is the sum over all non-elastic reactions, σ_{in} equals to the sum of the inelastic level excitation and continuum cross sections $\sigma_{(\mathrm{n,n_c})}$. A "–" marks cross sections that were not calculated.

complexity why Monte-Carlo simulations (Section 3.6) can be very helpfull in the interpretation of the data.

The cross section for inelastic neutron scattering can be divided into compound, direct and pre-equilibrium emission [38].

Compound rate: According to the Fermi gas model, the temperature T of a tungsten nucleus excited by 11 MeV corresponds to $T = 0.5$ MeV (this is where the Maxwellian distribution peaks). Hence compound emission cross sections for neutrons in the energy range mentioned above (7–11 MeV within the ToF-cut) are lower by 7–8 orders of magnitude compared to the elastic scattering and therefore are completely negligible (see Figure 3.5). Mathematically, this is a result from the exponential decrease of the Maxwellian distribution above 0.5 MeV. Physically, it simply follows from the restricted phase space state density of the residual nucleus. Due to the independence of the neutron emission from the compound formation the angular neutron distribution is isotropic (or at least symmetric around 90° when angular momenta of the CN and the remaining nucleus couple [25]). The continuum inelastic cross section originates almost entirely from compound decay.

Direct rate: Imagine a neutron entering the nucleus and striking a first single nucleon. If the energy of this neutron is still high enough to re-escape the nuclear potential and the nucleus is sufficiently transparent which is essentially the case for higher values of l, the neutron may

leave the nucleus without further interaction. This is the case for incident neutron energies $\gtrsim$ 10 MeV (where the energy of the incident neutron exceeds the binding energy) and leads to excitation of low-lying states of the final nucleus. The angular neutron distribution is highly anisotropic.

Pre-equilibrium emission: Between the two extreme cases of compound nucleus formation and the direct-interaction mechanism there are reactions intermediate with regard to complexity and progression in time where a nucleon is emitted after some collisions, but before thermalization. An excitonic model is used for cross section calculations where from every intermediate state, characterized by the number and excitation energy of excited nucleons and holes, particle emission takes place with a probability proportional to the partial density of states [29].

3.4 Elastic scattering

The cross sections for elastic scattering of neutrons (e.g. Figure 3.6 for ^{184}W, Figure 3.7 and Table 3.3 for all elements in $CaWO_4$) are taken from Evaluated Neutron Data Files (*ENDF*, Section 3.5). A neutron is scattered elastically either via CN formation or by diffraction from the nuclear potential (formelastic scattering), the latter giving rise to the pronounced Fraunhofer pattern displayed in Figure 3.7.

$d\sigma/d\Omega$	80°	100°	108°	120°	140°
O-16	$7.05 \cdot 10^{-1}$	1.21	1.36	1.19	$6.36 \cdot 10^{-1}$
Ca-40	$5.41 \cdot 10^{-2}$	$1.74 \cdot 10^{-1}$	$1.91 \cdot 10^{-1}$	$1.33 \cdot 10^{-1}$	$5.51 \cdot 10^{-2}$
W-nat	$4.14 \cdot 10^{-1}$	$5.39 \cdot 10^{-2}$	$5.79 \cdot 10^{-2}$	$1.08 \cdot 10^{-1}$	$2.58 \cdot 10^{-2}$

Table 3.3: Differential elastic cross sections (Lab-System) in barns/sr for 11 MeV neutrons scattered by the different isotopes in $CaWO_4$ (see also Figure 3.7), derived from [23], for the specific observation angles realized in various measurement campaigns (Lab-System). The oxygen cross section is already multiplied by 4 according to the stoichiometric condition. Different tungsten isotopes are weighted according to their natural abundances (Table 3.1).

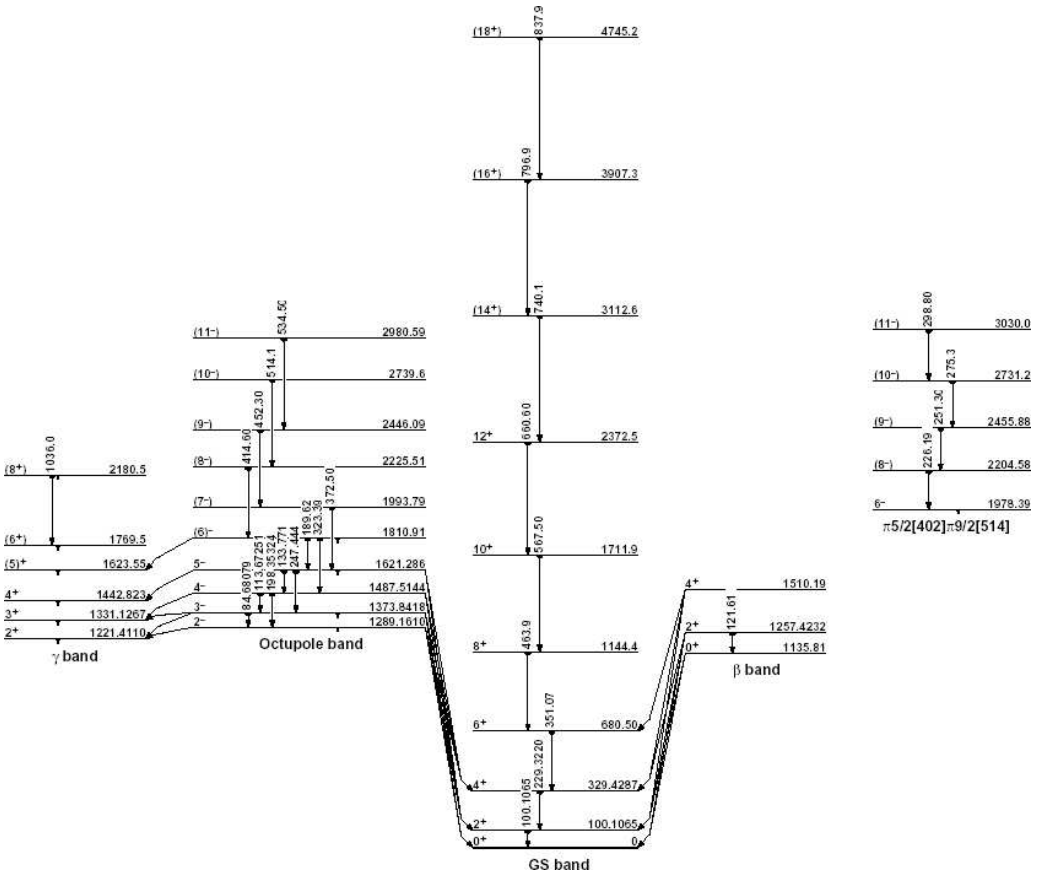

Figure 3.4: Part of the lowest lying excitation levels of $^{182}_{74}$W [17]: The rotational ground state band (GS band), quadrupole β and γ vibration (β band and γ band, resp.), octupole vibration band (Octupole band) and an example for a band based on the configuration derived from the proton shell model configuration ($\pi 5/2[402]\pi 9/2[514]$).

3.5 Evaluated Neutron Data Files (ENDF)

Generally, nuclear cross section investigations are carried out by an adaption of model parameters to experimental data as far as they are available in the literature. All models solve a time-independent Schrödinger equation with appropriate assumptions on interactions and waveforms. Since the problem of a self-consistent derivation of the nuclear potential from nucleon-nucleon interaction has not been solved up to now [25], semi-empirical potential shapes are tested to match the experimental data (optical model). For a given model potential with a set of parameters like potential depth, range etc., solutions of Schrödinger's differential equation are derived. These solutions are in many

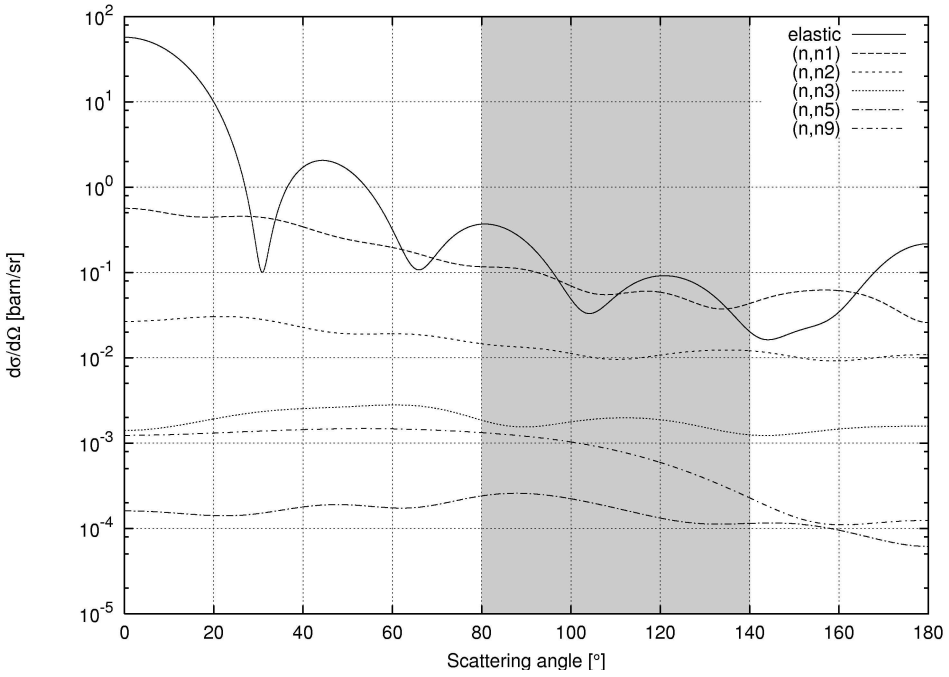

Figure 3.5: Differential elastic and principal inelastic cross sections (Lab-System) for 11 MeV neutrons scattered by W-182 as representative, derived from [23] ENDF. (n,n1) denotes the cross section for leaving the target nucleus in its first excited state, etc. The shaded area comprises the region of current measurements (Table 3.3).

cases calculated by means of partial wave decomposition.

All cross section plots in the previous sections were derived from Evaluated Neutron Data Files of reference [23]. There are different institutions around the world (e.g. the T-2 group of Los Alamos National Laboratories [23, a)] or the Japanese JAERI, also Russian and European evaluations) who use different numerical codes for self-consistent modelling of nuclear interactions. Each reference uses different codes for different reaction types and energy ranges, e.g. [23, a)] calls the GNASH code for Hauser-Feshbach calculations. Depending on the quality of the code, the consideration of different reaction mechanisms and availability of measurements used to match model parameters (e.g. of the optical model), cross section predictions of different sites vary substantially. This is especially remarkable for low-level excitations where [23, a)] (i) does not account at all for direct reactions and (ii) only accounts for the first two excited levels while [23, b)] takes about 10

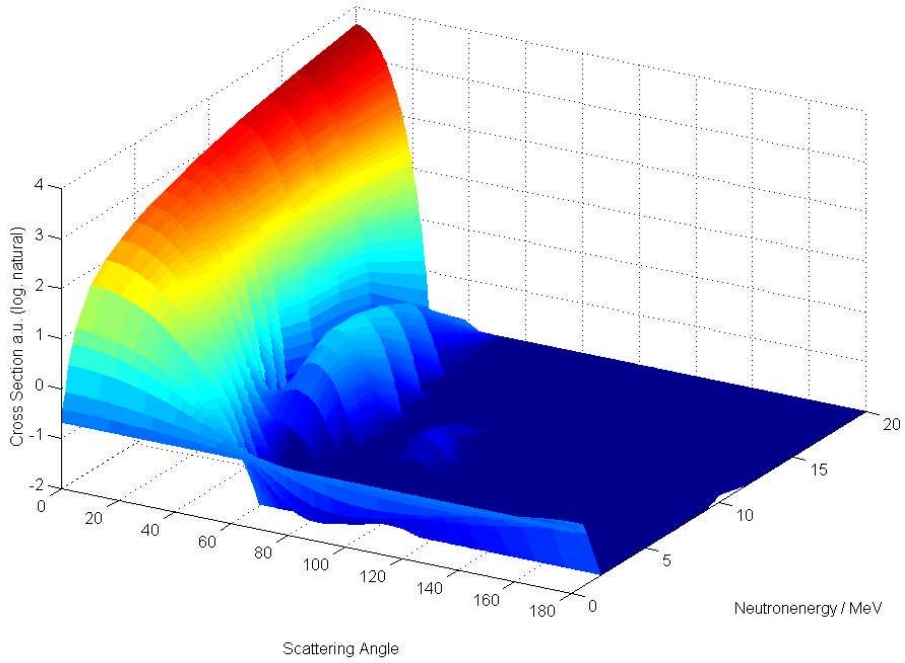

Figure 3.6: Elastic differential angular cross section for neutrons scattered by W-184 (CMS) [23] as representative for the tungsten isotopes.

particulary lumped levels on the average into consideration. The rest of the inelastic scattering cross sections usually are assumed to overlap and added to the respective continuum cross section. The user still needs to expand function parameters (e.g. Legendre parameters), interpolate between them in an appropriate manner and, if necessary, transform between laboratory and CM-system. (Input energies are always given in the lab system. Elastic angular cross sections are given in the CM system, all other reaction angular distributions mostly are given in the Lab system). For the cross section plots of the previous section each the appropriate source was chosen as indicated.

3.6 Geant

The complexity of processes that start from neutron interaction and finish with a measurable signal in one or more detectors of the calibration setup makes Monte-Carlo simulations desirable as was already outlined in Section 3.3. The incident particles (neutrons as well as gammas from the production reaction) have to be taken from realistic energy spectra and followed as they

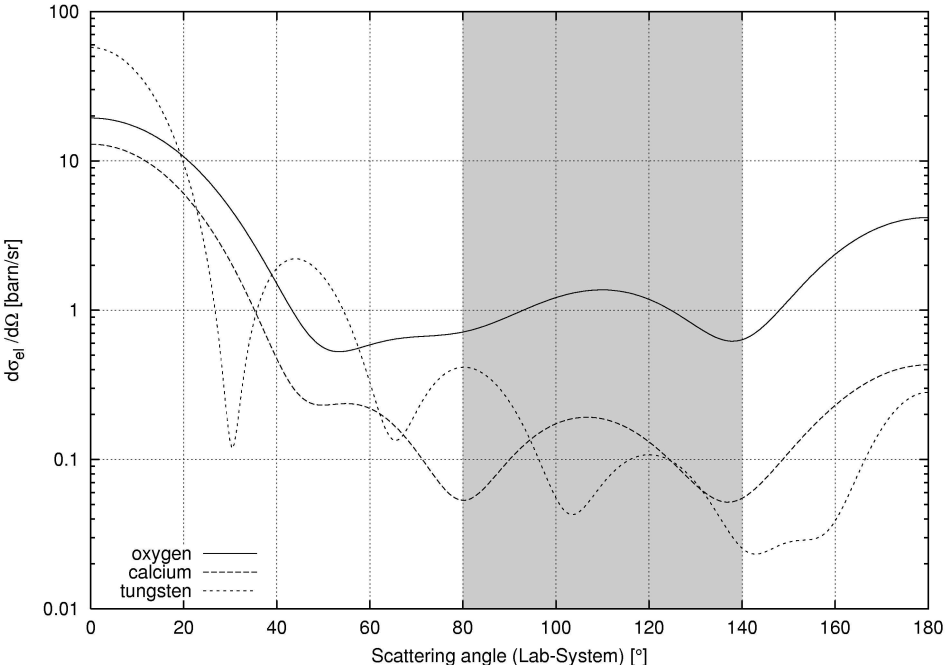

Figure 3.7: Differential elastic cross sections for 11 MeV neutrons scattered by the different isotopes in $CaWO_4$, derived from [23]. The oxygen cross section is already multiplied by 4 according to the stoichiometric condition. Different tungsten isotopes are weighted according to their natural abundance (Table 3.1). The shaded area comprises the region of current measurements (Table 3.3).

undergo nuclear and/or atomic interactions, multiple scattering in detectors and/or in the experimental environment leading possibly to random coincidences, finally leaving gamma cascades at the sites of interaction, etc. All of these processes depend on energy and many of them on the scattering angle. A diploma thesis [48] in our institute performed first simulations using the program Geant 4 for the relevant setup. Despite the variety of interactions almost every reaction type is qualitatively accounted for, some of them (esp. elastic scattering) even quantitatively. Nevertheless, one remarkable result of the investigation [48] is:

- In individual simulation steps energy and momentum are not conserved. For instance, in inelastic reactions this yields a systematic gain of nuclear recoil energy.

Moreover, for a reliable evaluation there are many more too severe flaws that cannot be corrected easily, some of which are summarized here:

- All inelastic reactions are treated as completely isotropic, even the highly anisotropic low-level excitations (see Figure 3.5).
- Forbidden level transitions take place with too high intensity, sometimes leading to a division in gamma energies that would not be observed in practice.
- Cross sections of different isotopes and reactions sometimes do not agree with any of reference [23], e.g. the total cross sections of levels 3 and 4 of ^{183}W are highly overestimated.
- Most of the gamma interactions with the atomic electron shells (including Coulomb scattering, X-ray production, etc.) were not considered in [48], probably because they were not "switched on".

Unfortunately, these misfeatures are most aggravating in such cases where an analytical evaluation is likewise hard to achieve. Concluding, quantitative results from a Geant 4 simulation are not available up to now.

Chapter 4

Matter interactions

This chapter deals with the fate and the effects that a recoiling nucleus (previous Chapter 3) experiences within the target material during its stopping process. The implications leading to the signals observed in the attached detectors (Section 1.5) are discussed with strong emphasis put on the scintillation outcome in Chapter 5. The propagation of phonons is comprehensively discussed in the parallel work of [42]. Throughout this chapter the recoiling nucleus struck by the neutron is referred to as "ion" (whether it is charged or neutral) while the absorber target atoms are simply called "atoms".

4.1 The stopping of ions in solids

Niels Bohr was the first to suggest the total stopping cross-section of ions in solids being divided into two parts: the energy transferred by the ion to the target electrons (called electronic stopping or inelastic energy loss) and to the target nuclei (called nuclear stopping or elastic energy loss) [53]. Particles lose energy in discrete amounts in nuclear collisions since a maximum impact parameter is given by intra-atomic screening. The energy loss from electronic interactions has a more continuous character since the charged ion interacts simultaneously with many electrons over various distances, while these electrons may only be described quantum-mechanically by probability densities. Although this separation of the energy loss of the ion into two separate components ignores a possible correlation between nuclear collisions and large inelastic losses due to electronic excitation, it is felt that this correlation probably is not significant when averaging over many collisions, as when an ion penetrates a solid. However it is of importance for single-scattering studies and for very thin targets. Additional interaction processes like nuclear interactions, elastic electronic collisions, etc. are neglected as they play only

a minor role compared to the two processes just mentioned.

The relative weight of the nuclear and electronic stopping processes strongly depends on the velocity v_1 and charge Z_1^* of the ion [29]. Here Z_1^* is the (velocity-dependent) degree of ionization of the moving atom, taking target polarization and Coulomb screening for close collisions into account.

It is convenient to define the nuclear stopping cross section $S_{\mathrm{n}}(E)$ that is related to the energy lost by the ion per unit path length $\mathrm{d}E/\mathrm{d}x$ by the relation

$$\frac{\mathrm{d}E}{\mathrm{d}x} = n\, S_{\mathrm{n}}(E) \tag{4.1}$$

where n is the atomic number density of the target.

4.1.1 Electronic Stopping

Around 1935, Bethe and Bloch stated the many problems in understanding stopping powers from the perspective of quantum mechanics, and derived in the Born approximation the fundamental equations for the stopping of very fast particles in a quantized electron plasma [53]. This theoretical approach remains the basic method for evaluating the energy loss of light particles with velocities of 10 MeV/u - 2 GeV/u (u = atomic mass unit). This restriction in velocity is because below these velocities the ion projectile may not be fully stripped of its electrons (which is assumed by this theory), and above this velocity there are additional relativistic corrections. Ions that got their kinetic energy from recoils induced by dark matter WIMPs or by neutrons in our scattering experiment are supposed to be much slower (Table 4.1). Thus the first problem to be solved in calculating the electronic stopping of such an ion is to estimate its degree of ionization, which is called the "effective-charge" problem. We define ζ as the fractional effective charge of an ion:

$$Z_1^*(v, Z_2) = Z_1\, \zeta(v, Z_2) \tag{4.2}$$

where Z_1^* is the effective charge of an ion of atomic number Z_1, at velocity v, and in a target Z_2. Bohr had suggested that the ion's electrons which have orbital velocities less than the momentary velocity v_1 of the ion would be stripped off, leaving the ion only with its inner high-velocity electrons. The idea behind this assumption is that for whatever target electrons moving faster than the ion, collisions with the ion are mostly adiabatic without direct energy loss. Following Brandt and Kitagawa [53], the ion's electron velocities are not just compared to the ion velocity, but to the relative velocity v_r

v_1/v_0	100°	108°	120°	140°
O-16	1.95	2.05	2.18	2.35
Ca-40	0.80	0.84	0.90	0.97
W-nat	0.18	0.19	0.20	0.21

Table 4.1: Initial velocities v_1 in units of the Bohr velocity $v_0 = 2.2$ mm/ns $\widehat{=}$ 25 keV/u of the atoms struck by 11 MeV neutrons in $CaWO_4$ for the specific observation angles realized in various beamtimes (Table 3.3). Different tungsten isotopes are weighted according to their natural abundance.

between the ion and the electronic velocity $\boldsymbol{v_e}$ of the medium averaged over all directions of electron motion:

$$v_r \; := \langle |\boldsymbol{v_1} - \boldsymbol{v_e}| \rangle \tag{4.3}$$

If the initial velocity of the ion $v_1 > v_e$, then in Eq. (4.3) v_r is minimum for greatest v_e and target electrons at the Fermi edge will preferentially be captured by the ion. While the concept of a Fermi velocity was introduced for a quantized free electron gas as the electron velocity of the highest occupied level, its term involving significant simplifications for real solids, many types of phenomena can be evaluated using a similar expression. In the case of materials with a band gap (Section 5.5) where fewer low-energy excitation levels are available, the Fermi velocity can be measured by electron energy loss experiments which can also be used to deduce the density of valence electrons.

The following section is subdivided according to different physical conditions which depend on the ion's velocity:
(a) stopping of very low velocity ions ($v_1 < v_F$, i.e. $E_{kin,1} < 25$ keV/u)
(b) stopping of high velocity ions ($v_1 > 3v_F$, i.e. $E_{kin,1} > 200$ keV/u).

Low-velocity heavy ions

Besides very elaborative considerations that include numerical evaluations using the local density approximation in stopping power theory (e.g. by Lindhard [53]), roughly speaking, a typical energy loss per unit distance for slow particles is proportional to the ion velocity, the square of the effective charge of the ion and the cube root of the electronic density ρ_e of the medium:

$$\frac{\mathrm{d}E}{\mathrm{d}x} \propto v_1 \, Z_1^{*2} \rho_\mathrm{e}^{1/3} \tag{4.4}$$

For bandgap materials the velocity dependence is slightly different and usually accounted for by $\mathrm{d}E/\mathrm{d}x \propto v_1^{0.7}$.

In the $CaWO_4$ scattering experiment we are concerned with ion velocities v_1 in the range of or less than the Fermi velocity v_F of the crystal they are traversing (Table 4.1), since the Fermi velocity of solids usually falls between 0.7 and 1.3 v_0 (v_0 is the Bohr velocity). This means that the charge state of the struck ions is close to neutral. In addition, the rule holds that the lower their momentary velocity the longer the time span where nuclear stopping is the main effective deceleration mechanism, since for an ion with $\zeta = 0$ no electronic stopping is calculated (see the introduction of Section 4.1).

High-velocity heavy ions

An important empirical rule for the calculation of the stopping cross section S_{HI} of fast heavy ions in solids is to relate this stopping power to the equivalent proton stopping powers S_{H}. This is called the heavy-ion scaling rule and has the form:

$$S_{\mathrm{HI}} = S_{\mathrm{H}}(Z^*_{\mathrm{HI}})^2 = S_{\mathrm{H}} Z^2_{\mathrm{HI}} \zeta^2 \tag{4.5}$$

where Z_{HI} is the atomic number of the heavy ion and ζ is its fractional effective charge. This effective charge term can be estimated from the Thomas-Fermi atomic theory, which may be applicable in the region where Thomas-Fermi atoms approximate Hartree-Fock atoms, i.e. where $0.3 \leq \zeta \leq 0.8$.

4.1.2 Nuclear Stopping

The ion's energy loss in elastic collisions with the target atoms simply follows the kinematic relationships discussed in Appendix A. The nuclear stopping cross section $S_{\mathrm{n}}(E)$ is defined according to Equation (5.3). Thus the nuclear stopping power, $S_{\mathrm{n}}(E)$, is the average energy transferred when summed over all impact parameters p. Together with the maximum energy transfer Γ, see Eq. (A.34), we have:

$$S_{\mathrm{n}}(E) = 2\pi\Gamma E \int_0^{p_{\max}} \sin^2 \frac{\Theta}{2}\, p\, \mathrm{d}p \tag{4.6}$$

with the integration's upper limit $p_{\max}$ being the sum of the two atomic radii, beyond which the interatomic potential, and the recoil energy E_R, is zero. In a universal screening function which can be used for all possible values of Z_1 and Z_2, the best fit for a reduced radial coordinate is given by [53]

$$a_U = 0.89\, a_0/(Z_1^{0.23} + Z_2^{0.23}) \tag{4.7}$$

where Z_1 and Z_2 are the atomic numbers of the ion and target atom, a_0 is the Bohr radius (0.52 Å). The exponent 0.23 accounts best for charge screening at closest p. For a universal nuclear stopping calculation [53] it is useful to turn to a (dimensionless) reduced energy ϵ defined as

$$\epsilon := \frac{a_U M_2}{Z_1 Z_2 e^2 (M_1 + M_2)} E \tag{4.8}$$

Examples of the reduced energy for recoiling ions in $CaWO_4$ in our scattering experiment are given in Table 4.2. The reduced nuclear stopping can be calculated as:

$$S_{\mathrm{n}}(E) = \frac{\pi a_U^2 \Gamma E}{\epsilon} S_{\mathrm{n}}(\epsilon) \tag{4.9}$$

(its unit is energy/(atoms/area)). For practical calcuations and $\epsilon < 30$, the universal nuclear stopping can be written as

$$S_{\mathrm{n}}(\epsilon) = \frac{\ln(1 + 1.14\epsilon)}{2[\epsilon + 0.01\epsilon^{0.21} + 0.2\epsilon^{0.5}]} \tag{4.10}$$

ion / target	O-16	Ca-40	W-nat
O-16	174	89	26
Ca-40	16	9.6	3.6
W-nat	0.22	0.17	0.12

Table 4.2: Examples of reduced energy calculated according to Equation (4.8) for oxygen (2209 keV), calcium (943 keV) and tungsten (212 keV) ions striking target atoms mentioned in either column. The energy values are calculated for 11 MeV neutrons scattered into 140°. (cf. Table 7.2)

4.2 Cascades

In this section we shall consider the fate of a target atom knocked off by a nuclear collision as described in Section 4.1.2. In order to understand which

	O-16	Ca-nat	W-nat
Lattice Binding Energy	3	3	3
Surface Binding Energy	2.00	1.83	8.68
Displacement Energy	28	25	25

Table 4.3: Lattice energies of $CaWO_4$ in eV [46].

processes will happen, it is necessary to compare the recoil energy of the target atoms with the relevant lattice energies (Table 4.3).

Lattice Binding Energy The lattice binding energy E_{latt} is defined as the minimum energy needed to remove an atom from a lattice site. It takes energy to break electronic bonds and displace an atom from a lattice site. The lattice binding energy must be smaller than the displacement energy since more energy is required to prevent the atom from oscillating back to its original lattice site.

Surface Binding Energy The surface binding energy of a target atom is less than in the case when the atom is inside the solid and surrounded by other atoms since an atom at the target surface is not confined on one side. Thus a surface atom has fewer bonds which must be broken.

Displacement Energy A displacement is the process where an energetic incident atom knocks a lattice atom off its site. The energy E_{disp} required to knock a target atom far enough away from its lattice site so that it will not immediately return is called displacement energy. This minimum energy produces a "Frenkel Pair", i,e. a single vacancy and a nearby interstitial atom, which is a fundamental type of target damage caused by the ion. Interstitial atoms are atoms knocked out of their original site, and come to stop not on a regular lattice site of the solid. Also the incident ions, when they stop, are considered interstitial atoms.

Assume that an incident atom has atomic number Z_1 and energy E and that it has a collision within the target with an atom of atomic number Z_2. After the collision, the incident ion has energy E_1 and the struck atom has energy E_2.

- If the moving atom hits a target atom and transfers more energy than E_{disp}, $\boldsymbol{E_2 > E_{\text{disp}}}$, the target atom will be ejected from its lattice site. These events will be called *displacements*.

  - A *vacancy* (lattice site without an atom) occurs if both $\boldsymbol{E_1 > E_{\text{disp}}}$ and $E_2 > E_{\text{disp}}$, i.e. both atoms have enough energy to leave the site and become moving atoms. Atom Z_2 will lose energy to the lattice, so the recoiling energy E_2 will be reduced by E_{disp} before its next collision takes place.
  - If $\boldsymbol{E_1 < E_{\text{disp}}}$ and $\boldsymbol{Z_1 = Z_2}$, then the incoming atom will remain at the site and the collision is called a *replacement collision* with E_1 released as phonons. The atom at the lattice site remains the same atom by exchange. If $\boldsymbol{Z_1 \neq Z_2}$ then Z_1 becomes a stopped *interstitial atom* (comes to a stop out of its original site).

- If $\boldsymbol{E_2 < E_{\text{disp}}}$, then the struck atom does not have enough energy to leave its site and will vibrate back at its original site releasing E_2 as phonons.

  - Finally, if $\boldsymbol{E_1 < E_{\text{disp}}}$, then Z_1 becomes an interstitial and $E_1 + E_2$ is released as phonons.

For primary recoil energies below several MeV, these collisions happen many times not only to the ion but also for many kicked-off atoms that generate recoil atoms as well. In this way, a cascade of recoiling ions is generated. For $CaWO_4$ in our scattering experiment, a typical recoil cascade consists of many hundred participating atoms independent on the primary ion.

Usually at room temperature, most of the damage disappears because thermal energies are large enough for the lattice atoms to allow simple damage to grow back into crystalline form ("self-anneal").

4.3 SRIM and ranges

SRIM, a Monte Carlo computer program [46] which calculates the slowing down and scattering of energetic ions in amorphous targets is available online. Since the target is considered amorphous, atoms are located at random positions, thus the directional properties of the crystal lattice are ignored (see TRIM.X for a treatment of crystalline targets [53]). But as the multiplicity of nuclear recoil cascades is quite high, directional effects may soon be smeared out due to averaging over many flight directions, at least for different cascade

ions. To estimate the importance of this effect is not trivial since in a scattering experiment like the one presented here the primary direction of the entering neutron is fixed with regard to the crystal orientation and deflection angles of the primary ion are peaked in forward direction according to the respective cross sections (Chapter 3). The treatment of multi-atomic materials is simply respected by assuming the probabilities of encounters being proportional to the stoichiometric abundance of the atoms.

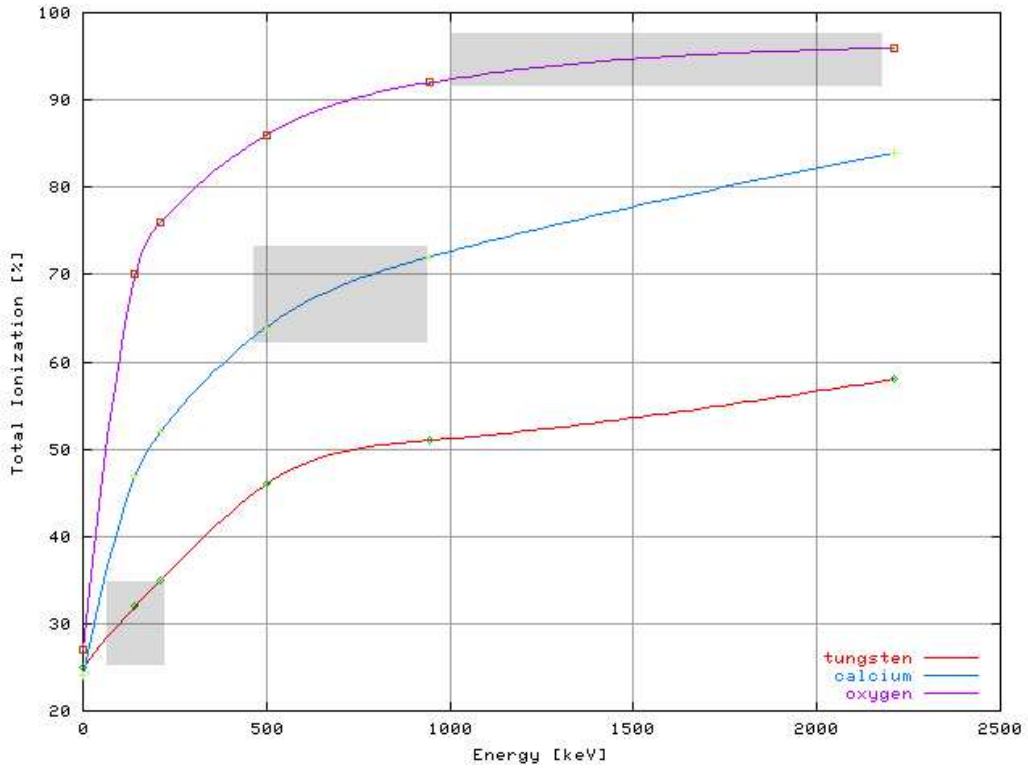

Figure 4.1: Simulated total ionization of calcium-, oxygen- and tungsten-ions in $CaWO_4$. The shaded areas comprise recoil energies realized in various beamtimes. The total ionization is the sum of the ionization induced by the ion and the ionization induced by atoms of the cascade.

Figure 4.1 shows the calculated ionization fraction of the energy that is released when calcium-, oxygen- and tungsten ions are stopped in $CaWO_4$. This ionization fraction further subdivides into the ionization of the primary nucleus itself and that of recoil nuclei which left their lattice sites in close encounters. Since the total energy fraction for vacancy production is always smaller than 2%, the remainder of the energy fraction can be attributed to the generation of phonons both from the primary and the secondary ions. At

first sight, the low portion of phonon production seems to be contradictory to a heat quenching $Q' \approx 1$, deduced from the stopping of α-particles in $CaWO_4$ [6] as well as in many other experiments (e.g. [1], [39]). This effect will be discussed in Subsection 7.4.4.

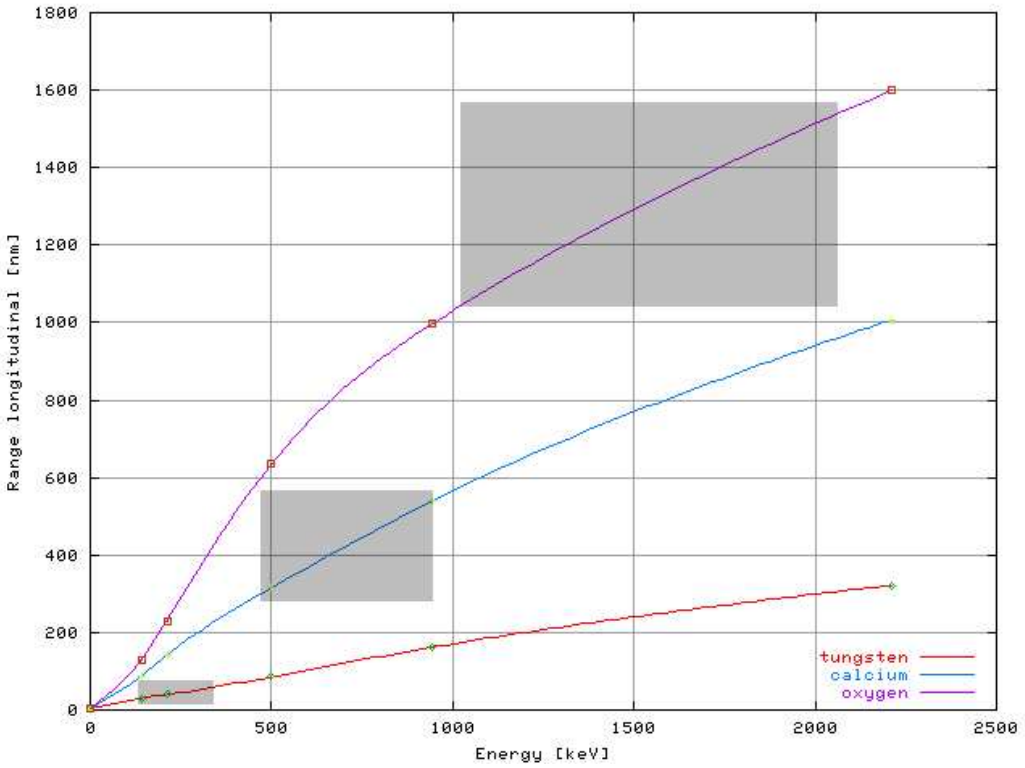

Figure 4.2: Simulated longitudinal range of calcium-, oxygen- and tungsten-ions in $CaWO_4$. The shaded areas comprise recoil energies realized in various beamtimes. The longitudinal range is the range of the cascade projected in the original direction of the ion.

Figure 4.2 shows the ranges of calcium-, oxygen- and tungsten-ions in $CaWO_4$ versus the primary (recoil) energy of the ion. The *longitudinal range*, displayed in this figure, refers to the direction of the primary recoil, i.e. the direction of the incident neutrons in a scattering experiment. The shaded regions mark the energies transferred by recoils from neutron scattering in our experiment and the associated calculated longitudinal ranges. Within the energy ranges that are realized in the experiment, the longitudinal range is proportional to the primary energy to a quite good approximation. The proportionality constant is the mean longitudinal energy loss of the ion, $\mathrm{d}E/\mathrm{d}x$, which is also listed in Table 4.4. This energy loss will emerge from the deriva-

	I(p)/I(p+c) [%]	I(p+c) [%]	Range [nm]	Energy/Range [keV/nm]
O-16	99	92-96	997-1600	1.1-1.4
Ca-nat	76	64-72	316-540	1.4-1.7
W-nat	25	28-35	22-41	4.5-5.2

Table 4.4: Ionization, longitudinal ranges and mean longitudinal energy loss of the ions in $CaWO_4$ for an energy transfer due to the deflection of 11 MeV neutrons for scattering angles from 80° to 140°. Both the primary ion (p) and the recoil atoms of the cascade (c) lose energy by ionizing absorber atoms. The fraction of the sum of both contributions and the total energy loss is denoted by I(p+c). The fraction of the ionization that is induced by the primary ion I(p) and the total ionization is denoted by I(p)/I(p+c).

tion and explanation of different Quenching factors of different elements in the same scintillator to be the crucial quantity, as we will further discuss in Section 5.6.

Table 4.4 summarizes the total ionization and longitudinal ranges of the ions in $CaWO_4$ for an energy transfer due to the deflection of 11 MeV neutrons for scattering angles within the range from 80° to 140°. Both the primary ion (p) and the recoil atoms of the cascade (c) lose energy by ionization of the absorber. The fraction of the sum of both contributions and the total energy loss is denoted by I(p+c). The fraction of the ionization that is induced by the primary ion I(p) and the total ionization is denoted by I(p)/I(p+c). For example, the primary energy of an calcium ion leads to about 64-72% energy transfer to the electron system of the absorber ("total ionization"), while the remaining 28-36% are converted into phonons. 76% of the total ionization is caused by the primary calcium ion, while 24% of the total ionization is caused by recoil atoms of the cascade. The fact that the total ionization yield for oxygen, calcium and tungsten are different indicates that the recoil cascade of absorber atoms has to be considered as well as the primary ion for the generation of ionization (see Table 4.4). Otherwise the total ionization yields for oxygen, calcium and tungsten ions would be clearly more similar to each other.

4.4 Radiation interaction

By inelastic nuclear reactions as well as during the energy dissipation process in $CaWO_4$ photons are generated that may be fully or partly reabsorbed in the crystal, or escape it (see e.g. Figure 2.1). When the phonon and photon signals are measured, gamma-rays from inelastic excitations that interact with the crystal shift pure gamma events along the direction of the nuclear recoil band. Thus inelastic reactions with full absorption of a single gamma energy give rise to the occurrence of tails branching off the electronic recoil band (details see [48]). By identification of the inelastic level corresponding to that gamma energy, it is in principle possible to attribute this recoil branch to the element (W, Ca, O in $CaWO_4$) and infer the Quenching factor from the slope of this branch. Such attempts have not been successful up to now due to a too poor light resolution.

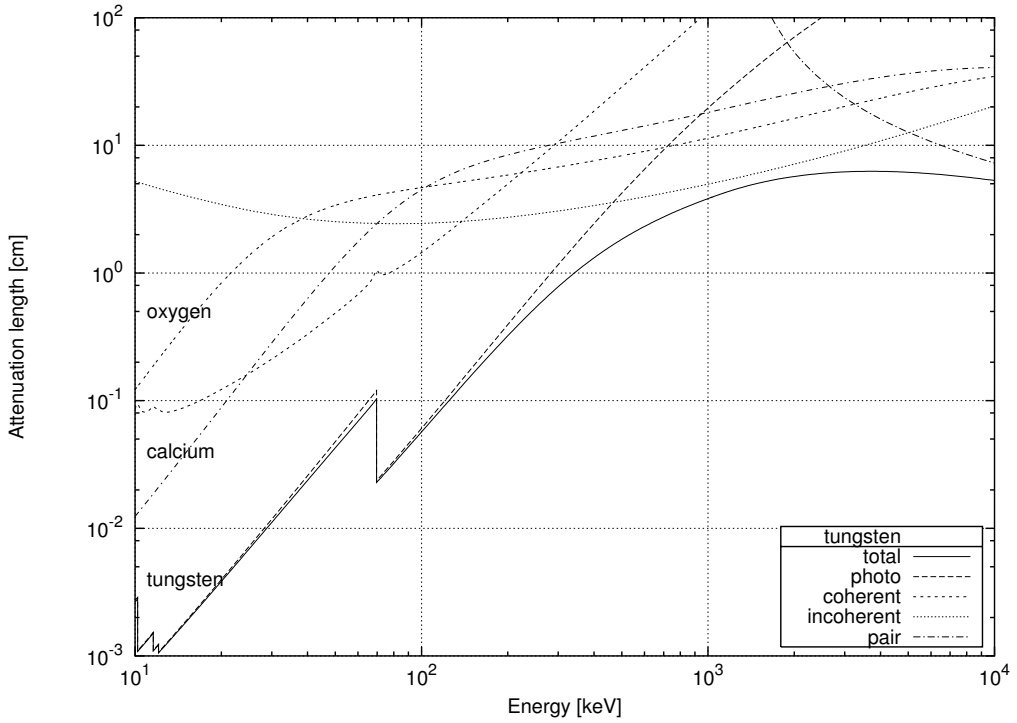

Figure 4.3: Total X-ray and gamma attenuation lengths in $CaWO_4$ for Ca, O and W and different contributions to the total attenuation by tungsten: photoelectric absorption (photo), Thomson (coherent) and Compton (incoherent) scattering, total pair production (pair) in the electron and nuclear field.

If only the scintillation light is measured, the energy of the simultaneous

gamma absorption that follows a nuclear recoil from an inelastic scattering adds to the recoil energy of the nucleus. These events will be shifted along the vertical direction in scatter plots where the amplitude of the scintillation signal vs. ToF is shown (if the energy loss of the neutron is small). The amount of that shift is given by the corresponding (unquenched) gamma energy. If no further discrimination is possible (e.g. via pulse shape discrimination between electron and nuclear recoils), these events contribute significantly to the background in these plots and make data interpretation more difficult (a discussion of this case is given in Subsection 7.4.3 for inelastic reactions from tungsten).

In order to estimate the X-ray and gamma absorption probabilities, the different contributing processes need to be calculated, see Figure 4.3.

Chapter 5

Scintillation mechanisms

The investigation of scintillation light quenching from nuclear recoils is one of the keys for an efficient background rejection in CDM particle detectors that utilize scintillators. An understanding of the underlying physical processes would be of great help in the prediction of unknown quenching factors (QF's) in any kind of material, since the measurement of QF sometimes requires a great deal of experimental effort. The general understanding of scintillation could help in the choice of a certain scintillator when special requirements need to be met (e.g. concerning scintillators with a certain mass or spin of the atomic nuclei, radiopurity etc.); it could help in the prediction of temperature and energy dependence if data exist in a restricted temperature or energy range. Finally it would help in finding answers, how and which detector processing might worsen or even improve the light yield and which precautions need to be taken in the production and handling of the scintillator.

Although scintillation detectors are one of the oldest tools in radiation and particle detection, many of the fundamental processes are still not very well understood. This chapter gives an overview about the multifarious mechanisms of scintillation processes that are involved in the scattering experiment. Not only the detectors that are used for Dark Matter Searches like crystalline $CaWO_4$ and NaI(Tl) use scintillation, but also the liquid NE213 scintillators, used for the detection of scattered neutrons in our setup. There are liquids and solid states, crystals and amorphous materials, organic and inorganic materials, doped or not, that show scintillation, some in a restricted temperature range. The common features to all scintillating materials allowing for the use as detectors will be revealed in this chapter: the existence and preference of certain electronic transitions, often used as final transitions in the dissipation process of a chain of higher level excitations, in an energy region where the material is essentially transparent to its own emission wavelength, and the absence of competetive non-radiative (quenching) mechanisms like

phonon production.

The chapter starts with an overview of the scintillation process and the most fundamental way to excite it, i.e. by photoabsorption. The neutron detectors used in the scattering experiment are capable of disriminating nuclear from electron recoils by different pulse shapes of the emitted light. This capability arises from scintillation processes known as delayed fluorescence and phosphorescence, processes that depend characteristically from the density of energy deposition and excitation careers. The same dependence holds for the reduced light output (quenching) from nuclear recoils. Several mechanisms for quenching and their dependences will be discussed in the subsequent section, followed by an overview of the scintillation light production in organic (aromatic) materials. Here certain symmetry properties of loosely bound π electrons are responsible for the scintillation light emission. While $CaWO_4$, the most important scintillator investigated in this work since it is used in the CRESST dark matter search, is of completely different material structure (inorganic crystal instead of organic liquid), again π electrons of the oxyanion WO_4^{2-} are responsible for the scintillation light emission. Finally, Birk's formula will guide us to a more quantitative formulation of scintillation quenching and will provide the explanation for mass and energy dependence of the quenching factors measured in our experiment.

5.1 Photo-luminescence

The energy system of any molecule can suitably be represented by a potential energy diagram. Although the exact shapes of these potentials are known for only a few simple molecules, the general form is similar to that shown in Fig. 5.1 for a diatomic molecule OA. The interatomic distance is represented along the x-axis and the energy along the y-axis. The curve aAa' determines the vibration amplitudes of atom A relative to atom O for all vibrational energies of the neutral molecule in the electronic ground state. A molecule in thermal equilibrium at room temperature will possess only a few quanta of vibrational energy, represented by the two levels near A. The upper curve bBb' similarly represents the vibrations of a molecule in an excited electronic state. The two levels near B represent the normal vibrational states when the excited molecule is in thermal equilibrium. The minimum of the potential B is displaced to the right of A due to the increase in bond length.

The absorption of a photon by the molecule can cause a transition from the ground state aAa' to bBb'. Such a transition will occur along a vertical line on the diagram, since the electronic change is more rapid than the atomic movements (*Franck-Condon* principle). The transition from A to D raises

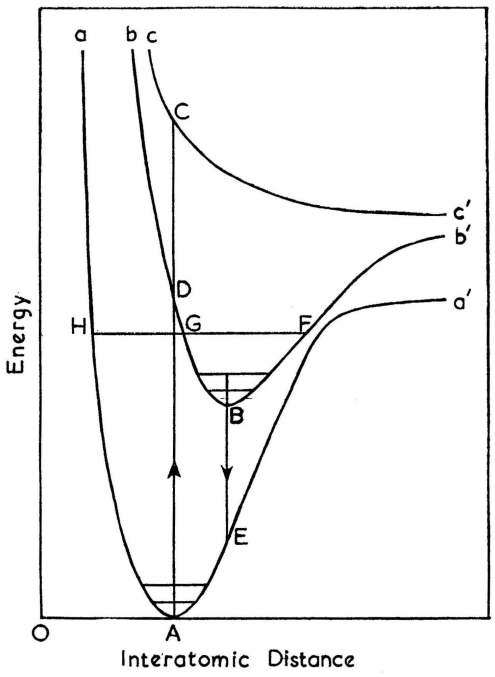

Figure 5.1: Molecular potential energy configuration [4].

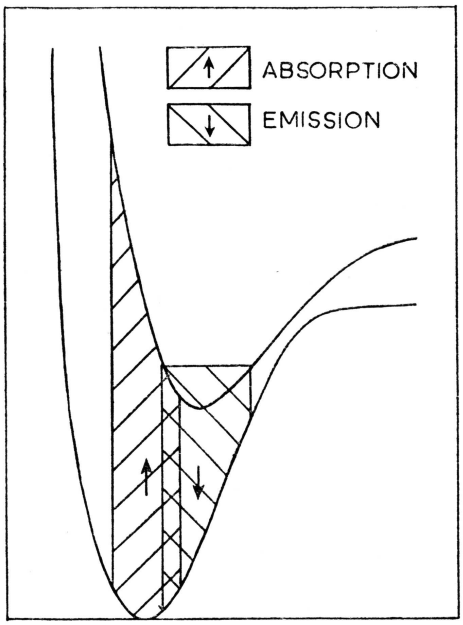

Figure 5.2: Absorption and emission transitions.

the molecule into the excited electronic level bBb'. If D is above the limit b' dissociation will occur, otherwise the molecule will be in a high vibrational level of bBb'. It will dissipate its excess vibrational energy rapidly as heat and fall to the point B. If the molecule is sufficiently stable, it may return to the ground-state along the line BE, under emission of fluorescence light. The fluorescence mean life time is long compared to the period of the molecular vibrations, and hence fluorescence only occurs in molecules in which the energy is not readily dissipated in other ways.

The general nature of the fluorescence and absorption spectra can be understood from a consideration of the potential diagram redrawn in Fig. 5.2. The *absorption* spectrum, corresponding to the transition form the ground state to the first excited state, is due to transitions form the first few vibrational levels of A up to bBb'. The *fluorescence* spectrum, corresponding to the reverse process, is due to transitions from the first vibrational levels of B down to aAa'. Due to the displacement of B towards longer interatomic distances (to the right of A), the fluorescence spectrum is shifted to the long wavelength side of the absorption spectrum, though there is usually a certain overlap. Additional intense absorption bands occur at shorter wavelengths,

due to transitions into the second and higher electronic states. The normal fluorescence spectrum on the other hand only corresponds to transitions from the first excited state to the ground state, and no fluorescence corresponding to transitions between any other electronic states has yet been observed.

It has been found experimentally [4], at least for organic crystalline phosphors, that the quantum efficiency of fluorescence (number of quanta emitted / number absorbed) is independent of the wavelength of the exciting light down to at least 2500 Å. This means that the fluorescence can be produced with equal efficiency by excitation into the second or higher electronic excited states. The transition from these higher states to the first electronic excited state must therefore occur with 100% efficiency.

The third curve cCc' in Fig. 5.1 represents a higher excited state in which the inter-atomic attraction is changed to repulsion. The curve has no minimum as there are no stable vibrational levels. The transition from A to C, corresponding to the absorption of a high energy photon, causes photochemical dissociation of the molecule into atoms, as represented by the passage along Cc'. The electronic energy, represented by the ordinate C, is converted into chemical energy, given by the ordinate of c', the remainder going into the translational energy of the atoms.

5.2 Delayed fluorescence

The fluorescence process in organics as well as in $CaWO_4$ arises from transitions in the energy level structure of a single molecule and therefore can be observed from a given molecular species independent of its physical state. For example, the absorption of $CaWO_4$ is comparatively invariant, not only with changes in the chemical composition, but also with changes in the state of aggregation (crystalline state, solutions [22]). Moreover, tungstate scintillators with different metal ion have essentially common properties. Therefore, the configuration responsible for both, absorption and emission, must be a constituent common to all the various systems, which is obviously W with adjacent oxygen ions. This behavior is in marked contrast to a kind of crystalline inorganic scintillators such as sodium iodide, which require a regular crystalline lattice as a basis for the scintillation process.

In general the light emission process may be more complicated than discussed in the introduction of this chapter: it may also involve intermediate states [22]. For instance it can happen that an excited state exists below the normal excited state which is reached in the excitation process. Instead of returning to the ground state, the system may fall to this intermediate state (Figure 5.3). We shall discuss this case for the neutron detector scin-

tillator (Section 5.4) with regard to the technical application of pulse shape discrimination.

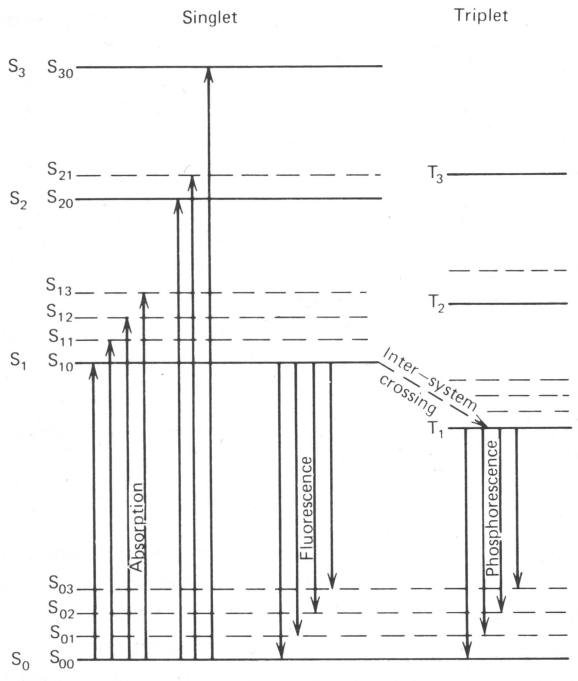

Figure 5.3: Energy levels of a molecule with π-electron structure [20]. For more details, see Section 5.4. S_0 and S_1 correspond to A and B in Figure 5.1.

Because the spacing between vibrational states is large compared with average thermal energies (0.025 eV), nearly all molecules are in the S_{00} state at room temperature. In Figure 5.3 the absorption of kinetic energy from a charged particle passing nearby is represented by arrows pointing upward. The higher singlet electronic states that are excited quickly (on the order of picoseconds) de-excite to the S_1 electron state through radiationless internal conversion. Furthermore, any state with excess vibrational energy (such as S_{11} or S_{12}) is not in thermal equilibrium with its neighbors and again quickly loses that vibrational energy. Therefore, the net effect of the excitation process is to produce, after a negligibly short period of time, a population of excited molecules in the S_{10} state.

The principal scintillation light (or *prompt fluorescence*) is emitted in transitions between this S_{10} state and one of the vibrational states of the ground electronic state. The lifetime for the first triplet state T_1 is characteristically much longer than that of the singlet state S_1. Through a transition called "intersystem crossing", some excited singlet states may be converted into triplet states. The lifetime of T_1 may be as long as 10^{-3}s and the radiation emitted in a de-excitation from T_1 to S_0 is therefore a delayed light

emission characterized as *phosphorescence*. Because T_1 lies below S_1, the wavelength of this phosphorescence spectrum will be longer that that for the fluorescence spectrum. While in the T_1 state, some molecules may be excited back to the S_1 state via energy transfer from other excited molecules and subsequently decay through normal fluorescence. This process represents the origin of *delayed fluorescence*.

5.3 Quenching

The *scintillation efficiency* of any scintillator is defined as the fraction of all incident particle energy which is converted into visible light [20]. One would always prefer this efficiency to be as large as possible, but unfortunately there are alternate de-excitation modes available to the excited molecules which do not involve the emission of light and in which the excitation is transformed mainly to heat. All such radiationless deexcitation processes are grouped together under the term *Quenching*.

5.3.1 Thermal Quenching

Considering Fig. 5.1, in many molecules the curves bBb', aAa' approach closely at some point F, and a molecule in the excited electronic state vibrating along GF may make a radiationless transition to the high vibrational level FH of the ground electronic state, and then dissipate the excess vibrational energy thermally. A rise in temperature, causing increased thermal agitation of excited molecules into the level FGH, increases the probability of this Quenching process, and reduces the fluorescence efficiency. Molecular interactions and collisions, which tend to broaden the curves aAa' and bBb' and cause merging at F, similarly increase the Quenching of the fluorescence.

The intensity of luminescence as a function of temperature consists of a flat part at high intensity in the low temperature region and an adjoining S-shaped part in the upper temperature region. This temperature dependence of the scintillation efficiency of $CaWO_4$ is independent of the method of excitation and is also the same for different intensities of the exciting radiation [22]. Different samples, however, may show differences in behaviour owing to differences in the perfection of the crystals. Badly crystallized products are only luminescent at low temperatures. This explains the fact that freshly precipitated $CaWO_4$ is non-luminescent at room temperature. When the product is heated to high temperatures, or even when it is kept long enough at room temperature, the crystals grow more perfect (cf. Section 4.2) and the quenching rapidly approaches a constant value. Therefore with normally

prepared $CaWO_4$ luminophors always the same quenching range is found.

5.3.2 Quenching dependences

Considering the light ouput from charged recoil nuclei there might be a directional variation of the light output which depends on the orientation of the path of the nucleus with respect to the crystal axis. [14] found deviations of about 4% both in the decay constants and pulse heights for ^{23}Na and ^{127}I recoils in NaI(Tl) generated along different crystal orientations. According to [20], it is not unusual to observe variations as large as 20-30% as the charged particle orientation is varied. This directional variation spoils the energy resolution obtainable if the incident radiation will produce tracks in a variety of directions within the crystal.

Concerning decay-times, the technical fluorescence decay time may be increased due to self-absorption ([4]).

5.4 Organic Scintillators

A large category of practical scintillators is based on organic molecules with certain symmetry properties and a π-electron structure. The π-electronic energy levels of such a molecule are illustrated in Figure 5.3. Energy can be absorbed by exciting the electron configuration into any of a number of excited states. A series of singlet states (spin 0) are labeled as $S_0, S_1, S_2, ...$ in the figure. A similar set of triplet (spin 1) electronic levels are also shown as $T_1, T_2, T_3, ...$. For molecules of interest, e.g. aromatics, the energy spacing between S_0 and S_1 is of the order of 3 to 4 eV, whereas spacing between higher-lying states is usually somewhat smaller. Each of these electronic configurations is further subdivided into a series of levels with finer spacing which correspond to various vibrational states of the molecule. Typical spacing of these levels is of the order of 0.15 eV. A second subscript is often added to distinguish these vibrational states. The symbol S_{00} then represents the lowest vibrational state of the ground electronic state S_0.

For the vast majority of organic scintillators, the prompt fluorescence represents most of the observed scintillation light. A longer-lived component is also observed e.g. in the case of NE 213, corresponding to delayed fluorescence. The composite yield curve can be represented adequately by the sum of two exponential decays – called the fast and slow components of the scintillation (details see Chapter 6, especially Equation (6.4)). While the prompt decay time is only a few nanoseconds, the slow component has a characteristic decay time of several hundred nanoseconds (cf. Table 6.3). Since the

majority of the light occurs in the prompt component, the long-lived tail would not be of great consequence except for one very useful property: The fraction of light that appears in the slow component depends on the nature of the exciting particle. One can therefore make use of this dependence to differentiate between particles of different kinds which deposit the same energy in the detector. This process is called *pulse shape discrimination (PSD)* and is widely applied to eliminate gamma-ray-induced events when scintillators are used as neutron detectors or vice versa.

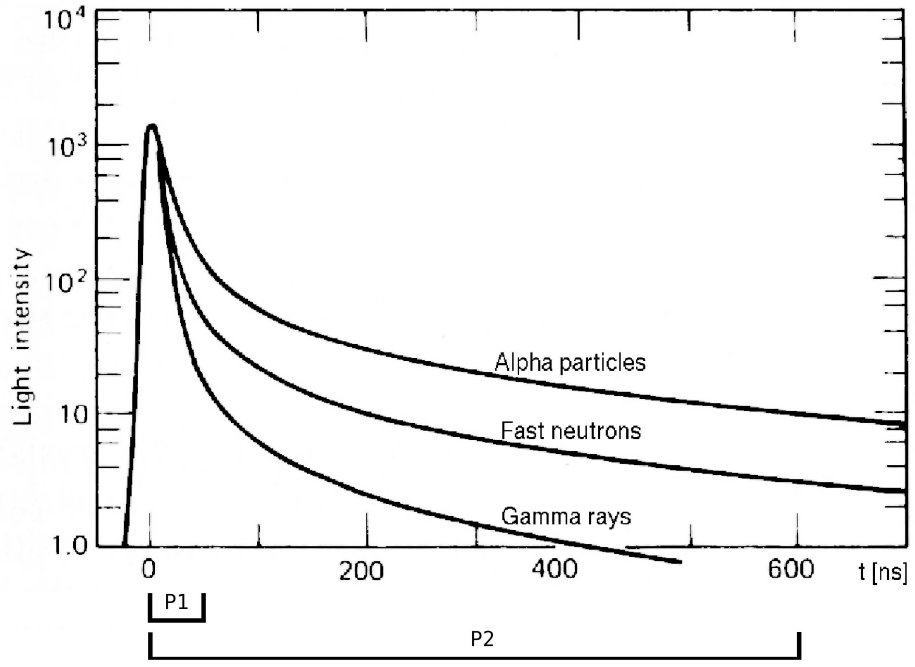

Figure 5.4: The time dependence of scintillation pulses in NE213 (equal intensity at time zero) when excited by radiation of different types.

There is strong evidence that the slow scintillation component originates from the excitation of long-lived triplet states (labeled T_1 in Figure 5.3) along the track of the ionizing particle. Bimolecular interactions between two such excited molecules can lead to product molecules, one in the lowest singlet state (S_1) and the other in the ground state. The singlet state molecule can then de-excite in the normal way, leading to delayed fluorescence. The variation in the yield of the slow component can then be partially explained by the differences expected in the density of triplet states along the track of the particle, because the bimolecular reaction yield should depend primarily on the rate of energy loss $\mathrm{d}E/\mathrm{d}x$ of the exciting particle and should be

greatest for particles with large $\mathrm{d}E/\mathrm{d}x$.

5.4.1 Energy transport

In almost all organic materials, the excitation energy undergoes substantial transfer from molecule to molecule before de-excitation occurs [20]. This energy transfer process is especially important for the large category of organic scintillators which involves more than one species of molecules. If a small concentration of an efficient scintillator is added to a bulk solvent, the energy that is absorbed, primarily by the solvent, can eventually find its way to one of the efficient scintillation molecules and cause light emission at that point.

A third component is sometimes added to these mixtures to serve as a "wave length shifter" [20]. Its function is to absorb the light produced by the primary scintillant and re-emit it at a longer wavelength. This shift in the emission spectrum can be useful for closer matching to the spectral sensitivity of a photomultiplier tube or for minimizing bulk self-absorption in large scintillators.

5.5 $CaWO_4$

Calcium tungstate ($CaWO_4$) crystallizes in the tetragonal scheelite structure at ambient conditions [13]. From the cationic point of view, the scheelite structure consists of two intercalated halfs of one diamond lattice: one for Ca cations and another for W cations (see Figure 5.5), where the Ca-Ca distances and W-W distances are equal. In the scheelite structure calcium cations are coordinated by eight oxygen anions, thus forming CaO_8 polyhedra. On the other hand, tungsten cations are coordinated by four O anions forming relatively isolated WO_4 tetrahedra. Fig. 5.5 shows a detail of the scheelite structure with the CaO_8 and WO_4 polyhedra.

Bond length and ionic radii are quoted in Table 5.1. In $CaWO_4$, the Ca-O bonds are highly ionic while W-O bonds are covalent in character [13]. There are still some very fundamental questions concerning the electronic properties of scheelites, especially concerning the nature of the states of the ideal crystal in the vicinity of the band gap.

Figure 5.6 compares the calculated total density of states [52] within a 110-eV range, with zero energy set at the top of the last occupied band. The upper core states are labeled according to their dominant atomic character. The one-electron energies of the upper core states including W $5s$, W $5p_{1/2,3/2}$, W $4f_{5/2,7/2}$, Ca $3s$, Ca $3p$, and O $2s$ states have very small relative chemical

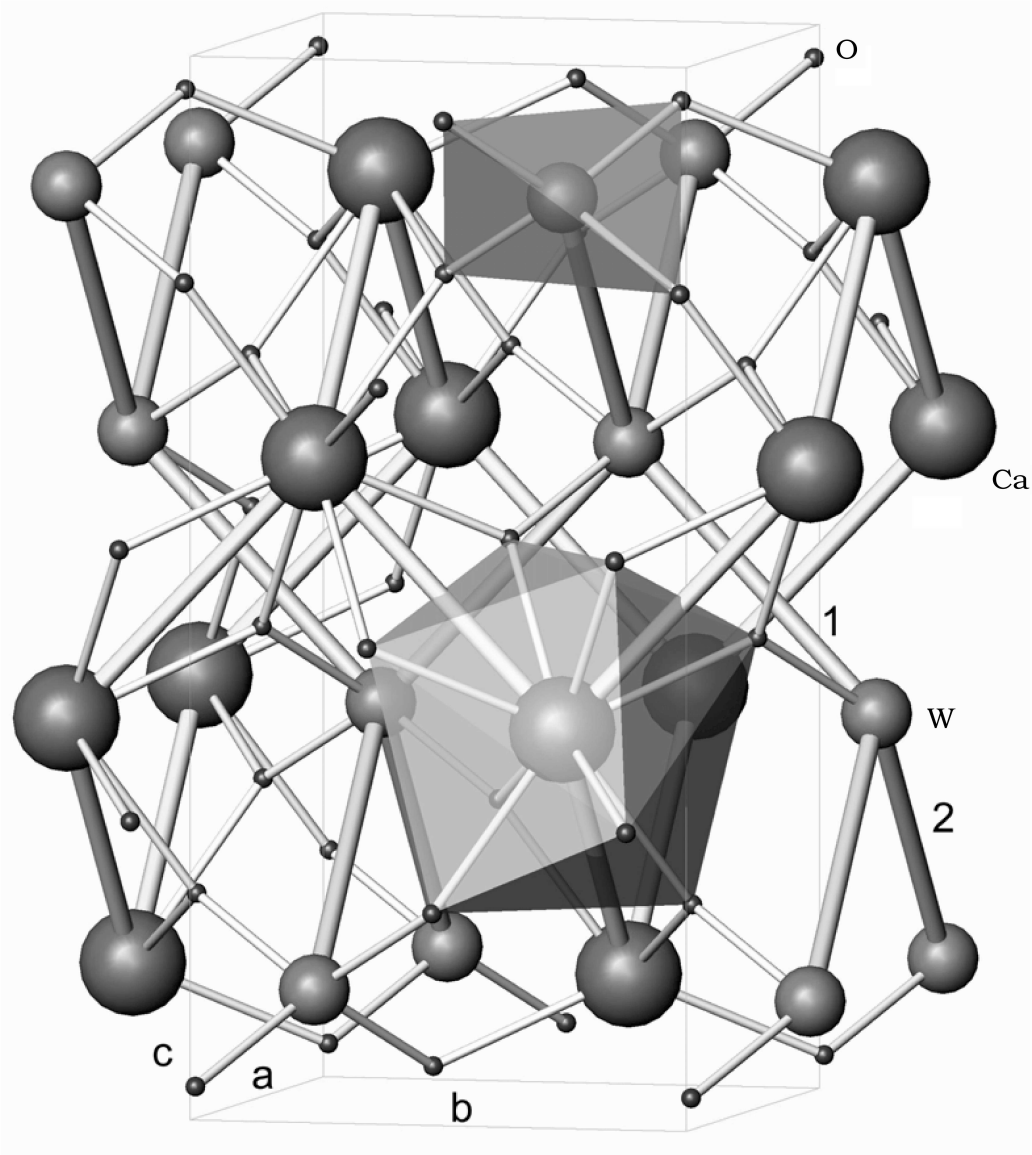

Figure 5.5: Unit cell of the scheelite structure of $CaWO_4$ compounds with the a, b and c axis [13]. Big spheres indicate Ca cations, medium-size spheres correspond to W and small spheres to O anions. Numbers 1 and 2 correspond to W-W distances of the diamond-like structure along $b + c$ and $a + c$ directions, respectively. The CaO_8 polyhedra and the WO_4 tetrahedra are shown.

shifts in $CaWO_4$. The O $2s$ states are among the upper core states forming a narrow band having a width of about 2 eV.

number density	$1.3 \cdot 10^{22}$ molecules/cm^3
W-O bond length	1.798 Å
Ca-O bond length	2.293 Å
O electronic configuration	[He] $2s^2 2p^4$
Ca electronic configuration	[Ne] $3s^2 3p^6$ [Ar] $(4s^2)$
W electronic configuration	[Kr] $4d^{10} 5s^2 p^6$ [Xe] $4f^{14}(5d^4 6s^2)$
Ca ionic radius	1.12 Å
a cell dimension	5.24 Å
c cell dimension	11.37 Å
Exciton reflectance peak	5.9 eV $\widehat{=}$ 210 nm
luminescence excitation threshold	4.8 eV $\widehat{=}$ 260 nm
peak fluorescence	2.8 eV $\widehat{=}$ 440 nm

Table 5.1: General Properties of $CaWO_4$: density, bond lengths, ionic radii, electronic configuration (round brackets denote ionization). Unit cell dimensions are given for 293 K [52]. The exciton reflectance peak is temperature independent [18]. The luminescence excitation threshold is given for 80 K [**?**]. The values for the peak of the fluorescence broad line is taken from [45].

The shape of the density of states for the valence band has two main features (Figure 5.7). The lower portion of the band has roughly equal contributions from O and W states per atom, while the upper portion contains states of primarily O character. The bottom of the conduction band is dominated by W states. Additional contributions come from the Ca states at approximately 3-4 eV above the bottom of the conduction band.

On the oxygen-sites, the valence-band states are almost entirely described by atomic-like $2p$ wave functions. The strong crystal field due to the nearby W ions splits the atomic $2p$ states into σ and π contributions. From Figure 5.8 it is apparent that the σ-like contributions are weighted toward the bottom of the valence band and the top of the conduction band, while the π-like contributions are stronger at the top of the valence band and bottom of the conduction band.

The geometry in the vicinity of the W sites is approximately tetrahedral

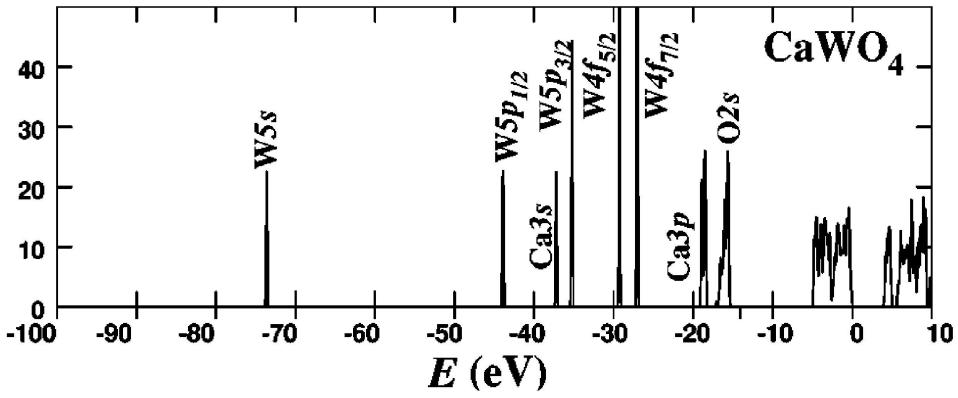

Figure 5.6: Plot of total densities of states per unit cell for a $CaWO_4$ scheelite crystal, including upper core, valence-band, and conduction-band states [52]. Zero on the energy scale is set at the top of the last occupied state. The upper core states are labeled according to their dominant atomic behavior.

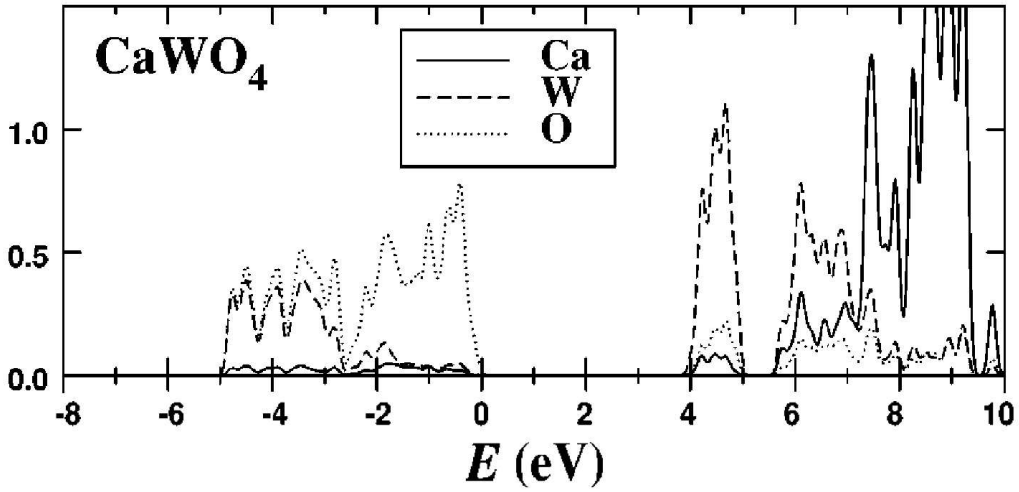

Figure 5.7: Atomic partial densities of states per unit cell for a $CaWO_4$ scheelite crystal [52].

and the $5d$ states split into e- and t_2-like states (non-degenerate mixing of d states in the crystal field approximation, [19]). From Figure 5.8 it is apparent that the bottom of the valence band receives roughly equal contributions from both the e- and t_2-like states, while the top of the valence band receives very little contribution from either symmetry. The bottom of the conduction band, however, is dominated by e-like contributions, while the upper conduction band is dominated by t_2-like contributions.

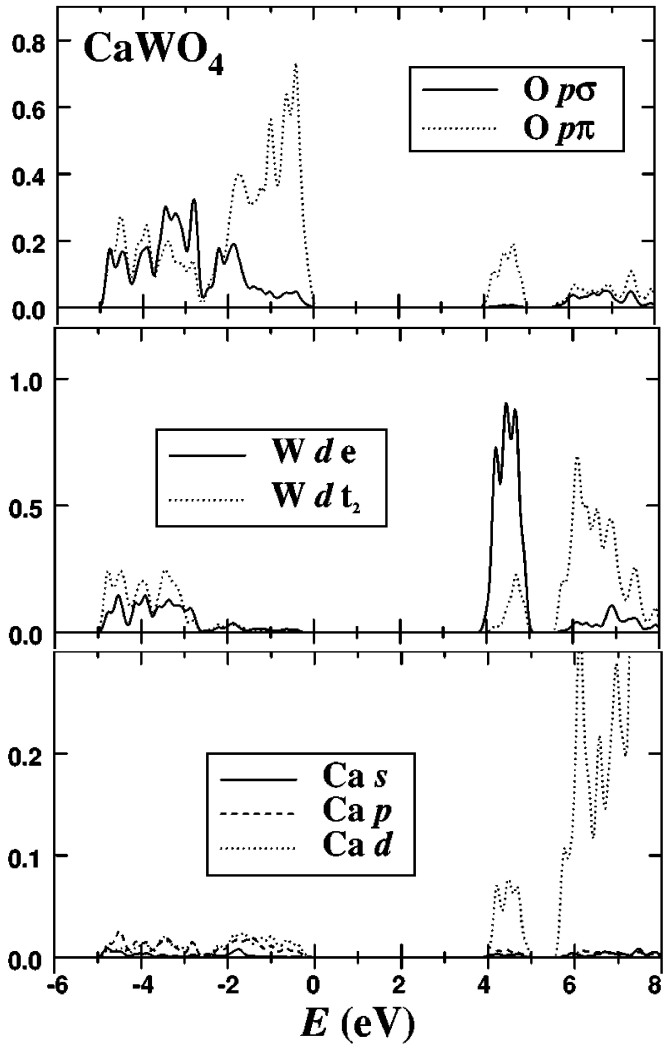

Figure 5.8: Atomic partial densities of states per unit cell for a $CaWO_4$ scheelite crystal [52]. Top: Crystal-field-split O $2p$ partial density of states, weighted by the σ-like (full line) and π-like (dotted line) contributions. Middle: Crystal-field-split W $5d$ partial density of states weighted by the e-like (full line) and t_2-like (dotted line) contributions. Bottom: Ca atomic-orbital partial density of states: The partial density is weighted by the s-like (full line), p-like (dashed line), and d-like (dotted line) contributions.

The Ca $4s$-, $4p$-, and $3d$-like contributions are shown in Figure 5.8, note that the vertical scale has been expanded relative to that in Figure 5.7. This figure shows that there are very little Ca $4s$ and $4p$ contributios to the valence-

and conduction-band states between -6 eV and +8 eV. However, there is a significant contribution of the Ca $3d$ states above the W $5d$ states.

Summarizing, two main types of intrinsic electronic excitations can be distinguished in $CaWO_4$ crystals [30]: One of them is the transfer of an electron from the oxygen O^{2-} to the tungsten ion, the other is the transfer of an electron from oxygen to the Ca^{2+} ion. Electronic excitations of the first type can be considered as various excited states of an oxyanion, measured via reflection spectra of $CaWO_4$ single crystals [18]. The lowest excited states involve one hole in the O $2p\pi$ states and one electron in the e W $5d$ states, where the exciton reflectance peak coincides with the first peak of the luminescence excitation spectrum attributed to the lowest dipole-allowed molecular transition. To make a long story short, the scintillation light emission is due to the lowest electronic transition from a tungsten atom to the adjacent oxygen atoms within the oxyanion complex. While the molecular-orbital model describes the general features of the excitation and luminescence, a more accurate description corresponds to Frenkel-type excitons having energies within the band gap of the one-electron states. The hole localizes on the O_4^{8-} complex, and the resulting Coulomb defect traps a spatially diffuse electron to create a self-trapped exciton (STE) [9, 31, 33].

5.6 Light Quenching

A small fraction of the kinetic energy lost by a charged particle in a scintillator is converted into fluorescent energy [20]. The remainder is dissipated nonradiatively, primarily in the form of lattice vibrations or heat. The fraction of the particle energy which is converted (the scintillation efficiency) depends both on the particle type and its energy. In some cases, the scintillation efficiency may be independent of energy, leading to a linear dependence of light yield on initial particle energy.

For the scintillators investigated in this work, the response to electrons is linear within the respective quoted energy ranges: NE 213 from 125 keV to 4.3 MeV, NaI(Tl) from 60 keV to 1.1 MeV, $CaWO_4$ from 6 keV to 511 keV. The response to heavy charged particles may be nonlinear and is always less for equivalent energies as will be shown in Chapter 7.

Birks was the first who observed a continued decrease in the scintillation efficiency of anthracene during a continued intense α-particle irradiation. No recovery was observed, and a brown discoloration of the irradiated surface layer appeared indicating that the effect is due to a permanent molecular damage [4].

Nonradiative electron-hole pair or exciton-exciton annihilation, and dam-

aged molecular or crystal structures acting as electron or hole traps, collectively referred to as "Quenching mechanisms" in regions of high energy deposition density, are now generally accepted as being the principal causes of a lowering of the scintillation efficiency [27]. In order to describe the effect quantitatively, the response of scintillators to charged particles can best be described by a relation between dL/dx, the fluorescent energy emitted per unit path length, and dE/dx, the specific energy loss of the charged particle [20]. In Birks theory, the passage of an ionizing particle through the crystal produces a number (SdE/dx) of "excitons" (loosely defined as excited or ionized molecular structures for organic materials) proportional to the specific energy loss. Further he assumes that the density of damaged molecules, acting as Quenching agents for the excitons, along the wake of the particle is also directly proportional to the specific energy loss. Then their density can be represented by $B(dE/dx)$, where B is a proportionality constant. Birks assumes further that some fraction k of these will lead to Quenching, i.e. k is the exciton capture probability of a damaged molecule relative to an undamaged molecule. Assuming that the light output is proportional to the effective number of excitons, the specific luminosity is thus given by

$$\frac{dL}{dx} = \frac{S\dfrac{dE}{dx}}{1 + kB\dfrac{dE}{dx}} \tag{5.1}$$

Equation 5.1 is commonly referred to as *Birks' formula*. A consequence of this equation is that, in the absence of Quenching, the light yield is proportional to energy loss:

$$\left.\frac{dL}{dx}\right|_e = S\frac{dE}{dx} \tag{5.2}$$

where S is the normal scintillation efficiency. The same holds for excitations of fast electrons (either directly or from gamma-ray irradiation) where dE/dx is small for sufficiently large values of E. Hence the incremental light output per unit energy loss is a constant

$$\left.\frac{dL}{dE}\right|_e = S \tag{5.3}$$

This is the regime in which the light output

$$L \equiv \int_0^E \frac{dL}{dE}dE = SE \tag{5.4}$$

is linearly related to the initial particle energy E. On the other hand, for a heavy ion, dE/dx is very large so that *saturation* occurs along the track and Birk's formula becomes

$$\left.\frac{dL}{dx}\right|_{\text{ion}} = \frac{S}{kB} \tag{5.5}$$

The values of S and kB are taken from the experiment and depend on the medium through which the incident particle is passing. S can be determined by Equation (5.3), then kB can be determined by Equation (5.5):

$$kB = \left.\frac{dL}{dE}\right|_{e} \Big/ \left.\frac{dL}{dx}\right|_{\text{ion}} \tag{5.6}$$

Integrating Equation 5.5 shows that the light yield L is proportional to the range R of the ion:

$$L = \frac{S}{kB} \cdot R \tag{5.7}$$

The quantity of interest in the scattering experiment is the Quenching factor of ions: $QF = E_{ee}/E$ (Equation 2.1). By definition, $L_{\text{ion}} = SE_{ee}$, and the Quenching factor is

$$QF = \frac{E_{ee}}{E} = \frac{1}{S}\left.\frac{L}{E}\right|_{\text{ion}} \tag{5.8}$$

Applying Equation (5.7) yields

$$\frac{1}{QF} = S\left.\frac{R}{L}\right|_{\text{ion}}\left.\frac{E}{R}\right|_{\text{ion}} = kB \cdot \left.\frac{E}{R}\right|_{\text{ion}} \tag{5.9}$$

Since kB depends only on properties of the material and is therefore constant as long as the Quenching factor of different ions in the same scintillator is considered, the important result is:

The Quenching factor is
inversely proportional to the mean specific energy loss of the ion.

This relation will be confirmed by the measurement of the Quenching factors of Ca, W and O in $CaWO_4$ in Section 7.4 in combination with the ionization and range calculation of Chapter 4.

Chapter 6

Experimental setup

A neutron scattering facility for the measurement of Quenching factors for nuclear recoils in Dark Matter Detectors is installed at the tandem accelerator of the Maier-Leibnitz-Labor (MLL) in Garching, Germany. This chapter describes in detail the experimental setup of this scattering facility. An introduction about the general setup and its motivation was already given in Chapter 2. The requirements of the scattering experiment were deduced to be:

- a mono-energetic neutron source with a neutron energy of the order of 10 MeV
- fixed kinematics by fixing the neutron scattering angle
- pulsing of the neutron source to allow a time-of-flight measurement
- discrimination of neutron and gamma events in the outer detectors

The structure of this chapter follows the path of ions through the accelerator beamline displayed in Figure 6.1.

The chapter starts with a description of the neutron production reaction and its experimental requirements. Then the most important facilities of the accelerator are described with special emphasis on the pulsing devices. Having reached the experimental site of the scattering experiment, the hydrogen target is described where neutrons are generated. The detection of these neutrons is described in the subsequent section. A discussion of the scattering geometry and the data acquisition both in hard- and software follows. At the end of this chapter a detailed description of the scintillation detection is provided.

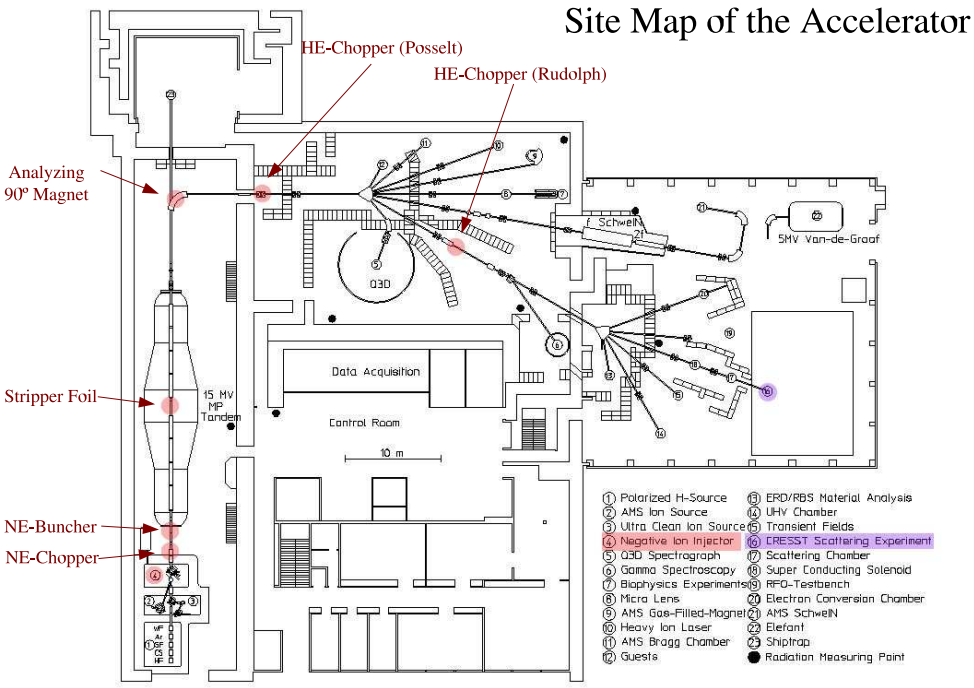

Figure 6.1: Site map of the accelerator with marks of the location of special devices described in the text.

6.1 Monoenergetic neutron source

A neutron source is considered monoenergetic when the energy spectrum consists of a single line with an energy width which is much less than the energy itself. In principle, such monoenergetic neutrons can be produced by two-body reactions in an accelerator. However, a practical source will not only produce these "primary" neutrons, but also "background" neutrons of lower energy, resulting from beam interactions in the accelerator and in the target structure or from interactions of the primary neutrons with the room structures (beam connected room background, inscattered neutrons). In addition, there may be a source intrinsic background of (secondary) neutrons. This background either consists of lines originating from other two-body reactions, of an energy distribution of more-body reactions (break-up) or of the satellite line as a result of kinematic collimation (see below).

As discussed in Chapter 2, the neutron energy required is determined by the expected WIMP recoil energy deposition in $CaWO_4$. Once the neutron production reaction is chosen, the neutron energy can still be adjusted to a

certain extent by the selection of the neutron emission angle. The optimal choice of the relation input energy and scattering angle is given by geometrical constraints in terms of maximum neutron flux (cf. Section 6.3) and largest possible cross section under that detection angle. At best the pair input energy/scattering angle is chosen from an optimization of the ratio of elastic against undiscriminable inelastic cross sections. Referring to Figure 3.6 the first side-maximum of the differential cross section for elastic scattering by tungsten was selected, requiring a neutron energy of 11 MeV.

Usually fast monoenergetic neutrons are produced by nuclear reactions like D(d,n)^{3}He, T(d,n)^{4}He, T(p,n)^{3}He or ^{7}Li(p,n)^{7}Be [39]. However, in the energy region between about 8 and 14 MeV these reactions cannot produce really monoenergetic neutrons because of the break-up of the projectile and/or the target nucleus [5]. Consequently, only few experiments about neutron production reactions exist in the "gap" region where only one monoenergetic alternative is at hand, namely ^{1}H(t,n)^{3}He (for energies up to 17.6 MeV). Due to the radioactivity of the projectiles the use of this alternative has been quite limited despite its outstanding specific neutron yield at 0° [11].

6.1.1 The p(^{11}B,n)^{11}C reaction

Heavy ion accelerator technology makes new types of monoenergetic neutron generators feasible, where light nuclei (mass m_{target}) are used as target material for incident heavy ion beams (mass m_{proj}). If $m_{\text{proj}} \gg m_{\text{target}}$, the large velocity of the center-of-mass (CM) plays an important role (Equation (A.7)) as can be seen from the following discussion. The kinetic energy of the whole system E_M is approximately given by the kinetic energy E_{k1} of the incident particle in the laboratory frame:

$$E_M \approx E_{k1} \tag{6.1}$$

This type of projectile and target ion selection is commonly referred to as "inverse kinematics". As a result of the high E_M, there is only relatively little energy $E_{k1}^{(M)}$ available in the CM system (Eq. (A.13)), roughly

$$E_{k1}^{(M)} \approx E_{k1} \cdot \frac{E_{02}}{(E_{01} + E_{02})} \approx \frac{E_{k1}}{A_1} \tag{6.2}$$

with A_1 being the atomic number of the projectile. This type of neutron source has the following advantages:

(a) Monoenergetic neutrons can be produced to much higher energies making use of the high CM velocity (Equation (A.12)). For example for

the non-inverse reaction ^{11}B(p,n)^{11}C, the maximum energy for neutron production where no levels in ^{11}C are excited (derived by means of Eq. (A.28)) is E_n = 2.39 MeV for a threshold proton energy of $E_{p,th}$ = 5.197 MeV , but E_n = 11.859 MeV for the inverse reaction ($E_{B,th}$ = 57.168 MeV) [54].

(b) The large velocity of the center of mass and the low energy in the CM system for the reaction result in high neutron energies without breakup of the projectile. For example, for the non-inverse p – ^{11}B reaction a neutron continuum from breakup occurs at primary neutron energies above 8.47 MeV, whereas the inverse reaction is free of this continuum up to 32.6 MeV.

(c) In an endothermic reaction, the velocity of the produced neutron does not exceed the CM velocity as schematically shown in Figure A.1. Thus, in the laboratory system, neutrons are only emitted at angles smaller than ϑ_{max}. In this situation, neutrons are "kinematically collimated" into a forward cone. In addition, the *source* reaction causes no background in the detectors for the scattered neutrons if these detectors are put in this angular range, i. e. $\vartheta > \vartheta_{max}$. Therefore, the signal-to-background ratio increases remarkably. Moreover, the shielding of the neutron detectors is simplified and the background due to the surrounding material of the experiment is minimized.

(d) The compression into the forward cone strongly enhances the 0° laboratory cross section, whereas the 180° (center-of-mass) cross section, which determines the intensity of the satellite neutron line and gives also a contribution at 0° in the laboratory system (see below), is reduced. Thus the satellite line may be disregarded as small disturbance.

(e) The Coulomb barrier for heavy projectiles is much larger than that of the usually used hydrogen projectile, so that a smaller background of neutrons produced from the beam stop can be expected.

The main deficiency for monoenergetic neutron sources is the occurrence of two neutron energies for all angles less than ϑ_{max}, as discussed in appendix A and illustrated in Figure A.1. This neutron group is commonly referred to as "satellite" neutrons. However, both the energy and yield of the satellite group is considerably smaller than those of the primary neutron group.

Among the many candidates of inverse (p,n) reactions which could give monoenergetic kinematically-collimated neutrons, the one with ^{11}B is expected to be the best at 11 MeV since it matches the prime goals of a true high-energetic monochromatic neutron production reaction:

(a) Greatest possible energy spacing between the ground and the first excited state of the daughter nucleus formed (i.e. ^{11}C: 2000 keV for the reaction discussed in this section). This is important to prevent the production of neutron groups emitted with lower energy, leaving an excited daughter nucleus behind that subsequently decays by gamma-emission: e.g. ^{1}H(^{11}B,n$_i$)^{11}C* in Figure 6.2.

(b) The (negative) Q-value of the nuclear reaction should be as large as possible to allow kinematically collimation from ground state neutron emission at high energy. The threshold energy for the excitation of the first level is then calculated using Equation (A.28) by adding the Q-value of the ground nucleus reaction (e.g. -2764 keV for the discussed reaction) to the Q-value required for the 1. level excitation: ΔQ_1 = -4764 keV for our reaction. Hence for neutron energies above 11859 keV also a neutron group from the first excited level appears (cf. Eqs. (A.22) or (A.25)).

The kinematic properties and the yield from the ground state reaction is shown in Figure 6.2. Special attention deserves the fact that both the energy and the specific yield of the satellite line decreases strongly with energy. Especially around the resonance at 11.4 MeV (with a width (FWHM) of 0.8 MeV) the ^{11}B$-^{1}$H source is a powerful source in the energy gap mentioned above. The required ^{11}B net energy of 55.4 MeV is just inside the voltage range of the tandem Van de Graaff accelerator in Garching.

6.1.2 The tandem accelerator

Injector

To make use of twice the terminal high voltage, negative ions (in our case BO^- or B^-) need to be extracted from a source pill. This is carried out by sputtering Cs^+ ions onto the surface of the pill: Cs is heated, the neutral vapour gets into contact with an ionizer at 1400°C which is at the same electric potential where Cs^+ ions are generated. By means of a voltage between target pill and Cs-heater ("Source Voltage") the Cs^+ ions are accelerated towards the target where they knock out neutral target (B) atoms and stay on the target surface building a film with a thickness of a few atomic layers. Sputtered B atoms penetrate this film and pick up an additional electron (B^-) from the Cs film due to the negative potential with respect to the heater and further positive extraction voltage. ^{11}B isotopes are selected by magnetic deflection. Having left the injector site they are again accelerated towards the low-energy chopper via the pre-acceleration voltage. In our case,

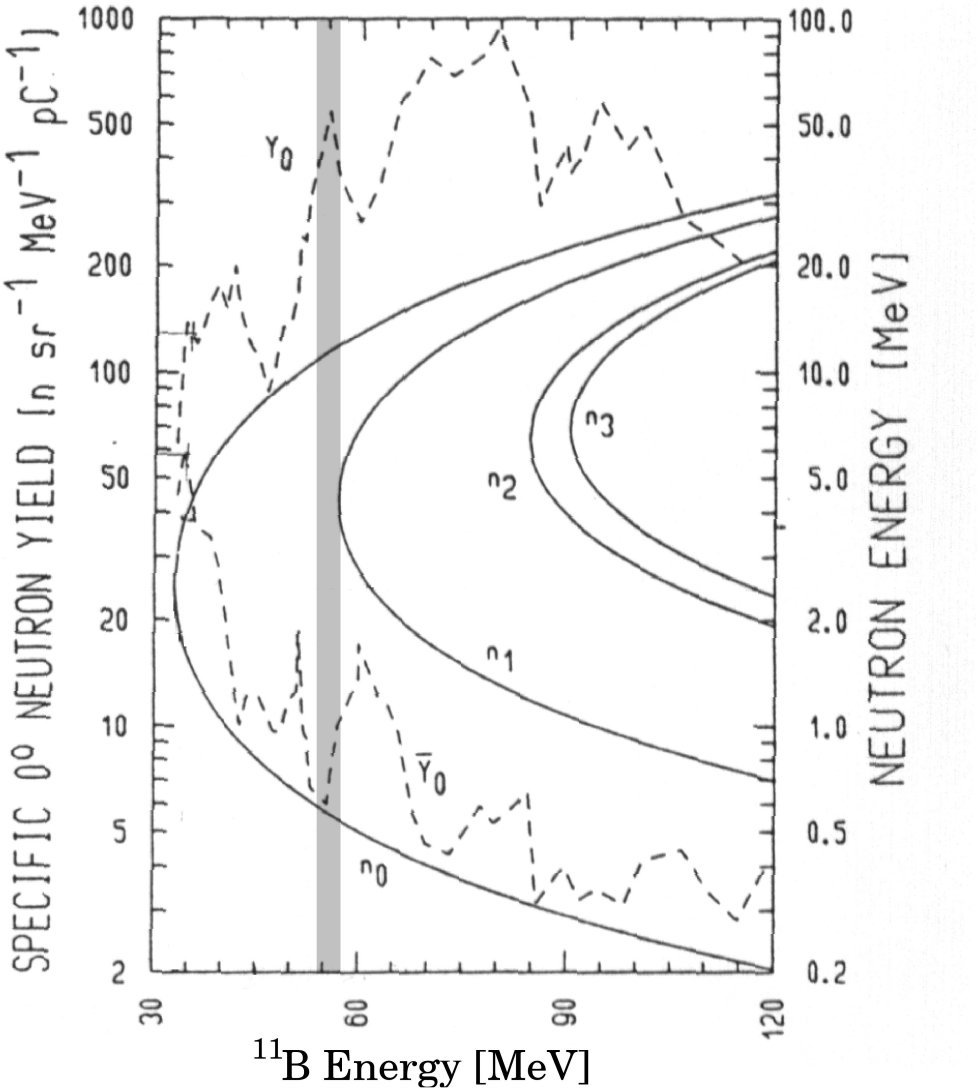

Figure 6.2: Energy dependence of the neutron energies (solid curves) of the ^{1}H(^{11}B,n)^{11}C reaction (populating the four lowest levels in ^{11}C indicated by the labels n_0,n_1,n_2,n_3). The dashed curves gives the specific 0° yield of the high energy branch (Y_0) and the low energy branch $\bar{Y_0}$ of the n_0 neutron group [10]. The shaded area indicates the relevant region that was chosen for the neutron production: a resonance in the production yield of the fast neutron group (Y_0) and a minimum in the production yield of the slow neutron group ($\bar{Y_0}$). The production of neutrons from the first excited state n_1 is only just not possible due to its slightly higher reaction threshold.

from the cesium sputtering source, typically –600 nA ("particle current" due to single negative charge) were extracted with a pre-acceleration energy of 150 keV.

Low-energy chopper

This B^- beam is then chopped by means of a low-energy (*LE*) chopper operated by an oscillator at a frequency determined by $2.5/2^i$ MHz, $i = 0, 1, 2, \ldots$. The value of i has been called "Untersetzung". The task of the LE chopper is to match experimental bunch separation requirements, i.e. to cut the DC particle flux into packets (*bunches*) of adjustable separation ($400 \cdot 2^i$ ns) with a packet width of 100 ns. This width is determined by the maximum buncher input acceptance (depending on its operation frequency).

The LE chopper is in principle a pulsed electrostatic steerer in combination with an aperture. It consists of 5 capacitors with plates ("Platten") on opposite sides charged to ±400 V, while the delays of neighboring capacitors have to be adjusted differentially to the particle transversal energy ("Plattendelay"). The voltage impulse width of the capacitors must also be adjusted to particle velocity ("Impulsbreite"). The ion transmission is established when the HV rectangular impulses switch to zero, for one capacitor after another. The division of the chopper into five deflection capacitors is necessary because LE ion velocities (3 (Au) -50 (H) mm/ns) are of the same order as plate dimensions (50 mm) divided by bunch widths. Since there will be no ion transmission through the chopper when the ion's time-of-flight (ToF) is greater than the impulse width, a ToF between 10 and 20 ns ($\ll$ 100 ns) is desirable. Different ions and energies throughout the accelerator pulsing facilities are synchronized by means of an adjustable delay ("Delay") of the complete LE chopper signal versus a master clock.

Buncher

The task of the buncher [37], located directly behind the LE chopper (downstream), is to concentrate the particle density by providing a localization of the ion bunch in space/time as sharp as possible. This is achieved by a (long) double-split drift tube where the pulsed beam (pulselength 100 ns) is bunched by two RF waves ("1F" at 5 MHz and "2F" at 10 MHz) to a burst duration of about 1 ns. The phase-shift ("Phase 2 F") is adjustable separately as well as their amplitude ratio (controlled by the absolute value "Amplitude" and their ratio "Balance"), but both amplitudes are also adjustable separately, "Ampl 1 F" and "Ampl 2 F". These quantities depend on the mass of the particles, their velocity, and on the length of the tube.

The superposition of the first harmonic frequency approximates a sawtooth function which would be optimal for a linear acceleration or slowing down of particles that are too late or too early, respectively, compared to the mean field-free flying particle. The focus of the bunch in the optimum case is at the high energy chopper (see below). The phase of the LE chopper / buncher ensemble may be shifted ("Phase") against that of the master frequency generator.

Tandem

In a carbon stripper foil (4.0 μg/cm^2) in the high voltage terminal, the B^- beam is converted to B^{5+} ions. We have chosen the completely stripped ion's charge state because the extraction yield is higher (59%) as compared to B4+ (26%) and the terminal voltage (11.2 MeV) can be controlled at a lower value compared to 13.4 MeV in the case of B4+, this facilitates a stable operation of the accelerator. Ion currents are measured by Faraday cups located at relevant positions in the beamline. Cup 1 is located directly in front of the tandem tank (see Figure 6.1) where typically 400 nA (DC) are measured. The final energy of the B-ions is controlled at 67 MeV: this is the sum of the net mean energy of the boron nuclei in the lab system at the production resonance of 61 MeV (Figure 6.2), plus an energy loss of 5.1 MeV in the cell window, plus a mean energy loss of 1.3 MeV in the H_2 gas (Subsection 6.1.3). The beam is then analyzed by a 90° magnet to select those ions that were correctly charged in the stripper foil, yielding about 600 nA (DC) or 75 nA pulsed beam ($i = 1$). Compared to the value measured on Cup 1, the *charge current* is enhanced by a factor given by the new charge state of the ion (5+). Furthermore, a particle transmission of about 50% is observed. This current is measured at Cup 5 which is located directly behind the 90° magnet. The ^{11}B nuclei are now travelling with 23.6 mm/ns (0.112c).

High-energy chopper

To cut the front and end tails of the bunch a high energy (*HE*) chopper ("Rudolf-" or alternatively "Posselt-chopper") is operated by an oscillator at the same frequency which is used at the CERN laboratory (10.051 MHz). Logarithmic current differences on two segments of a current integrating slit-aperture located downstream behind the HE chopper are used to control the bunch position with respect to the LE system via "Phase".

After having passed various ion lenses (quadrupole solenoids) and steerers (electrostatic capacitors), the pick-up of the high-energy chopper (most of

the time the Rudolf-chopper) and 2 switchers (tandem-hall to hall I and from there to hall II, Figure 6.1) a B^{5+} beam with typically 40 nA (DC, no pulsing) arrived at the experiment. Depending on the variable pulsing frequency settings the flux is further reduced. The highest repetition rate of the ion bunches is 2.5 MHz.

Three dominant effects are responsible for broadening of the bunch (assumed optimal pulsing adjustment):

(a) Energy uncertainty during extraction ($\Delta\tau_1 = 0.25...1$ ns)

(b) Inhomogeneities in the gap field of the buncher ($\Delta\tau_2 = 0.3...1$ ns)

(c) Smearing of energy during the stripper passage ($\Delta\tau_3 = 0.7...1$ ns)

Therefore the total time resolution originating from the bunch width amounts to $\sqrt{\sum \tau_i^2} = 1...2$ ns, which is about 1/3 of the overall experimental time resolution (cf. Figure 6.6).

6.1.3 The hydrogen gas target

At the experimental site, neutrons are produced by the reaction $p(^{11}B,n)^{11}C$. For this purpose a hydrogen target has to be supplied by a hydrogenated foil (usually containing carbon) or a hydrogen gas target. In order to suppress the neutron background from a carbon-boron reaction, a hydrogen cell was chosen and designed as follows: The hydrogen gas is contained in a cylindrical stainless-steel cell with walls of 0.5 mm, a length of 3 cm and an inner diameter of 1 cm (Figure 6.4). For the entrance window a material had to be found which has high mechanical strength and is leakproof under ion bombardment. In Ref. [49], $^{96}_{42}$Mo foils are reported to not showing any signs of failure at deuteron beam intensities up to 20 μA. Consequently, molybdenum was chosen for the window foils. The choice of the window foil thickness is a compromise between long-term safe operation (beam bombardment under given pressure difference) and minimum beam deceleration which otherwise would lead to an additional spread in neutron energy. Therefore the Mo foil thickness was chosen to be 5 μm. The calculation of the energy loss of the B-beam in the window is simplified because the effective charge fraction $\zeta = 0.95$ does not change during transmission, see Eq. (4.2). From Equations (4.5) and (4.10) we derive an average energy loss of 4.8 MeV for 64 MeV ^{11}B ions (corresponding to 15.3 times the Bohr velocity v_0, Subsection 4.1.1). The molybdenum foil was fastened to a small stainless-steel flange using a 2-component glue; the window flange together with a small

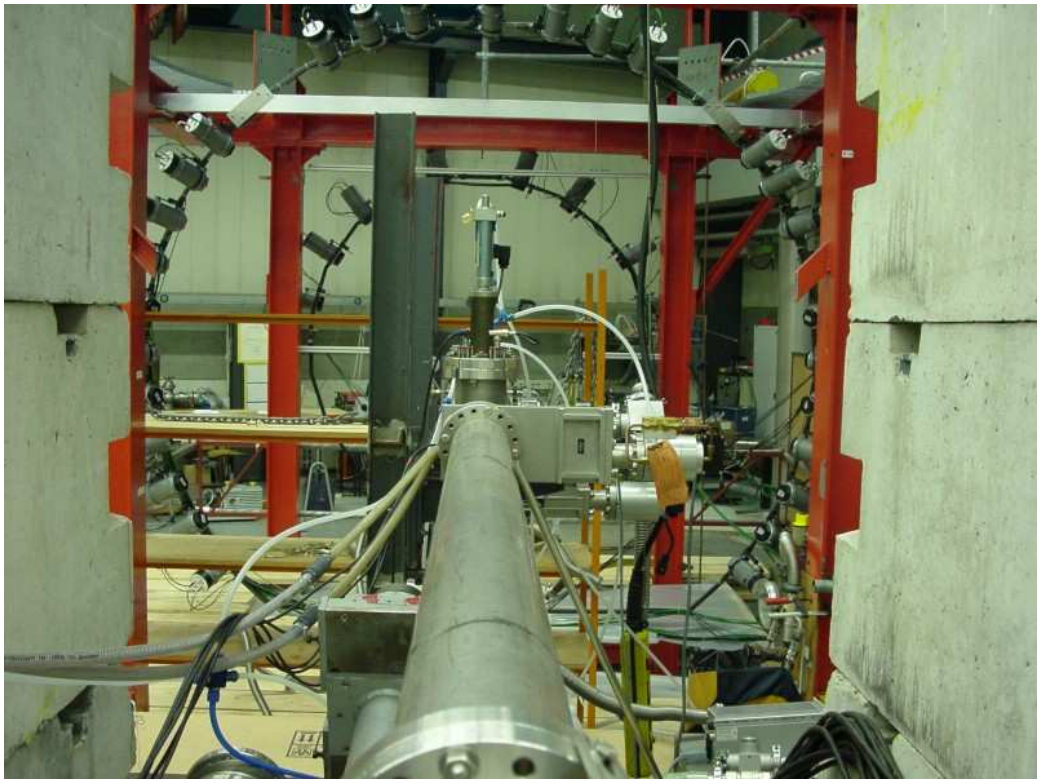

Figure 6.3: View downstream the beamline onto the experimental site. In this setup, two detector rings at different scattering angles and distances from the beam target are mounted.

isolating polyethylene disk and the aperture are screwed to the beam flange. The screws, connecting the flange to the beam tube reference ground, are insulated against the aperture.

The material of the beam stop has to be selected such that a neutron background from nuclear reactions of the beamstop itself is suppressed as much as possible. Therefore, the Coulomb barrier

$$V_C = \frac{Z_1 Z_2 e^2}{R} \tag{6.3}$$

with R being the sum of the two nuclear radii, cf. Eq. (3.1), is chosen to be as high as possible (Z_1,Z_2 are the atomic numbers). On the other hand high numbers for Z_2 and the mass number A_2 of atoms in the beam stop increase the kinetic energy available in the CM system. Selecting $^{197}_{79}$Au as beam stop material, which was reported to produce the smallest number of background neutrons among several tested stopper materials (C,Al,Fe,Ta,Au,Pb) [49],

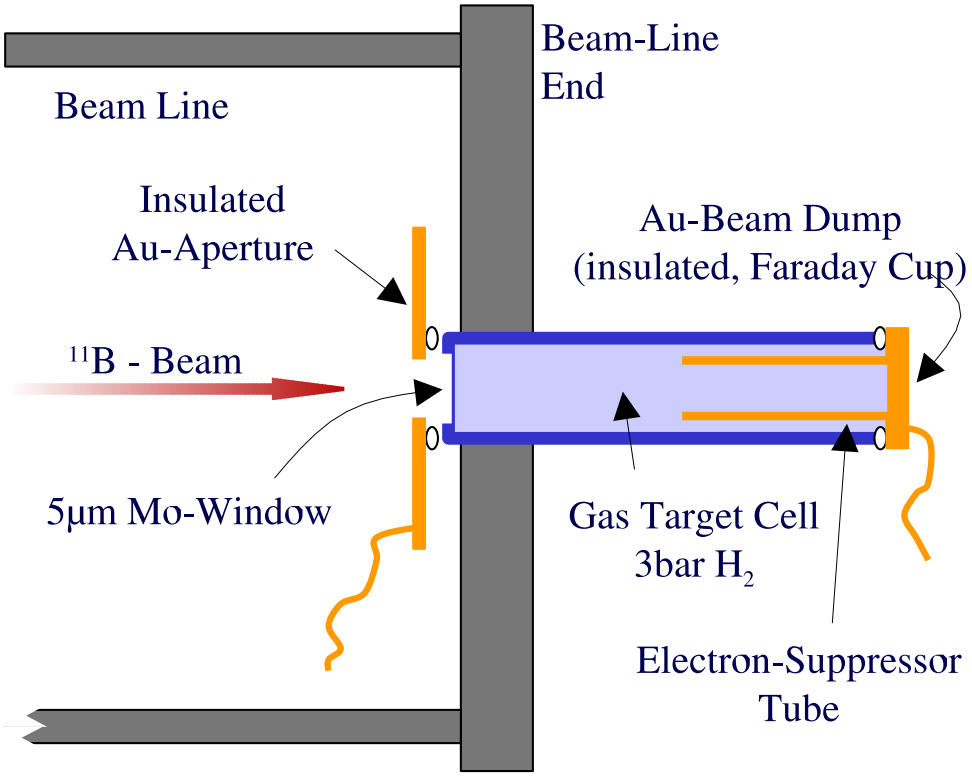

Figure 6.4: The hydrogen gas target cell: scheme

gives $V_C = 54$ MeV with $R = 10.5$ fm and a total CMS energy $\sqrt{s} = 58$ MeV (Eq. A.10) which is slightly higher. At the same time, the Mo window with $R = 8.8$ fm, $V_C = 33$ MeV and $\sqrt{s} = 57$ MeV contributes to a noticeable neutron background continuum at lower energies (see below) as well. The fraction of background to monoenergetic neutrons is about 1/3 and is well identified by blank runs (bombardment of the evacuated target cell). Nevertheless, such a blank run in a scattering experiment at the expense of actual beamtime is mostly less efficient.

In our experiment the beam stop is a 1.5 mm thick electrically insulated removable Au disk. An inner copper tube prevents backscattered electrons from leaving the beamstop. Otherwise such electrons would increase the measured integrated current picked up from the target leading to wrong estimates of the beam intensity. The entrance window is surrounded by an electrically insulated Au aperture in order to minimize the background neutron production by the beam corona and to serve as charge indicator during the adjustment of the beam optics. This assembly served as a Faraday cup for easier threading the beam onto the target and reading the beam

current during the experiment.

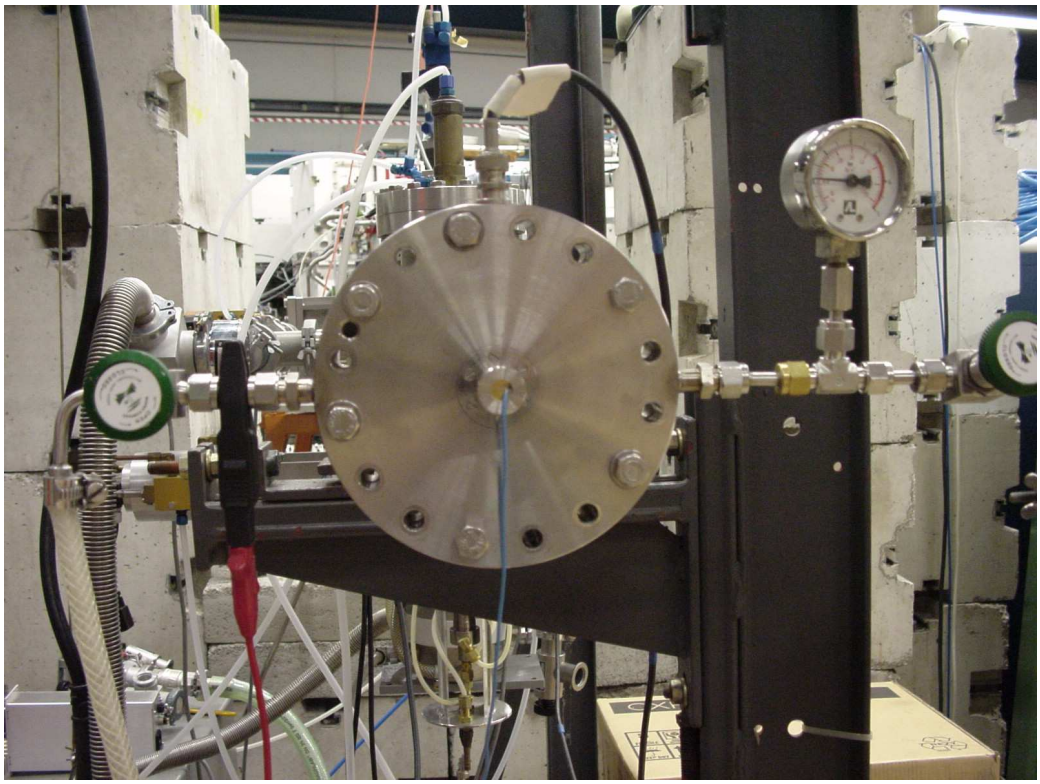

Figure 6.5: Photograph of the hydrogen gas target cell mounted on the end flange of the accelerator beam tube. The hydrogen gas transfer line with pressure gauge can also be seen.

The pressure of H_2 gas is 0.3 MPa absolute. The gas transfer line (Figure 6.5) is flushed thoroughly before filling the target to remove the residual gases. After the cell is irradiated for several hours, it is refilled with H_2 gas to remove the contamination stemming from the inner surface of the cell. The cell including the beam stop is exchanged regularly (typically once a day) in order to reduce the gamma radiation exposure of the central detector arising from the activated assembly. The Mo window was replaced at every beamtime, because gold atoms from the beam stop are sputtered onto the window leading to a broadening of the boron and neutron energy distribution.

A typical ToF spectrum is shown in Figure 6.6, the corresponding energy spectrum is depicted in Figure 6.7. The total energy resolution $\Delta E \approx 1.1$ MeV at 11 MeV (FWHM) derived from the ToF spectrum (Figure 6.6) originates mainly from four contributions:

(a) TDC time resolution (Subsection 6.4.2): 3 ns

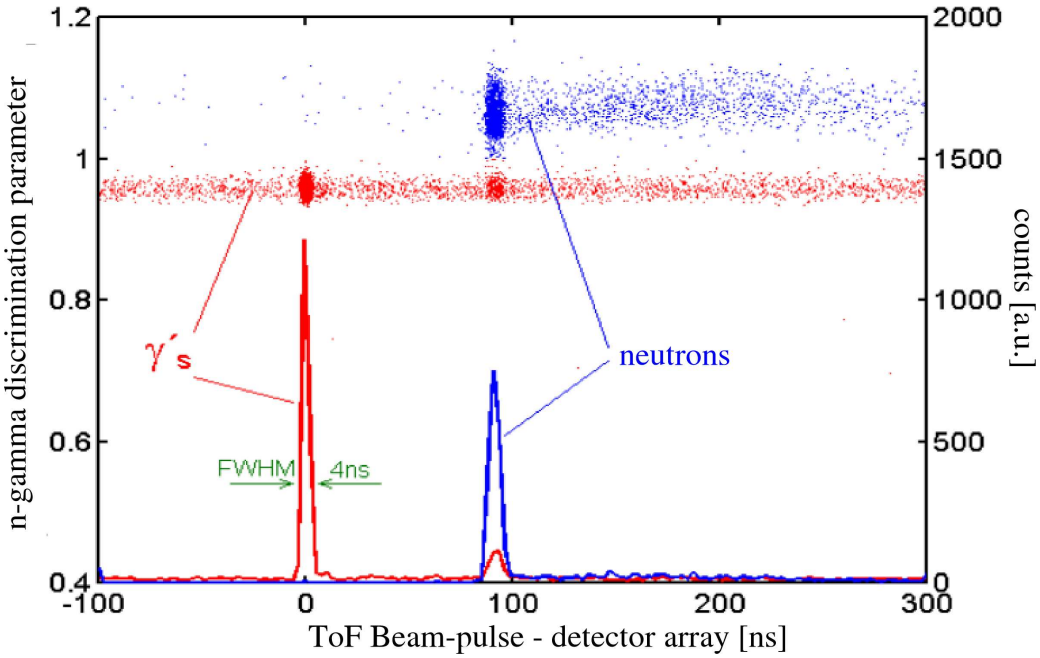

Figure 6.6: n/γ discrimination capability versus Time-of-Flight of the monoenergetic 11 MeV reaction. In addition, the ToF spectrum is shown (right axis).A sharp peak of neutrons that arrive about 100 ns later than photons from the gas target is clearly identified. These photons stem from inelastic reactions and the stopping of the boron beam in the target window and the beam stop. The discrimination of neutrons and photons is efficient both in ToF and pulse-shape. Events with gamma-like pulse-shapes, but occuring within the ToF-peak of neutrons, are induced by inelastic reactions of neutrons with carbon nuclei in the scintillator, where the carbon recoil is negligibly small [16] but a part of the photon energy is detected (see text). The tail of neutrons arriving later than the 11 MeV neutrons from the hydrogen reaction, obvious in the upper discrimination plot, stems from the beam stop and the target window, cf. Figure 6.7.

(b) ^{11}B-bunch resolution (Subsection 6.1.2): 2ns

(c) Reaction location within the hydrogen target: 1.5 ns

(d) Detection location within the neutron detectors: 1.5 ns

According to Eq. (6.8) (see Section 6.3), with $\Delta E = -2E\Delta t/t$, better energy resolution is achieved by longer flight paths (larger t). The resolution of the gamma ToF peak is just determined by items a) and b). Since these are the

two biggest contributions, the neutron ToF resolution is nearly as good as that of the gamma ToF peak.

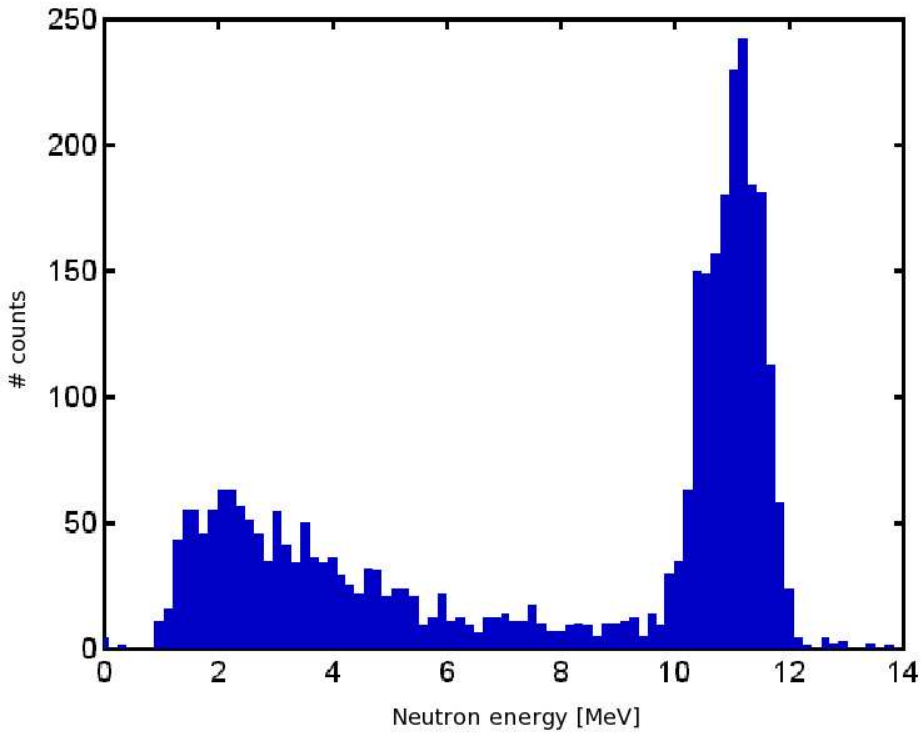

Figure 6.7: Energy spectrum of the monoenergetic 11 MeV reaction plus low energy background from the beam stop.

Neutron flux

The differential cross section for 11 MeV neutrons interacting in the neutron detector, i.e. in the liquid scintillator NE213, is $\mathrm{d}\sigma/\mathrm{d}\Omega\,(0°) = 180$ mb/sr [5] (see also Figure 6.8). For a characterization of the beam we usually take "Untersetzung" 1, i.e. a flux reduction after the buncher of $2^{i+2} = 8$ with respect to the measured dc current (gas-out) at the beamstop, resulting in a pulsed current of 1 nA. With the common charge state of +5 the boron current is $\dot{N}_B = 1 \cdot 10^9$ s^{-1}. One neutron detector, with a front area of $F = 64$ cm^2 at a distance of $R = 2$ m and an angle of 0° with respect to the boron flux direction, gives a solid angle coverage of $\Delta\Omega = F/R^2 = 1.6 \cdot 10^{-3}$ sr. The number of hydrogen atoms in the gas target (length L) which act as target for the boron beam is approximately $N_H/A = 2pL/k_BT = 4.4 \cdot 10^{24}$

m^{-2}. Considering a detection efficiency of 0.2 and using Equation (1.2) with $a = H$ and $b = B$, we derive a detection rate of $\dot{N} = 30/s$ for 11 MeV neutrons, which is in reasonable agreement with the measurement, taking into account the uncertainty of the measurement of the boron current due to backscattered electrons enhancing the positive charge of the beamstop.

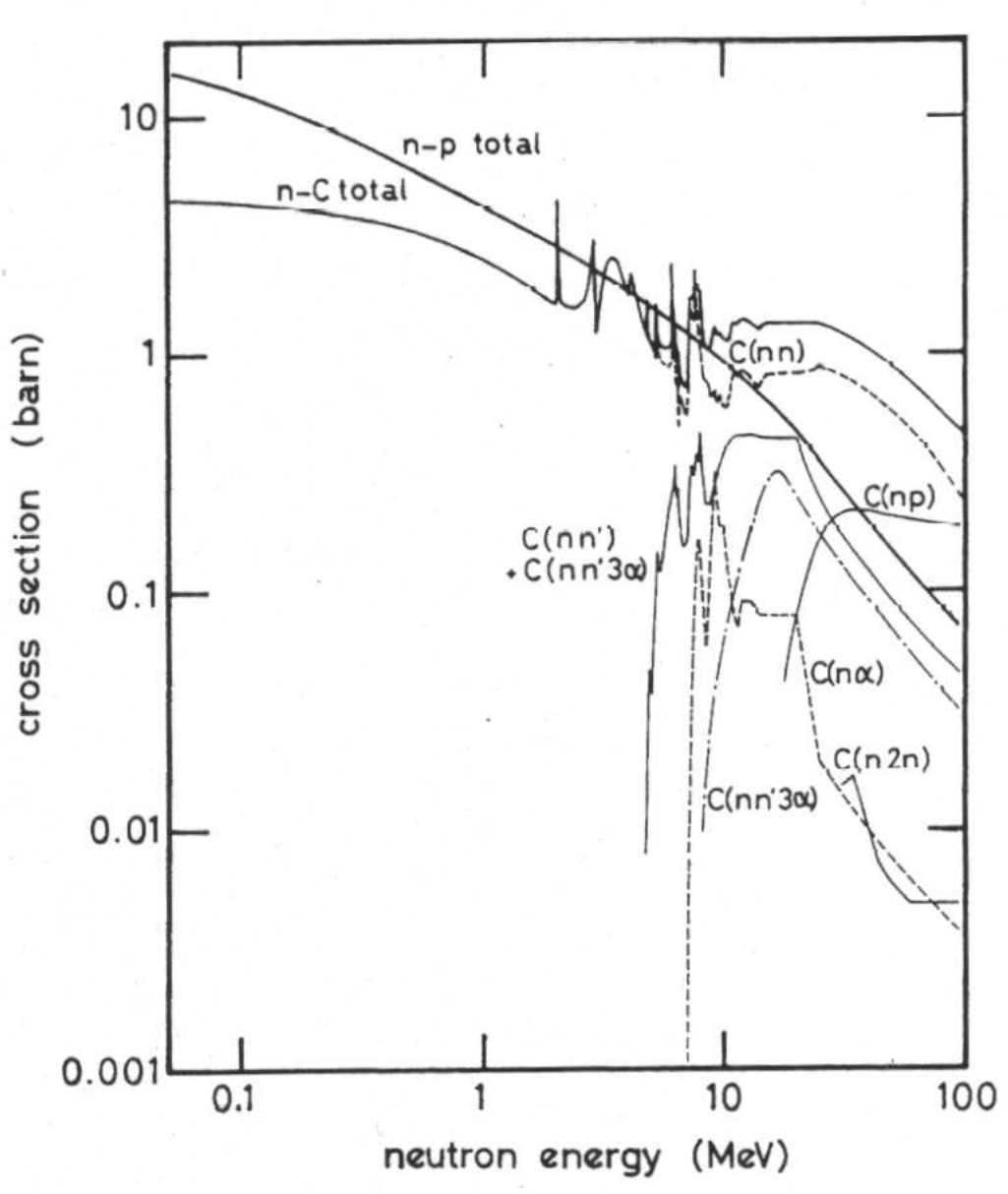

Figure 6.8: General features of various neutron-hydrogen and neutron-carbon reaction cross sections [47].

The strong reduction in current due to pulsing leads to power dissipation of only 10 mW. Therefore no target cooling system must be provided in contrast to similar experiments with higher currents.

6.2 Neutron detectors

Every neutron source emits gamma-rays as well (for example cf. Figure 7.2 in the case of the Am/Be-source). Thus the capability of discriminating neutrons from gammas which otherwise would contribute significantly to the background is essential.

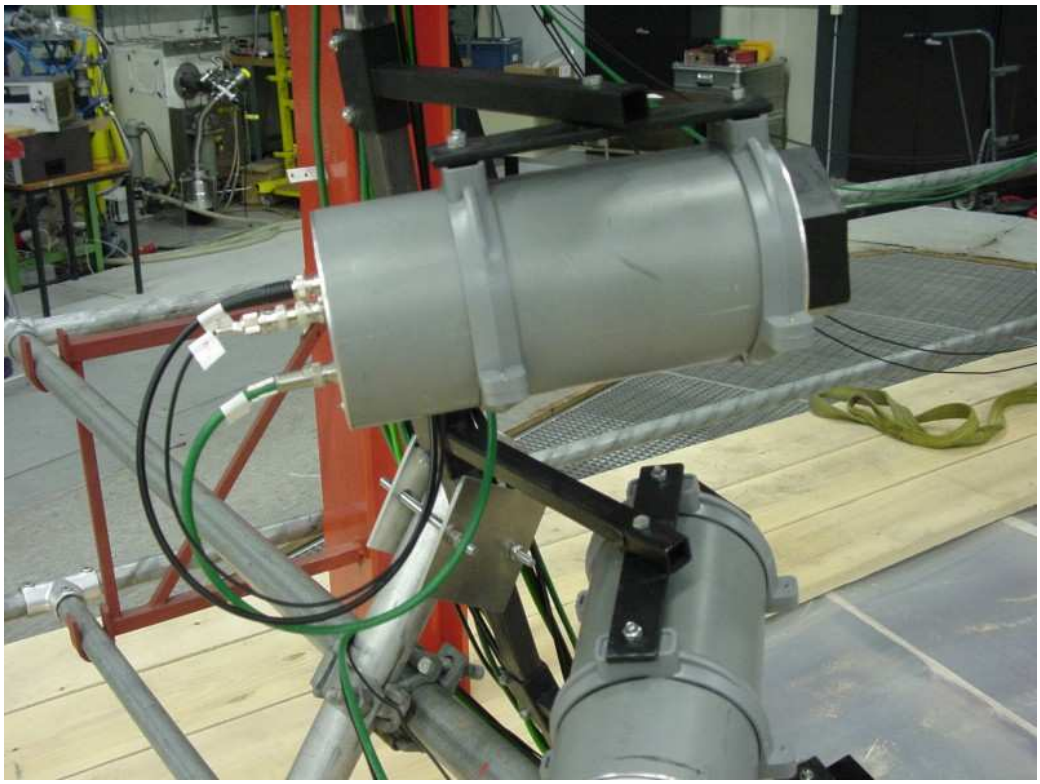

Figure 6.9: A photograph of the neutron detectors.

The most common method of fast neutron detection is based on elastic scattering of neutrons by light nuclei. As discussed in detail in Section 2.7, the scattering interaction transfers some portion of the neutron kinetic energy to the target nucleus, resulting in a recoil nucleus. The use of hydrogen as target is by far the most popular because according to Eq. (A.35) the energy transfer is maximum: only in collisions with ordinary hydrogen can

the neutron transfer all its energy in a single encounter. For single scattering in hydrogen, the fraction of the incoming neutron energy that is transferred to the recoil proton can range anywhere between zero and the full neutron energy, so that on average, the recoil proton acquires about half that of the original neutron energy (Figure 2.4).

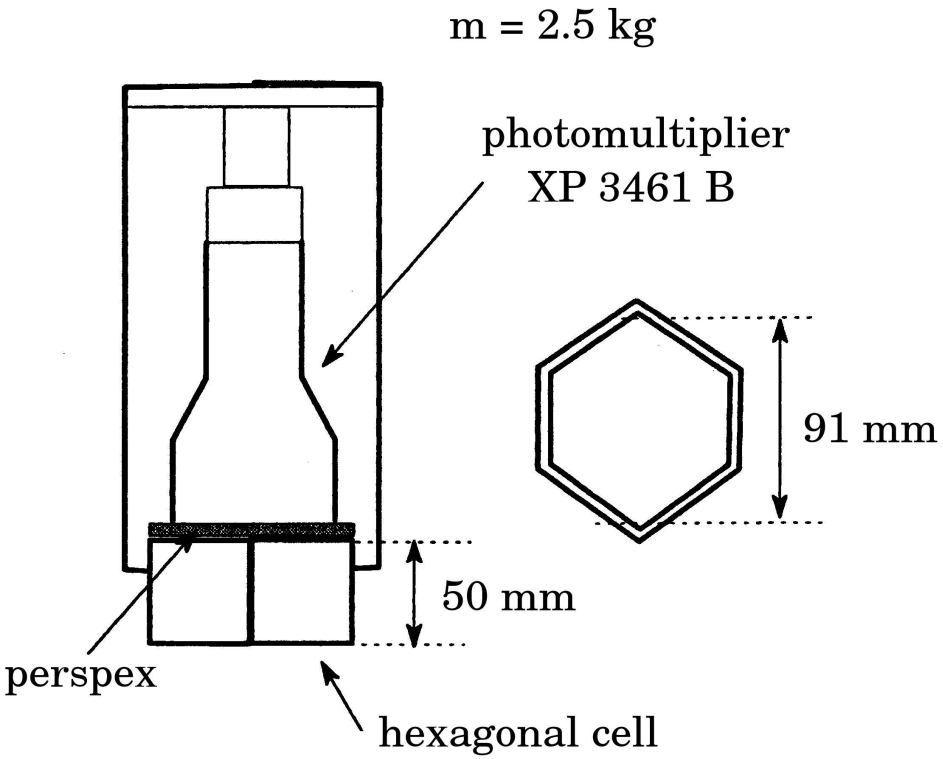

Figure 6.10: Scheme of the neutron detectors.

The SICANE team [39] from Lyon, France, generously equipped us with 40 neutron detectors; Figure 6.9 shows a photograph of such a detector, Figure 6.10 shows the schematic view [40]. Each cell which contains the liquid scintillator has hexagonal shape with an inner diameter of 91 mm and a depth of 50 mm. Each cell is optically coupled to a Philips photomultiplier XP 3461 B. The whole assembly (cell + photomultiplier) weighs 2.5 kg.

The manufacturer *Nuclear Enterprises, Ltd.* (NE) composed a liquid organic scintillator specifically for the purpose of good neutron/gamma-discrimination capability. Its identification number is NE 213. It consists of the originally crystalline organic scintillator naphtalene ($C_{10}H_8$, $\lambda_P \sim 340$

nm, t_0 = 81 ns, relative efficiency 3 % of anthracene [4]) dissolved in xylene ($C_{24}H_{30}$). This mixture is used to dissolve the primary solute PPO ($C_{15}H_{11}NO$ p-terphenyl). As already outlined in Subsection 5.4.1, the emission spectrum of any solution is characteristic of the solute and not of the solvent. The solvent used exhibits negligible fluorescence in the pure bulk state. The deposition of energy leads to the excitation of the solvent which transfers its excitation energy to the solute. The latter converts it into radiative energy emitting a continuous spectrum with a maximum at 380 nm [26]. A secondary solute (POPOP) is added to the mixture in order to shift the maximum of emission towards 420 nm to better match the photomultiplier cathode sensitivity. Structure formulas of the ingredients are displayed in Figure 6.11, Table 6.1 summarizes the basic properties of NE 213.

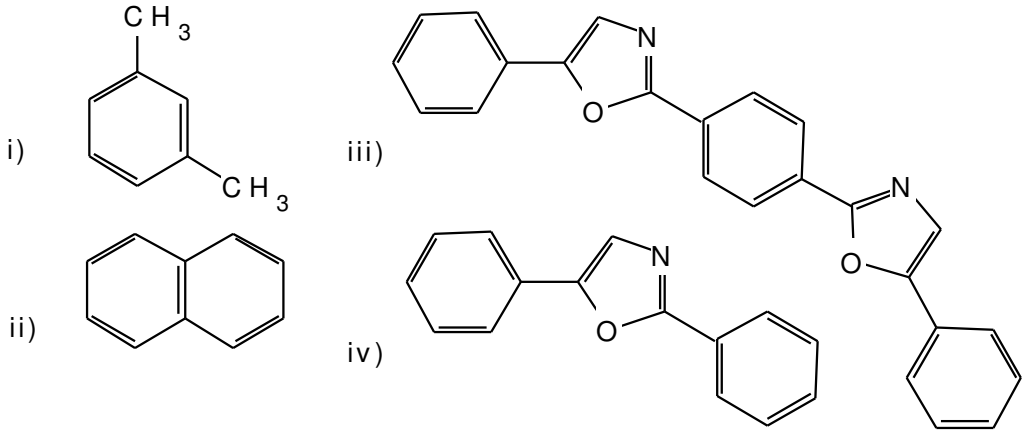

Figure 6.11: Structure formulas of ingredients in NE 213:
i) (meta-)Xylene ((1,3-)Dimethylbenzene), ii) Naphtalene,iii) POPOP, iv) PPO (2,5-Diphenyloxazole)

6.2.1 Calibration

The low Z value of the constituents of organic scintillators (hydrogen, carbon, and some oxygen) results in a very low photoelectric cross section, so that virtually all gamma-ray interactions are Compton scatters. Therefore a gamma-ray spectrum taken with an organic scintillator will show no photopeaks, and Compton edges are the only distinguishable feature. Since the scintillation response to electrons is fairly linear [20], a gamma-ray source is often used to calibrate the energy scale of the detector output. However, because there are no photopeaks, some point on the Compton edge must

Light Output	78% of anthracene
Wavelength of Maximum Emission	425 nm
Density	0.874 g/cm^3
H/C Atomic Ratio	1.213
Refractive Index	1.508
Boiling Point	141°C

Table 6.1: Properties of the liquid scintillator NE 213 [20]. Anthracene has the largest light output of any organic scintillator.

be selected and associated with the maximum energy of a Compton recoil electron. Following Flynn [20] we choose the channel number at which the Compton continuum has fallen to half its plateau value (see Figure 6.12).

6.2.2 Neutron-/Gamma-Discrimination

The rise time of the light response of the scintillator is comparable to that of the photomultiplier, some 100 picoseconds. The decay time comprises two components, cf. Section (5.4): one fast component (some nanoseconds) and one slow component (some hundreds of nanoseconds) [34]. Thus the shape of the light signal is given by

$$L(t) = A\exp(-\frac{t}{t_1}) + B\exp(-\frac{t}{t_2}) \tag{6.4}$$

The values of t_1 and t_2 as well as A and B vary as a function of the ionisation: whether caused by an electron (gamma detection) or a proton (neutron detection). Table 6.3 lists the values of these parameters.

The possibility to discriminate different particle interactions by their individual pulse shapes was already discussed in Section 5.4. Since the ratio A/B depends on the type of interaction, such a discrimination using the given CAMAC modules (Subsection 6.4.2) is realized by integrating each signal over two periods (cf. Figure 5.4) where either the fast or the slow pulse component dominates respectively: the first gate (called P1) collects fluorescence light with a typical gate length of 40 ns, the second gate (P2) integrates the full signal by additionally respecting delayed fluorescence by using a typical gate length of 400 ns. The electronic CAMAC modules are described in Subsection 6.4.2.

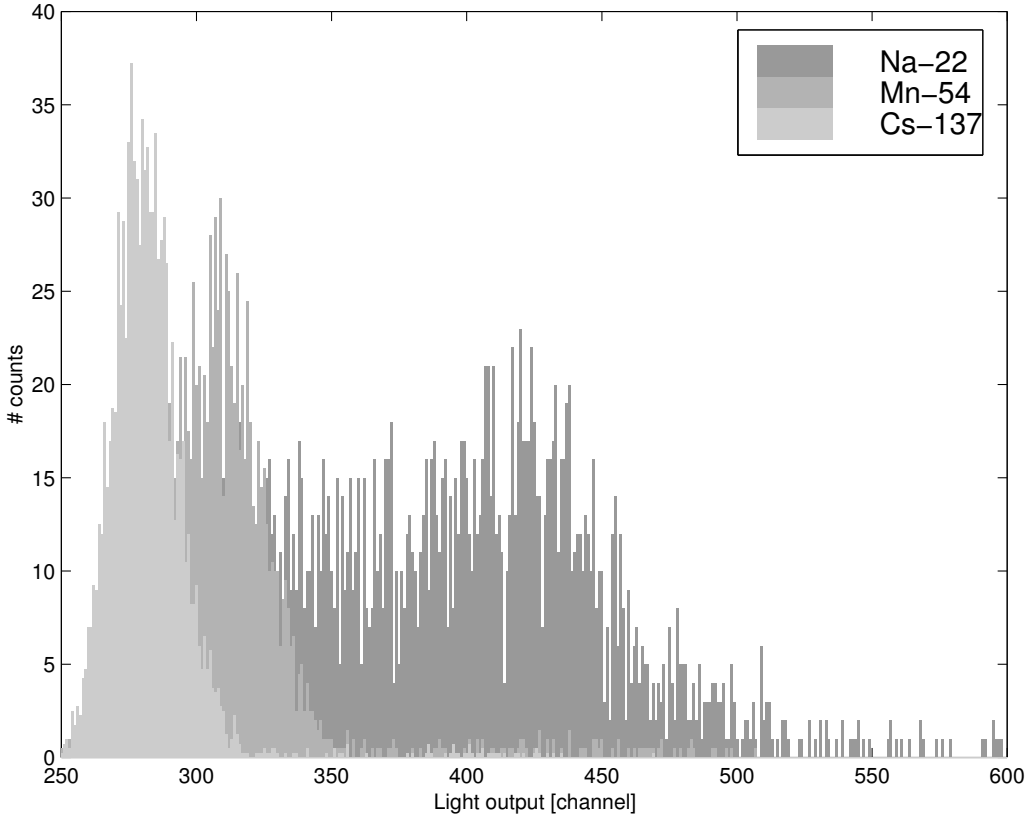

Figure 6.12: Linearity investigation of the neutron detectors: calibration via Compton spectra. Energies of the sources are listed in Table 6.2. The low-energy part of the spectra is cut due to the trigger threshold, the rate enhancement towards the edge is predicted by the Klein-Nishina-formula [20].

6.2.3 Detection efficiency

The neutron detection efficiency of the liquid scintillator is calculated via the neutron mean free path length λ which depends on the interaction cross section of the nuclei that constitute the solvent: carbon and hydrogen. It can be expressed as:

$$\frac{1}{\lambda} = \sigma_{\mathrm{H}} N_{\mathrm{H}} + \sigma_{\mathrm{C}} N_{\mathrm{C}} \tag{6.5}$$

where N_{H} and N_{C} are the numbers of hydrogen and carbon atoms per unit volume: $N_{\mathrm{H}} = 4.82 \cdot 10^{22}$ cm^{-3} and $N_{\mathrm{C}} = 3.98 \cdot 10^{22}$ cm^{-3}, cf. Table 6.1.

The total reaction cross section of NE 213 for an incident neutron of 11 MeV is about 1 barn (10^{-28}m^2) for hydrogen as well as for carbon (see Figure 6.8), resulting in a mean free path of $\lambda = 12.5$ cm. Nevertheless it must be

Source	Decay	$T_{1/2}$	Energy [keV]	Branching ratio [%]	Compton edge [keV]
Am-241	α	432 y	60	36	11
Co-57	EC	272 d	122	86	39
			136	11	47
Hg-203	β^-	47 d	279	81	146
Na-22	Annihilation	2.60 y	511	90	341
Cs-137	β^-	30 y	662	85	478
Mn-54	EC	313 d	835	100	639
Na-22	β^+ / EC	2.60 y	1275	100	1062
Co-60	β^-	5.27 y	1117	100	963
			1333	100	1118
C-12*	γ		4439	100?	4197

Table 6.2: Gamma sources used for the calibration of all detectors involved in our setup. Listed are: Mode of decay leaving an excited daughter isotope with subsequent gamma de-excitation, half-life, energy of photopeak [17], yield per disintegration ("branching ratio") and Compton edge derived according to Equation (A.38). C-12* denotes the first nuclear level of carbon-12 excited by an (α,n)-reaction of Be-9 (details in Section 7.1).

	t_1 [ns]	t_2 [ns]	A/B
Electron	5.2	107	38
Proton	5.6	138	28.5

Table 6.3: Pulseshape parameters according to Equation (6.4) for scintillation light emission in NE 213 [43].

emphasized that the restriction to proton recoils via pulse-shape analysis reduces the *detection* efficiency by a factor of two compared to the overall

reaction cross section. Furthermore by comparing λ with the dimensions of the neutron detectors (Figure 6.10) we notice that these detectors have been designed for a lower neutron energy (the AMPHORA experiment [43]). There the mean neutron energy was $\sim$ 1.3...2.1 MeV, accordingly the total reaction and detection cross sections are higher (Figure 6.8, $\lambda \approx 6.0$ barn). Therefore a scintillator depth of 5 cm was chosen for a mean free path of $d = 3.7$ cm, resulting in an interaction probability $(1 - e^{-d/\lambda}) = 74\%$. For the 11 MeV neutrons we chose to deploy the neutron detectors perpendicular to their symmetry axis, so that the scattered neutrons face the 5 cm wide edge of the scintillator: while the total reaction efficiency of 52 % does not change since it depends on the total reaction volume for $d \ll \lambda$. Of course, besides a high detection efficiency for the neutrons that are scattered from the central detector, a good resolution of the scattering angle is desirable in order to pin down kinematics. By choosing the perpendicular orientation, the resolution of the scattering angle is enhanced by a factor of 2. (Note: since detection efficiencies depend on the detector threshold (continuum spectrum, see Figure 2.4) the efficiencies quoted in this paragraph are calculated for a 0 keV threshold.)

6.2.4 Quenching

As for any other scintillator, the intensity dL of light produced for an energy deposition dE strongly depends on the nature of the ionizing particle (Section 2.3). If the particle is an electron, the amount of the collected light is proportional to the energy deposition (Subsection 6.2.1). However, for proton recoils induced by incident neutrons, the relation light/energy is non-linear and can empirically be parametrized as [40]:

$$E_{ee} = 0.215E_p + 0.028E_p^2. \tag{6.6}$$

For example, an 11 MeV neutron, transferring at maximum all its energy to a proton, yields about half of its kinetic energy in equivalent electron energy: $E_{ee} = 5.75$ MeV for the maximum recoil energy; but as already mentioned, the energy deposition is continuous (see Figure 2.4). Of course, gain and gate width (esp. P_2) must be adjusted to account for the maximum light yield. Thus the continuous energy deposition does not allow for neutron identification that would be possible if a characteristic neutron energy was fully absorbed. Instead, pulse shape analysis and time-of-flight measurements must be used.

6.3 Geometry

For a given scattering angle ϑ and a given neutron detector distance R from the centre of interaction which is located at z_0, the optimal spatial distribution of the neutron detectors can be derived from the intersection of a sphere (radius R, centre z_0) and a cone (opening angle ϑ, peak at z_0). In this case, all detectors are located at the same distance from the central detectors and under the same scattering angle, therewith averaging of energy dependences in cross sections and Quenching factors are minimized. In a scattering experiment, there are several constraints that influence the optimum geometrical setup:

Scattering angle: Due to the axial geometry the differential solid angle $\mathrm{d}\Omega$ is proportional to the sine of the scattering angle ϑ:

$$\mathrm{d}\Omega = 2\pi \sin\vartheta \mathrm{d}\vartheta. \tag{6.7}$$

In practice, the area (i.e. the number of detectors) usable to observe scattered neutrons is maximal at 90° and it is hard to put many detectors close to 0° or 180°.

Rate vs. resolution: In time-of-flight (ToF) spectrometry the relative energy resolution is inversely proportional to the flight path R (classical calculation) [29]:

$$\frac{\Delta E_k}{E_k} = 2v \cdot \frac{\Delta t}{R} \tag{6.8}$$

Here E_k is the kinetic energy of the neutron, v is its velocity, and Δt is the overall time resolution. Thus a longer flight path leads to a better energy resolution. On the other hand the rate of neutrons $\dot{n}$, scattered into a detector area of a fixed size, is inversely proportional to the square of the distance: $\dot{n} \sim R^{-2}$. Usually a compromise is necessary between an optimal counting rate and a reasonable energy resolution.

6.4 Data acquisition

The data acquisition (*DAQ*) of the 40 neutron detectors is arranged in 5 groups with 8 detectors each. This division is given by the organisation of the appropriate CAMAC modules (TDCs, QDCs and CFTs) that were generously provided by the Institut de Physique Nucléaire de Lyon (IPNL), as well as the neutron detectors themselves, and used for the neutron detector part of the hardware DAQ.

6.4.1 NIM

High voltage supplies for the central detectors (other than the neutron detectors), signal shaping, timing, coincidence logics, fanning, etc. for signals coming from the accelerator pulsing system, from the central detector(s) and from the neutron detectors are provided by six NIM (Nuclear Instrument Module) systems, each rack subdivided into 12 individual module positions.

6.4.2 CAMAC

The hardware DAQ interface between the detectors (or the NIM hardware, resp.) and the software DAQ is provided by two CAMAC (Computer Automated Measurement and Control) crates. One important feature of the CAMAC system is that a standard CAMAC word access needs 1 μs for read/write which must be accounted for in the interplay of software and hardware trigger engineering. The following passages describe the most important plug-in modules used in the experimental setup.

DFC

Fast amplitude independent trigger generation for high time resolutions is achieved by Constant Fraction Triggers (CFTs, Discriminateurs à Fraction Constante, DFCs). This time pick-off method is superior to simple leading edge timing because an output signal is produced a fixed time interval after the leading edge of the pulse has reached a constant fraction of the peak pulse amplitude [20]. This time interval is then independent of pulse amplitude for all pulses of constant shape.

Each of the 4-channel ISN (Institut des sciences nucléaires de Grenoble) modules used in this work accepts 50 Ω positive (+5 V maximum) signals at LEMO sockets as well as a common veto (NIM) and an authorisation ($\overline{\text{NIM}}$) signal [43]. Each channel provides two 50 Ω LEMO outputs: a prompt and a delayed ("Retardée", 270 ns) NIM gate of 250 ns length each which will be connected to the TDC inputs (see below). A 34-line ribbon cable (ECL) may be connected to the corresponding QDC input (see below) providing several combinations of programmable gates for each channel (especially P1 and P2, Subsection 6.2.2). A speciality of these modules is that the authorization (veto) inputs open (inhibit) only the ECL signals, the NIM signals are not controlled. The idea behind this arrangement is that fast coincidence analysis from their own generated trigger may be used to authorize (veto) the integration by the QDCs.

TDC

12 bit Time to Digital Converter modules (TDCs) [26] were used for the fast coincident neutron ToF measurement. They are stepwise adjustable for maximum time intervals between 100 ns and 5 μs with corresponding resolution. For our scattering experiment where we face neutron flight durations of about 100 ns it is convenient to choose 1 μs with a channel spacing of (about) 300 ps. The modules accept 50 Ω coaxial lemo inputs on the front panel: one single start, 8 individual stops, 1 common stop and one clear (*RAZ*, "Remise A Zéro"). All signals are NIM. A speciality of these modules is that the external RAZ resets the memory without arming, i.e. after such a hardware RAZ the memory is indeed reset to zero, but rewriting is still not enabled. Different TDCs differ considerably (up to 50 %) in time/channel calibration, requiring a check whether all TDCs are within their appropriate range when operated in common timing coincidence. The TDC response is perfectly linear (within their resolution given by quantization), but we recognized a drift on a time scale of seconds, leading to a poorer resolution of about 3 ns (Subsection 6.1.3).

QDC

The charge signal of the neutron detectors is digitized by a 16 channel multiplexed 12 bit ADC. The modules provide one ribbon jack with 34 connectors that accept the integration gates (ECL) from the DFCs. The charge pulses themselves are connected to either one of eight 50 Ω LEMO entries, furthermore a NIM 50 Ω LEMO RAZ jack is provided on the front panel. The allocation of ports to the signal inputs is CAMAC programmable, e.g. four signals can be integrated within four ports or eight signals within 2 ports, etc. A speciality of these modules is that the external RAZ does arm the module but leaves the previously stored data in the memory, i.e. no reset (clear) is performed.

6.4.3 LabView

The software DAQ and data storage is programmed in LabView, a high-level programming language with a graphical front-end resembling the design of electronic circuit boards. The programming of user-interfaces (Virtual Instruments, VIs) provides very intuitive handling, but the use of ready prepared program blocks with a multitude of options slows down the operation, often beyond the CAMAC timing.

6.5 $CaWO_4$ Scintillation detection

The endeavour after the Quenching measurement of Dark Matter relevant tungsten recoils requires an extremely careful design of the scattering experiment for the following reasons:

- tungsten (A = 180-186) is the heaviest element tested so far. Thence the signal is expected to be very small due to the low recoil energy and an expected low Quenching factor. To be nontheless sensitive requires:
  - a very low detection threshold (single photo-electron sensitivity is desirable at room temperature since recoil energies are very small, cf. Table 7.2),
  - the knowledge of contributions from inelastic nuclear processes at small level spacings,
  - the consideration of all kinds of accidental coincidences, growing in relevance at low energies
- the dominant light emission decay time τ of $CaWO_4$ is by far longer than the occurring flight- and detection times in the neutron detectors, with the need for:
  - higher accelerator repetition rates than $1/\tau$ to ensure a reasonable neutron flux. As a consequence, the coincidence decision between neutron and central detector has to be adapted to the delayed trigger response of the central detector
  - reliable control of trigger timing over more than two orders of magnitude in light yield.

6.5.1 Photomultiplier tubes

Photomultiplier tubes (PMs) are the most widely used devices at room temperature to convert the extremely weak light output of a scintillation pulse into a corresponding electrical signal. Their major drawback is the small escape depth of the photocathode resulting in semitransparency for incident (visible) light. The comparatively low quantum efficiency of maximum 20–30% not only leads to actually higher minimum achievable thresholds, but also contributes significantly to a deterioration of the energy resolution being the bottleneck in the number of information carriers throughout the whole conversion process.

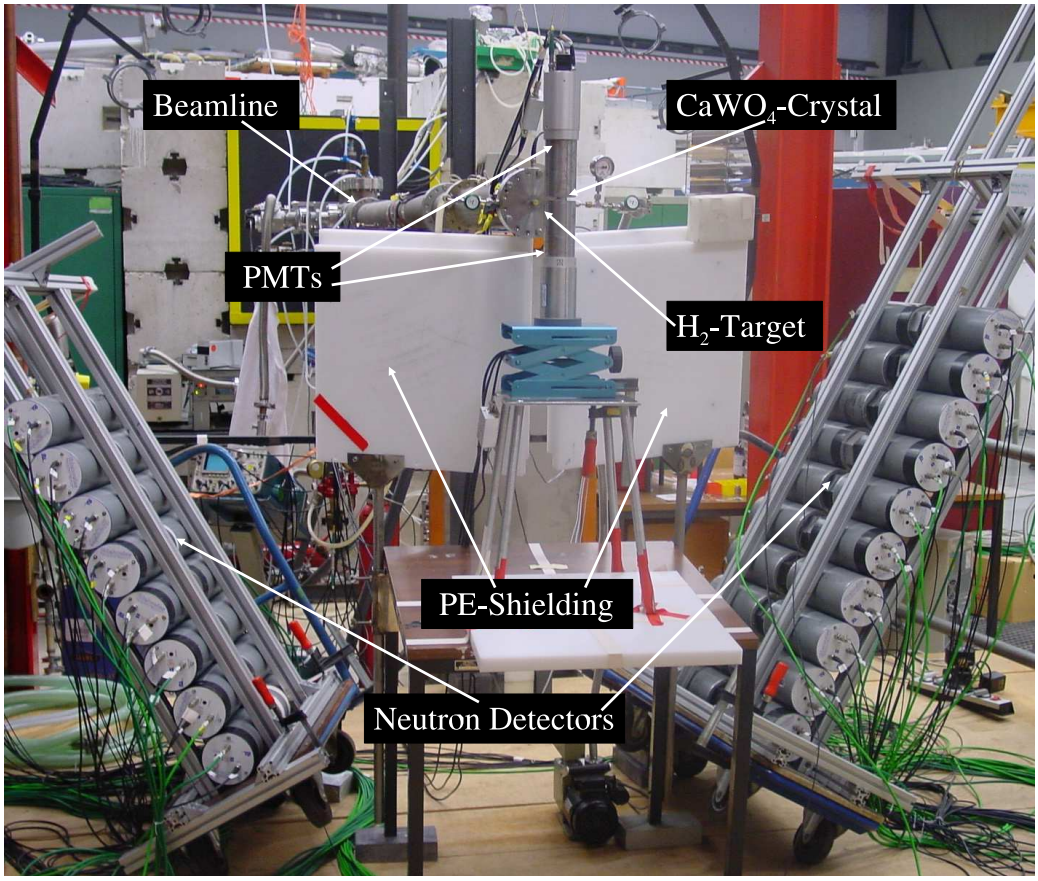

Figure 6.13: Photograph of the setup for neutron scattering by $CaWO_4$ using a double detector.

The sensitivity of the photocathode and the window glass should match the scintillation spectrum as closely as possible. While the work function (potenial barrier between material and vacuum) is to be kept as low as possible in order to collect a maximum number of electrons even in the long-wavelength region of the light spectrum, superior photosensitivity is only achieved at the price of higher thermionic noise. During the first beamtimes we have used two RCA 8850 photomultipliers. Since the thermal emission rate ($\sim 100/\mathrm{m}^2 \cdot$ s) is proportional to the cathode area, we later switched to smaller PMs with a window size adapted to the size of the $CaWO_4$ crystal. The reduction of the window volume is, in addition, advantageous for minimizing the event rate of unwanted neutron scatterings giving rise to wrong deflection angles and spurious pulses in the glass itself.

For a further reduction of low-energy background events (dark pulses and neutron interactions in the vicinity of the scintillating crystal) two photomul-

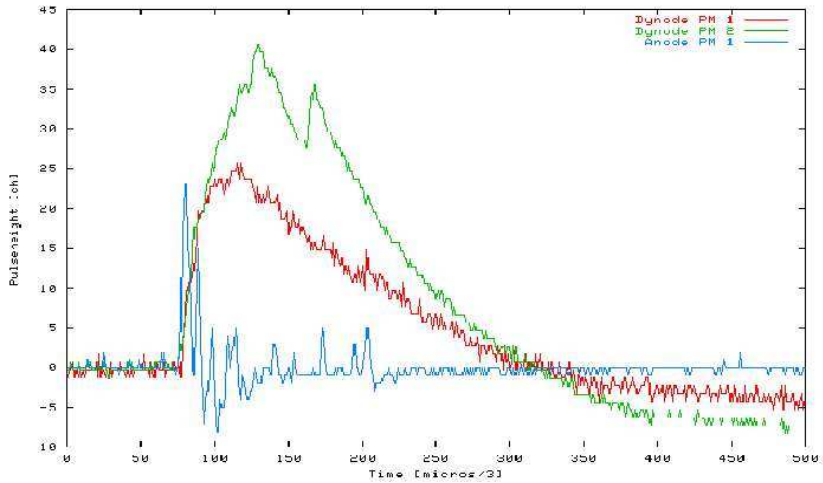

Figure 6.14: Scintillation light signals in the double detector: fast (anode) and slow (dynode) signal of photomultiplier 1 and slow (dynode) signal of photomultiplier 2. Single photo-electrons arrive according to the exponential light decay and give rise to spikes in the fast signal and steps in the integrated (dynode) signals.

tipliers were mounted facing the cylindrical $CaWO_4$ crystal on opposite sides and read out in coincidence with each other. Events that create a signal in only one PM may thus be rejected offline, i.e. in the subsequent software data analysis. Furthermore, the light collection from both crystal faces reduces the number of internal reflections and corresponding signal degradation due to absorption in the crystal and the reflective foil.

6.5.2 Light collection

The cylindrical crystal was surrounded by an aluminum foil or a multilayer reflective foil or a combination of both for enhanced light collection. In order to prevent total reflection by enclosed air bubbles between the plain faces of the crystal and the PM glass, which would lead to light trapping, the crystal was coupled to either PM by an optical compound; also various liquids were tested. The refractive index n_1 of the optical compound should be chosen intermediately between the refractive index n_1 of the PM glass and the high refractive index n_2 of $CaWO_4$: $n_0 < n_1 < n_2$. This coupling does not relieve the difference between n_2 and n_0 since the critical angle $\vartheta_c = \arcsin n_2/n_0$ is determined by the maximum and minimum refractive indices

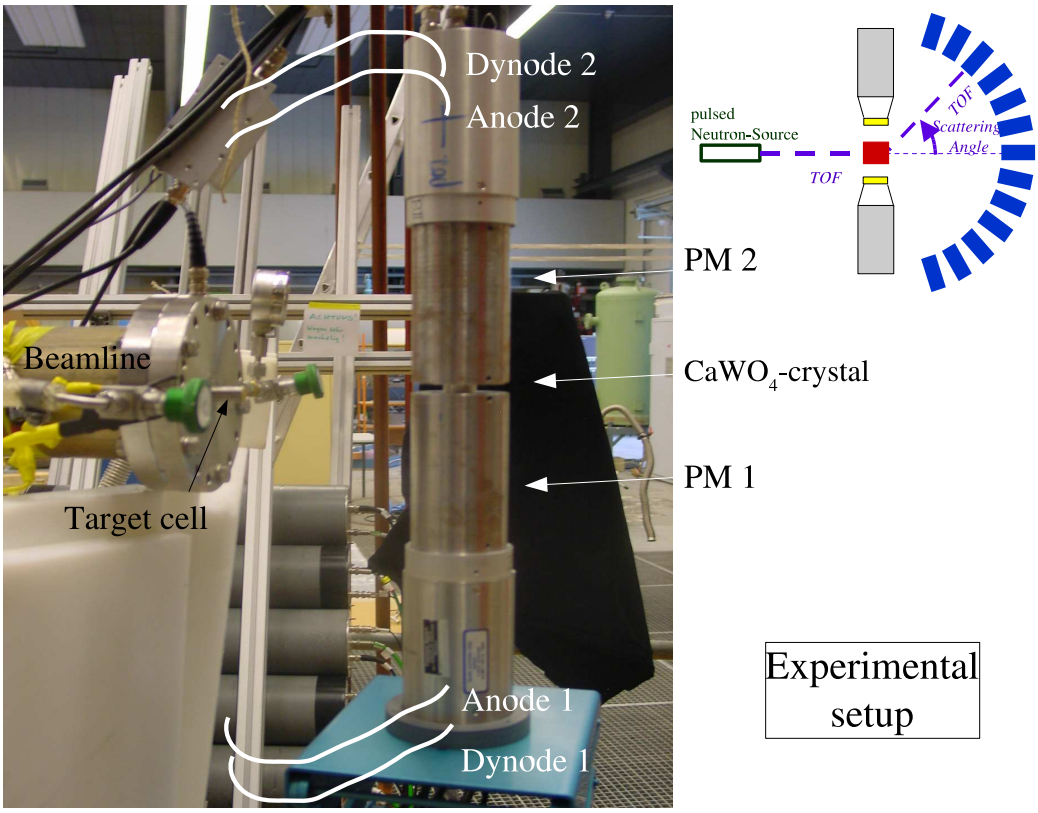

Figure 6.15: Neutron scattering by $CaWO_4$ using a double detector: anode and dynode signals from photomultipliers 1 and 2 facing the crystal from opposite sides. Below the target cell: $0.5 \times 0.5 \times 0.05$ m^3 polyethylene panels for shielding of the neutron detectors (bottom centre) against direct irradiation from the cell, keeping the shielding mass as low as possible to prevent ambient scattering.

from all surface transitions. Furthermore we tested whether crystal surface roughening enhances the light output (with or without optical coupling) from the plain faces. Summarizing we found that all of these methods lead to only small changes in the total light yield, at maximum on the 10%-level (which is already of the order of variations due to remounting of the PM–crystal setup), indicating a nearly maximum light collection efficiency.

6.5.3 Calibration and Trigger Generation

From both photomultipliers two signals were recorded: one fast (differentiated) signal, which shows the single photon electron (PE) pulses that arrive with the exponential decay of the $CaWO_4$ scintillation ($\tau \approx 12$ μs, see be-

low), and one slow (integrated) signal which integrates over the total light emission, giving a pulse with a risetime equal to the light emission time and a pulse height proportional to the total energy. For the RCA 8850 PMs, the fast signal was taken from the anode, the slow one from the dynode. For the PMs adapted in size, the singal integrated signal from the PM was split and one branch was electronically differentiated. So two signal traces from each PM were stored using a JOERGER waveform digitizer. A photograph of the setup is shown in Figure 6.15. Processing and recording both traces of each PM is advantageous for the following reasons:

Slow signal

- The properly shaped integrated signal provides the hardware DAQ trigger by using the cross-over method (details in Section 7.3). Single photo-electron sensitivity could be reached with the option to raise the detection threshold to a few PEs arriving on a several μs time scale.

- The integrated signal pulse height provides the energy information, especially in the higher energy range ($>$ 15 keV) where pile-up makes PE counting impractical or even impossible

Fast signal

- First photo-electron trigger (*FPET*) provides a much more accurate trigger timing offline than hardware cross-over trigger does. This holds because the quality in timing resolution of the cross-over method depends on congruent pulse shapes for different amplitudes, a situation which is only scarcely fulfilled at low energies where every incoming PE adds a step to the integrated signal (Figure 6.14).

- Counting of single PEs at low energies provides a more accurate energy information and resolution than the integrated signal due to the statistical arrival of single PEs. The merging of both calibration methods at intermediate energies was accomplished.

Calibration spectra and the linearity proof of the scintillation yield for electron recoils are shown in Figure 6.16.

6.5.4 Trigger timing

The hardware DAQ trigger system is divided into a fast and a slow component. The fast component is related to the duration of neutron flights

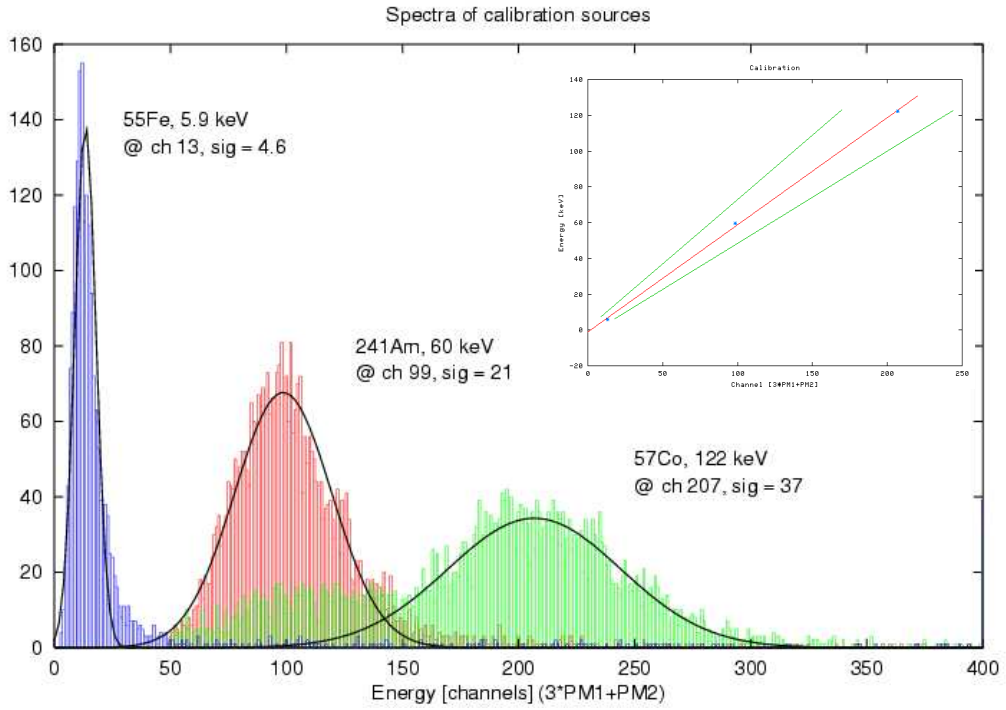

Figure 6.16: The $CaWO_4$ scintillator calibration: composed histogram generated from irradiation spectra of a ^{57}Co, ^{241}Am and a ^{55}Fe source. The energy information was taken from the pulse height of the dynode signal for all sources with optimal weighing of the contributions from the two photomultipliers PM1 and PM2. The inset shows the channel-energy relation to satisfy linearity over the energy range of interest down to 6 keV. The red (central) line is the best fit, green (outer) lines indicate the 1σ energy resolution.

between the neutron source and the neutron detector with a timing of several 100 ns, the slow component waits for the slow light decay time of the $CaWO_4$ scintillation which is $\tau = 12\mu$s. For the determination of τ see Figure 6.17. If a fast coincidence condition (see next section) is fulfilled, an acceptance window ("Master Gate") opens to wait for the $CaWO_4$ trigger. If the fast and slow decisions are positive a *Master LAM* (LAM = "Look-at-me") is set to indicate the polling software DAQ to read out the data stored in the appropriate CAMAC modules.

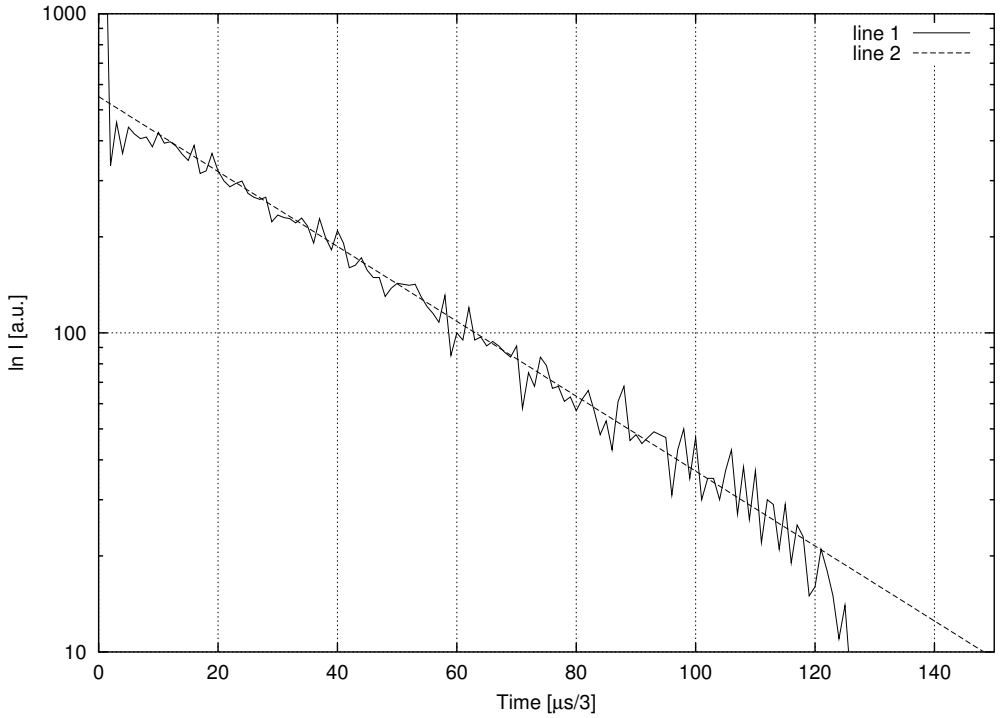

Figure 6.17: The $CaWO_4$ decay time at room temperature: the scintillator was irradiated by a Fe-55 source and the anode signals were recorded. The time origin of every pulse was assumed to be the first arriving photo-electron, all events were shifted in time to match a common starting point, then the anode traces of many scintillation events are added (line 1). The abscissa of this plot is the logarithm of the added intensities if different pulse heights in the anode spikes corresponding to single PE's are time-independent. The linear fit (line 2) provides the decay time of 12.3 ± 0.3 μs with no more than one decay constant. The artificial pile-up of the first PE raises the intensity of the first channel and reduces the intensity in a few following channels, the drop-off at 40 μs is due to the record length of the hardware DAQ.

Fast coincidence

One of the main guidelines for trigger generation is the reduction of dead time, leading to the principle that in a coincidence setup the one which triggers least generates the gate. For example, in the simple ToF setup (Subsection 6.1.3) where neutrons from a pulsed beam fly straight from the reaction chamber to the neutron detector, this neutron detector opens a gate to wait for the information whether there was a bunch or not (for it may also happen that an ambient radioactive decay or a muon triggered the neutron

detector). In order to rule out a significant contribution of multiple detector events that happen too close to each other to be individually identified (*pile-up*), it is trivial to state that the neutron detector will trigger less often than the source emits neutrons (that is: boron bunches arrive at the reaction chamber). But how do we know when bunches arrive at the target?

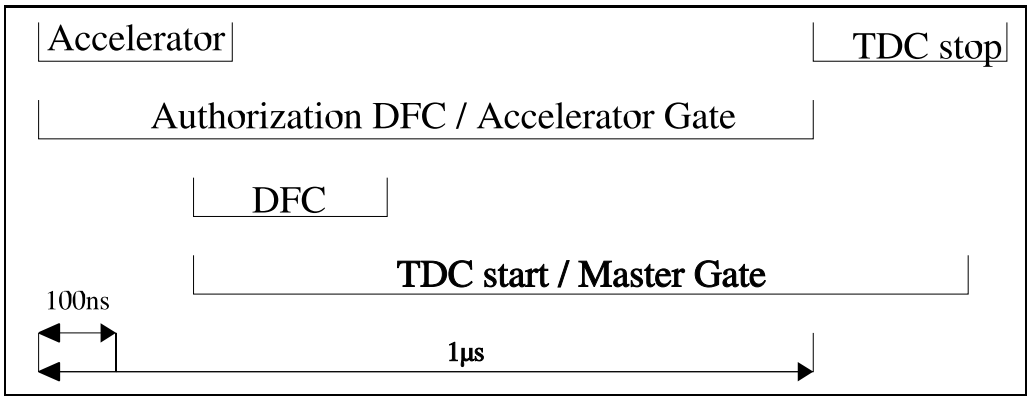

Figure 6.18: $CaWO_4$ Trigger setup: fast coincidence gates.

Among various possible solutions we decided to take the accelerator pulsing information to be the ToF stop condition. The LE chopper provides a signal of the selected frequency (because primarily it chops the beam into packets, Section 6.1.2). On the other hand, the HE chopper pick-up provides a phase information with a jitter corresponding to less than 1 ns; this control adjusts within parts of a second ("Phasenregelung"). Combining both signals, an accurate timing signal with arbitrary but fixed delay (given by the ToF of the boron ions through the beamline tube) is provided. Application of an appropriate delay shifts this accelerator signal into the time domain of neutron generation.

The block diagram of the fast coincidence part of the hardware DAQ is shown in Figure 6.19. Every group of eight neutron detectors checks its own coincidence condition with the accelerator gate. As a result the neutron detectors start only the TDC of their own group. Hence it is possible to check whether different groups trigger within the same accelerator gate which is called "multiple group events".

Slow coincidence

Once the fast coincidence condition is fulfilled, the master gate opens to wait for the $CaWO_4$ cross-over trigger from at least one of the two PMs that observe the $CaWO_4$ crystal. The master gate is shifted with respect to the fast coincidence signal according to the cross-over (CO) timing ($\sim 20\mu$ s).

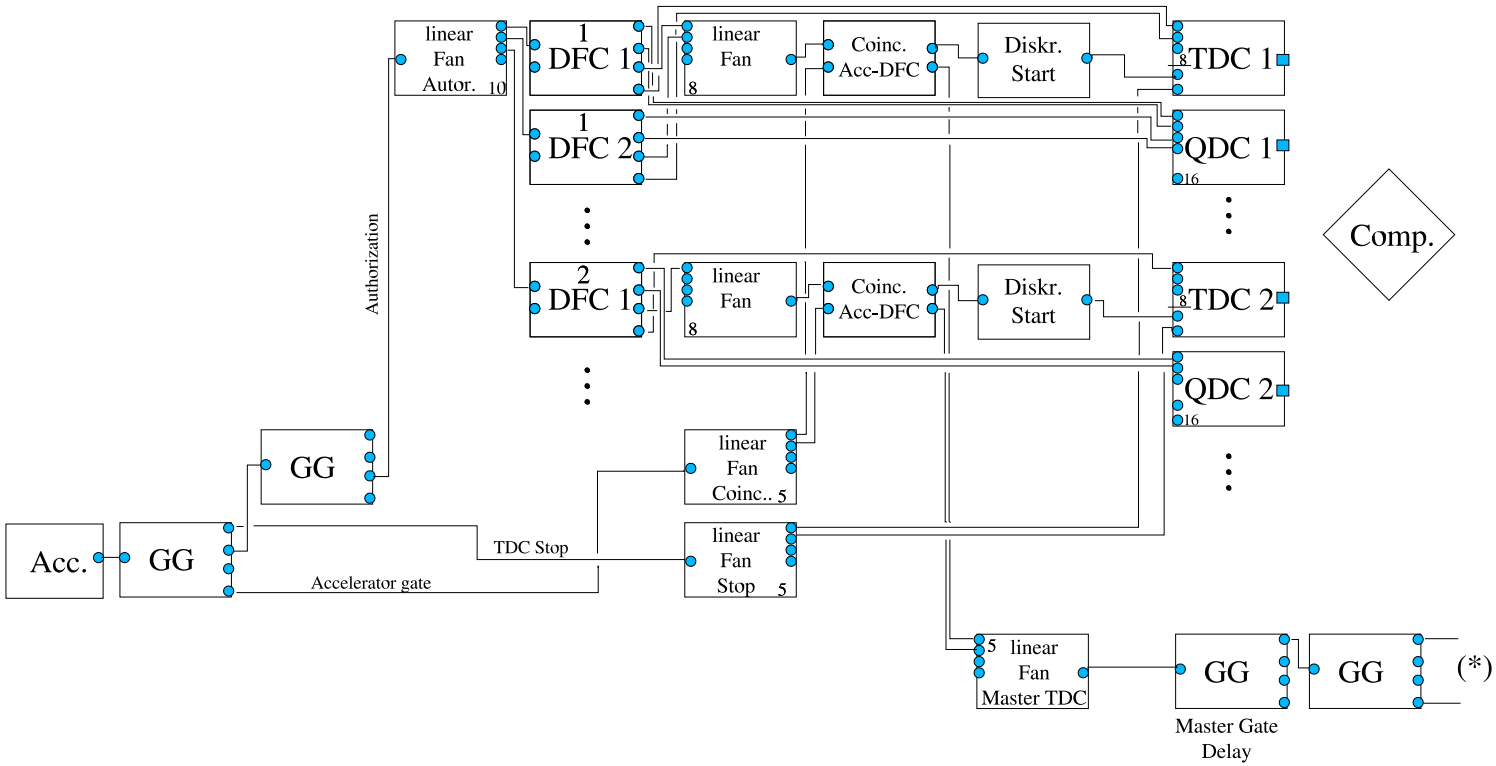

Figure 6.19: Schematic diagram of the fast coincidence part of the hardware DAQ. The module caption is the same as in Figure 6.22. (*) marks the connection to the slow coincidence part of the DAQ. A filled square denotes DAQ from the computer.

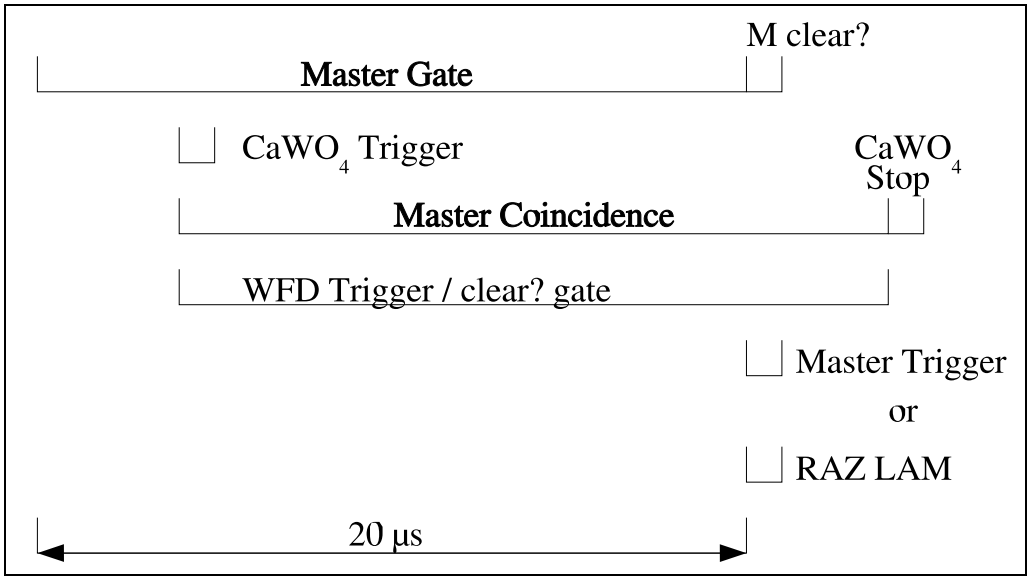

Figure 6.20: $CaWO_4$ Trigger setup: slow coincidence gates.

The time resolution of the hardware CO trigger is worse than the bunch repetition intervals, so the master gate opens for typically 15-20 μs which covers the arrival of several preceding and following bunches. The recording of several preceding and following bunches, with all coincidence requirements met, provides a powerful tool in the offline data analysis where the FPET is used to determine the trigger timings much sharper than with CO timing: Around the bunch that is due to physically true coincidences between accelerator, central detector and neutron detectors, neighboring event clusters appear with the time intervals given by the accelerator pulsing. Event rates in these neighboring bunches are used to determine the background rate in the central (physically true coincident) bunch (details below). The neighboring bunch cluster contain events each in the central and ring detectors that are each related to the boron bunch arrival at the hydrogen target, but there is obviously no relation between the event in the central detector and the event in the neutron detectors. For instance it may happen that, say, a neutron from bunch number 1 is scattered anywhere from the central detector: the coincidence between central detector and accelerator is met. Let a neutron from the following bunch number 2 scatter anywhere in the experimental surrounding (or penetrating the shielding) and be detected in the neutron detector without having scattered from the central detector. In this case, the coincidence between neutron detector and accelerator is met. Although both events, central scattering from bunch 1 and neutron detection from bunch 2, are physically uncorrelated, they will be recorded by the DAQ.

This consideration holds for every possible bunch interval within the master gate and gives rise to satellite peaks on either side of the central bunch in the walk-plot (Figure 6.21).

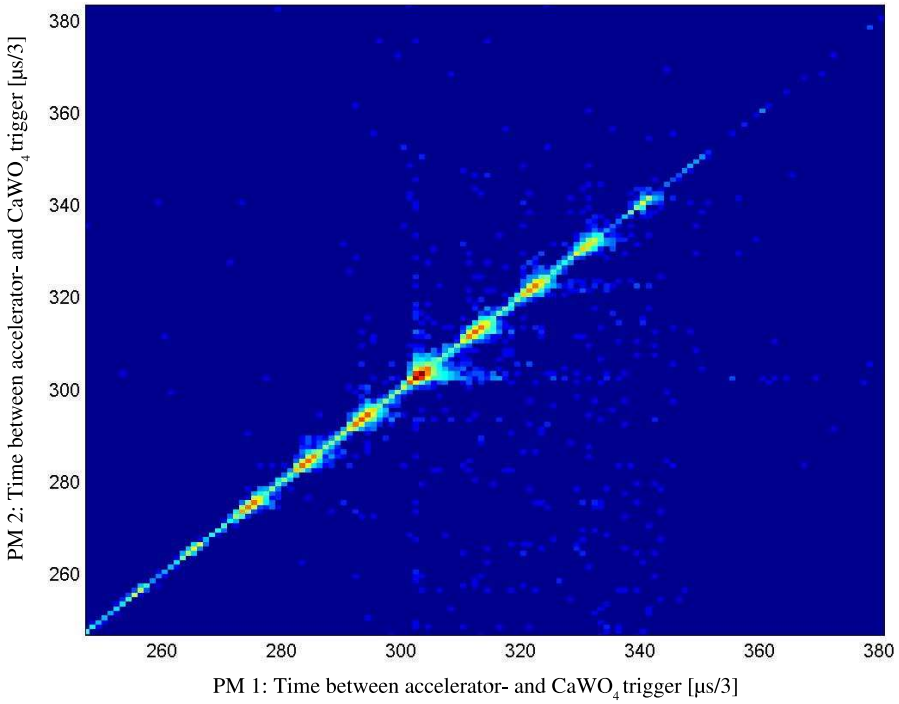

Figure 6.21: The $CaWO_4$ neutron scattering using a double detector: time between the accelerator- and the FPET $CaWO_4$ trigger of PM 2 vs. PM 1 without ToF- or n/γ-cut (the times on each axis is given by the time needed to produce the cross-over trigger compared to the signal onset). The different accelerator bunches with a spacing of 3.2 μs within a hardware acceptance gate of 25 μs width are colour-coded by the number of recorded events (red: high, blue: low). The central bunch at $\sim$ 303 μs/3 represents mainly true (physical) coincidences whereas the neighboring peaks show beam correlated coincidences.

If a $CaWO_4$ trigger arrives within the master gate, a separate CAMAC LAM is set indicating a read-out event to the polling software DAQ, otherwise a Clear LAM is set to indicate that the stored data from the neutron detectors should be erased. Figure 6.21 shows the number of recorded $CaWO_4$ triggers of PM 2 vs. PM 1 in dependence on the time that passed since the fast coincidence trigger was set. The accelerator bunches appear with a high

event rate every 3.2μs.

Figure 6.22 shows the block diagram of the slow coincidence part of the hardware DAQ and the definition of the module blocks. The CAMAC 1024 Trigger is used to indicate the read-out LAM to the computer, the TDC RAZ is used to indicate the clear LAM signal to the computer.

QDC and TDC data are stored in the CAMAC modules until the slow coincidence decision is made. The DAQ program reacts to the Master LAM by starting the readout procedure of the neutron detector data and $CaWO_4$ pulses and to the clear LAM by a fresh reset and arming of the assembly. The offline FPET can be evaluated by adding the fast coincidence logical signal to one slow trace.

The central bunch that contains physically true events is identified by the majority of neutron events in the outer detectors after having passed an appropriate ToF cut. The identification of the central bunch in turn provides a cut (*walk cut*) that further cleans the ToF spectrum from accidental coincidences. The loss of life time during the master gate check could be prevented in future setups by recording the fast and slow coincidence event traces independently from each other, while a common clock provides the time information.

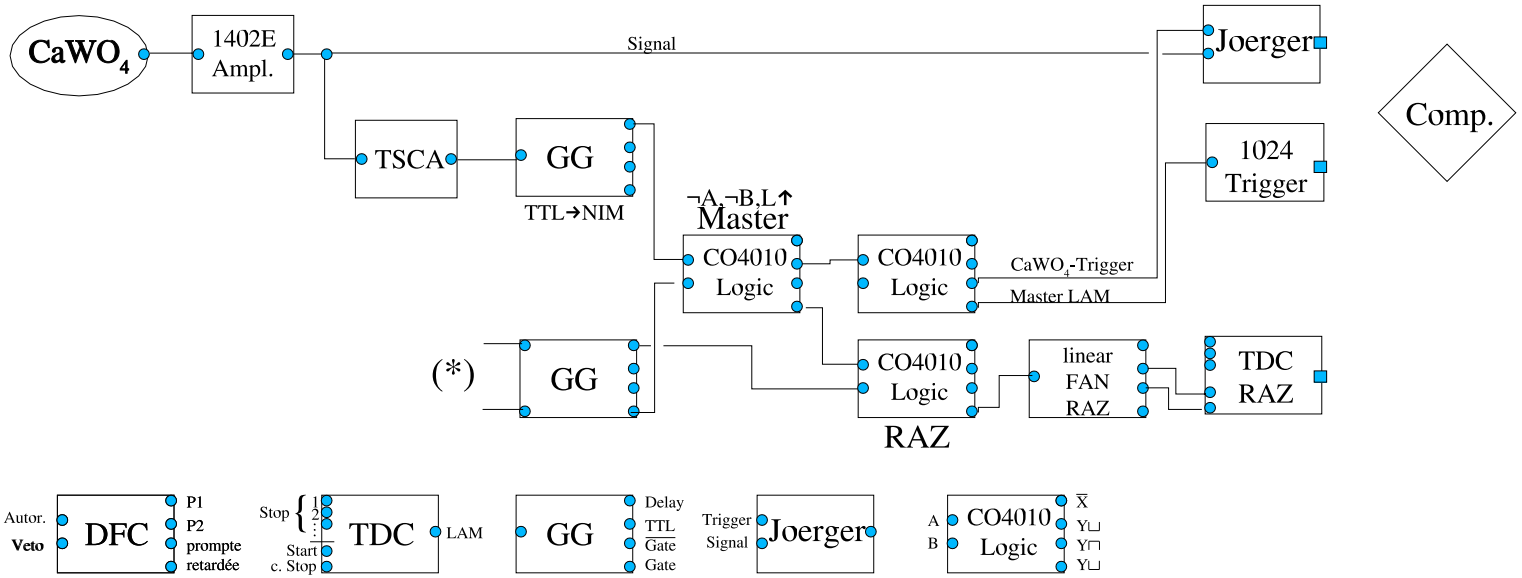

Figure 6.22: . Schematic diagram of the slow coincidence part of the hardware DAQ and module caption. (*) marks the connection to the fast coincidence part of the DAQ. A filled square denotes DAQ from the computer.

Chapter 7

Quenching Results and Discussion

7.1 NE213 Scintillator with Am-Be-source

As introduced in Section 2.6, to get first information about Quenching Factors without all the complications of running an accelerator and slow trigger timings (as in the case of $CaWO_4$), and, from the technical point of view, check the assembled experimental setup, a simplification can be realized by

(a) irradiating a fast (compared to the neutron flight duration) detector like NE213 instead of the slow $CaWO_4$

(b) with neutrons of a continuous energy spectrum (from an Am-Be source) instead of using an accelerator, and keep the scattering angle fixed.

Given a NE213 neutron detector to act as central detector for recoil Quenching measurements, the similarity of central and outer detectors on the one hand generates redundant information with respect to their ability in n/γ-discrimination and fast trigger generation, providing on the other hand an instructive tool for analysis of the physical situation in a scattering experiment under well-investigated conditions. Such tests involving neutron sources will help with the interpretation of results obtained with more complicated setups where the central detector is either not capable of particle identification (NaI) or too slow for timing information, or even both ($CaWO_4$).

Neutron sources at hand might be a Californium-252 or an Americium-241/Beryllium neutron source (Figure 7.1). In the latter case ^{241}Am emits an α-particle ($^{241}_{95}\mathrm{Am} \rightarrow {}^{237}_{93}\mathrm{Np}^{(*)} + \alpha$) which is absorbed by Be under neutron emission. $\mathrm{Np}^{(*)}$ stays in its 2^{nd} excited state in 85% of all disintegrations, from there it decays within 67 ns to the ground state (60 keV, Table 6.2) or to

the 1st excited state at 33 keV. This trigger time delay due to the decay time of the gamma emission coincides with typical neutron ToF values sometimes giving rise to a misleading interpretation of coincidences. The alpha particle (Q = 5.6 MeV) after being slowed down is captured by Be: ${}^{9}_{4}\mathrm{Be} + \alpha \rightarrow {}^{13}_{6}\mathrm{C}^{*}$. The neutron spectrum of Figure 7.1 results from the de-excitation of this highly excited ($E \gg S_n = 4.9$ MeV) carbon nucleus: ${}^{13}_{6}\mathrm{C}^{*} \rightarrow {}^{12}_{6}\mathrm{C}^{*}+$ n. The gamma spectrum of Figure 7.2 is mainly given by the final deexcitation of the excited carbon nucleus: ${}^{12}_{6}\mathrm{C}^{*} \rightarrow {}^{12}\mathrm{C} + \gamma$, where the cutoff-energy is the first excited level of ${}^{12}\mathrm{C}$ at 4.4 MeV, see Table 6.2.

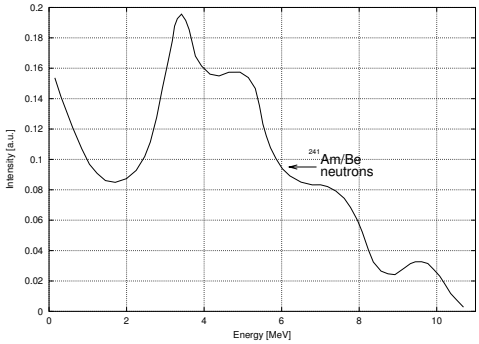

Figure 7.1: Neutron spectrum.

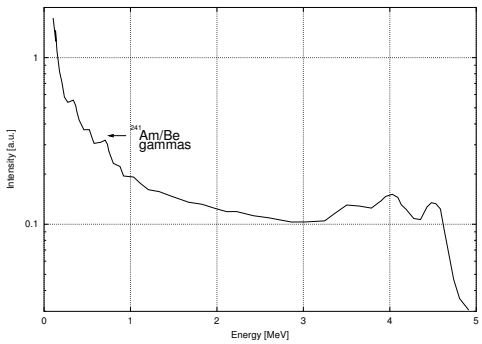

Figure 7.2: Gamma spectrum.

Figures 7.1 and 7.2: Americium-241/Beryllium source [2]. The gamma spectrum is not intrinsic of the source, but already folded with the detector response. This is obvious from the Compton continuum below the full-energy peak at 4.4 MeV (cf. Table 6.2), accompanied by the single and double escape peaks (pair production) to the left.

Figure 7.3 shows a scatter plot of a NE 213 neutron detector irradiated by neutrons and gammas from an Am/Be-source, observed by eight neutron detectors mounted on a ring with radius 1.20 m under 40° scattering angle in the laboratory system. The setup is similar to that in Figure 2.5 with the "pulsed neutron source" replaced by the "Am/Be-source". The distance between the central detector and the ring centre was 1.43 m, resulting in a flight path length of 1.86 m for the scattered particles. The central detector (PM No. 10) is the same as the one in Figures 2.4 and 6.12.

Both central and ring detectors respond fast compared to the neutron ToF thus allowing for a sharp start and stop time information. In Figure 7.3, due to trigger reversal (neutron detectors start the clock which is stopped by the central detector) time is running from right to left (lower ToF channels indicating a slower motion). The y-coordinate shows the light yield according to the energy deposition in the central detector. The energy signal is obtained

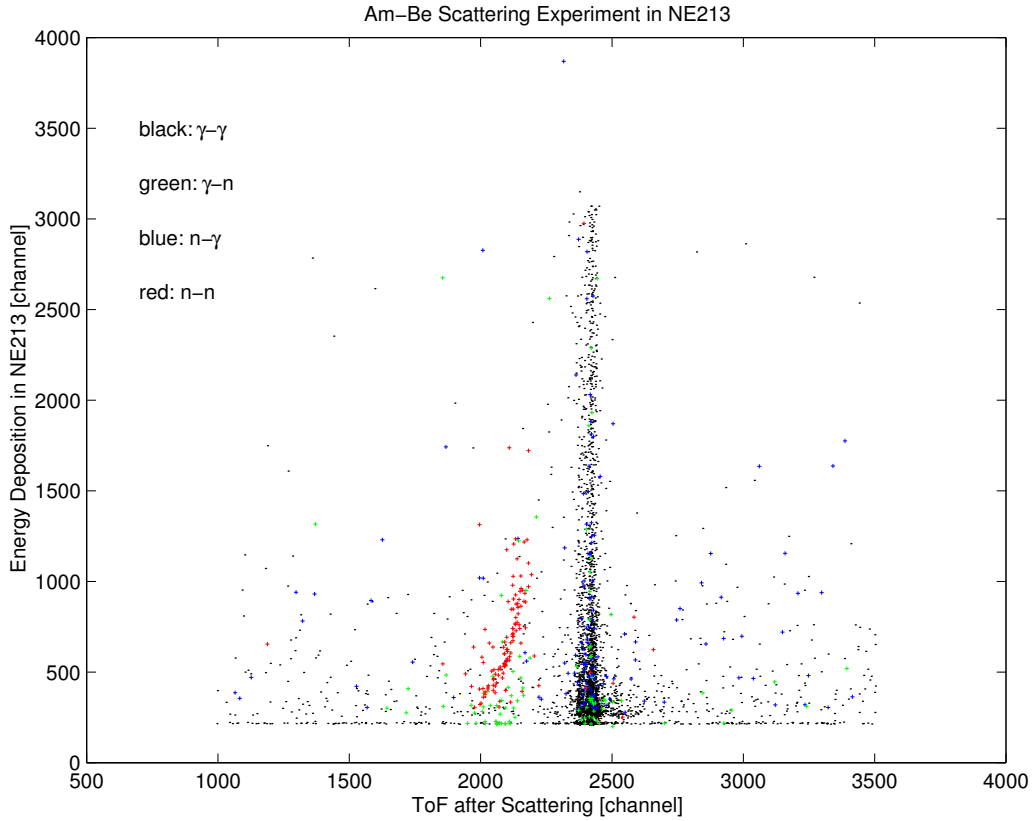

Figure 7.3: Typical raw scatter plot of a neutron/gamma scattering experiment exhibiting data without any cuts. Here: The NE 213 scintillator irradiated by neutrons and gammas of an Am/Be-source and observed under 40° scattering angle (further explanations in the text).

from a coincidence trigger setup providing the correspondence of the QDC charge integration with the ToF signals. (For the energy calibration see Figure 6.12).

The colour codes in Figures 7.3 and 7.4 refer to the results of the pulse shape analysis in the central and any of the outer detectors: black dots denote gamma identification in both detectors while red crosses denote neutron identification in both detectors. The blue crosses mark neutrons in the central detector and a coincident gamma in the outer detectors, green crosses the situation vice versa.

From Figure 7.4 it is evident that gamma interaction in the central detector is independent of gamma flight duration as expected from the constant speed of light c. Further on we will use these gamma peaks as timing reference since we can define the ToF zero point, which is the same for both neutron

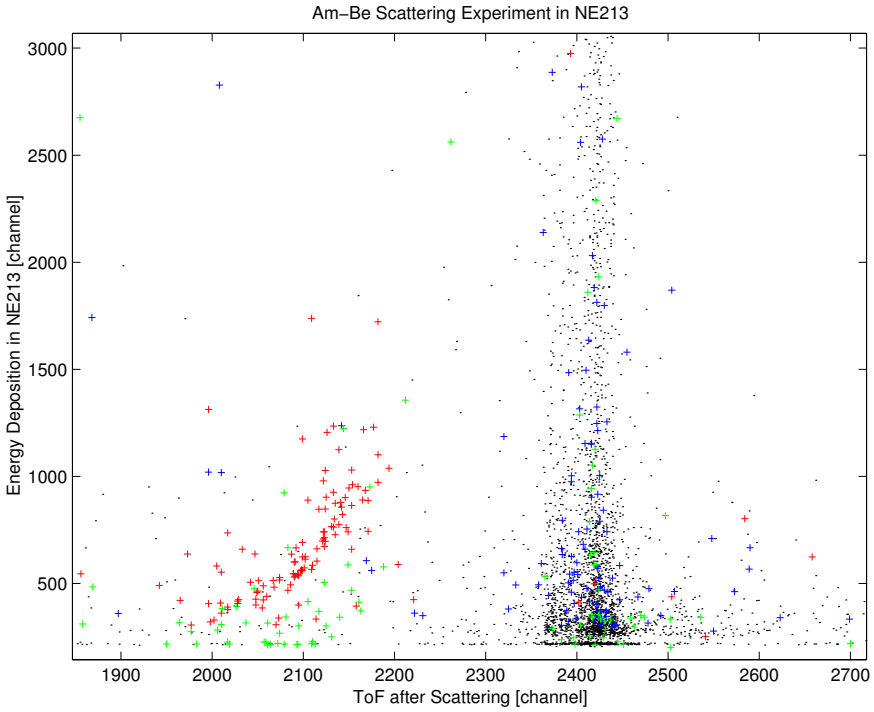

Figure 7.4: Same figure as Figure 7.3, but zoomed in: The NE 213 scintillator irradiated by neutrons and gammas of an Am/Be-source, observed under 40° scattering angle.

and gamma interaction in the central detector, by subtracting the gamma ToF from the peak location (flight distance divided by c). The gamma peak seems to be split into two parts of slightly different flight duration. A detailed analysis of various shielded and unshielded flight paths revealed that the origin of the first pronounced gamma peak are coincident gammas from a single disintegration within the source interacting independently in the central and outer detectors, whereas the later less pronounced peak comes from true gamma scattering in the central detector.

The second marked feature is the band of neutrons elastically scattered by hydrogen in the liquid scintillator. The spectrum is continuous with an energy deposition roughly following a t^{-2} law as expected from a continuous neutron source spectrum (cf. Figure 7.1, see also appendix A, Eq. (A.33)).

Blue crosses (n-γ events) are located right upon the gamma peak and denote a neutron in the central detector scattered anywhere and a gamma of the same source disintegration recorded by the outer detectors. The short distance between the source and the central detector lets these events look

much like a gamma flying from the central to the outer detector.

Events that show up as a gamma in the central detector and a neutron in the ring detector are displayed by green crosses. Due to the high neutron separation energy of ^{12}C ($S_n = 18.7$ MeV) it is impossible to produce gamma-induced neutrons in the scintillator. Moreover, in the energy region of interest elastic scattering by hydrogen and carbon dominate (Figure 6.8) since the first carbon excitation level is at 4.4 MeV. ToF measurements combined with pulse-shape analysis prove that despite nearly perfect n/γ-discrimination still some events that definitely have to be attributed to neutron interaction show gamma signature (Figure 6.6). These events are interpreted as inelastic reactions either in the scintillator itself (carbon without taking notice of the highly quenched carbon recoil [16]) or inelastic reactions in the close vicinity of the scintillator, e.g. the scintillator housing. Anyway only the gamma of this reaction is detected (while the timing is determined by the ToF of the neutron) so that neutron identification is not completely unambiguous.

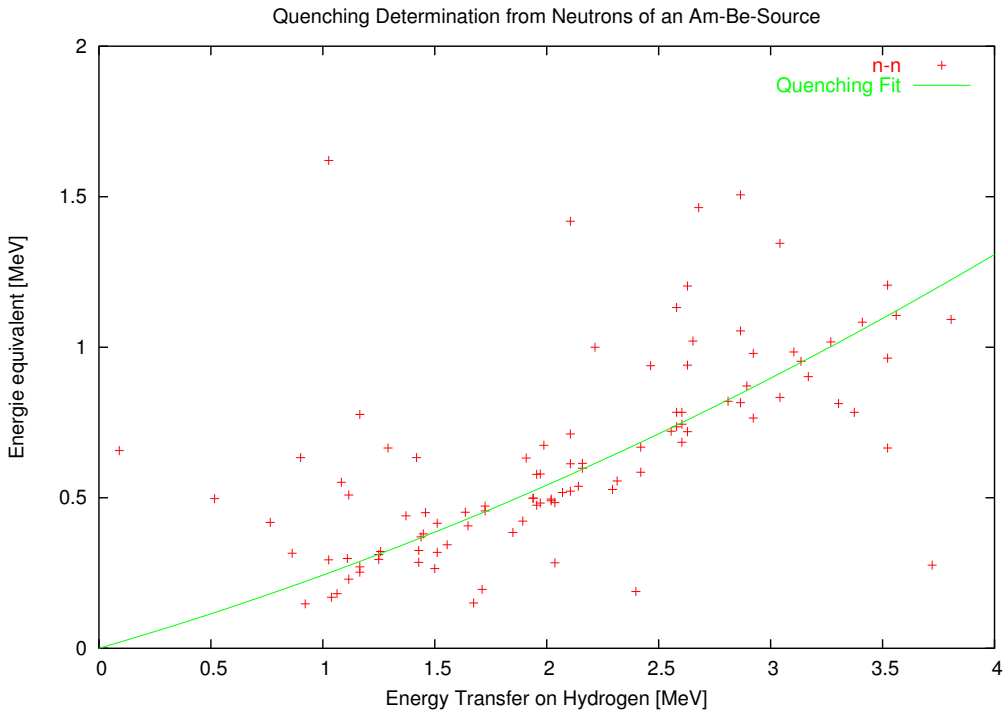

Figure 7.5: Measured electron-equivalent energy of elastically scattered neutrons from an Am-Be-source plotted versus the proton recoil calculated from the ToF of the scattered neutron. For comparison, the energy-dependent Quenching function $E_{ee} = 0.215E_p + 0.028E_p^2$ (see Equation (6.6)) is also shown.

Figure 7.5 shows the measured electron-equivalent energy vs. the proton recoil energy. The Quenching function of Equation (6.6) fits very well to the measurement. The energy dependent Quenching function of hydrogen in NE 213 was already measured by [41] and [47], additionally the corresponding Quenching function for carbon in [16].

7.2 NE213 Scintillator with p(^{11}B,n)^{11}C Reaction

The next step towards a scattering experiment with $CaWO_4$ is done by replacing the continuous Am-Be neutron source by monoenergetic neutrons from the inverse (p,n) reaction. This is the first time that the tandem accelerator gets involved in the scattering experiment. Measurement campaigns are organized in *beamtimes*, i.e. measurement time (smallest unit is one "bit" = half a day) is allocated to the different groups that use the tandem accelerator. A typical beamtime lasts about 1 to 2 weeks, 24 hours a day. In total, i.e. including all Quenching measurements presented in this work, 13 beamtimes were performed throughout four years. The first one or two days of a beamtime are needed to set up the accelerator by a proper installation of the boron source and the threading of the beam through the beamline onto the experimental target. Usually a third day is necessary to adjust the pulsing of the beam. Accounting for experimental challenges due to reconstructions and modifications of the scattering setup itself, which takes again usually one or two days, actual Quenching measurements start about 4 to 5 days after the beamtime has officially begun. Preperations of new setups to be probed in beamtimes usually take 1 to 3 months in advance, the data evaluation from scattering data takes several weeks and deals with the order of 10 GByte of data from individual beamtimes.

While the neutron detectors in all scattering arrangements were shielded by about 0.5 m polyethylene (or water), there was never a similar (lead) shield used against direct gamma irradiation from the source. As already outlined in Section 7.1 the prominent gamma peak originates from "*accidental*" coincidences of source disintegrations leading to at least two gammas, one of them hitting the central detector and the other one reaching the neutron detector. In the following any type of these coincidences will be called *beam correlated* coincidences and will be distinguished from true accidental coincidences, the latter being referred to as *random* coincidences (e.g. trigger from ambient radioactivity or cosmic muons). The similarity of the gamma spectrum produced this way in the central detector and the corresponding

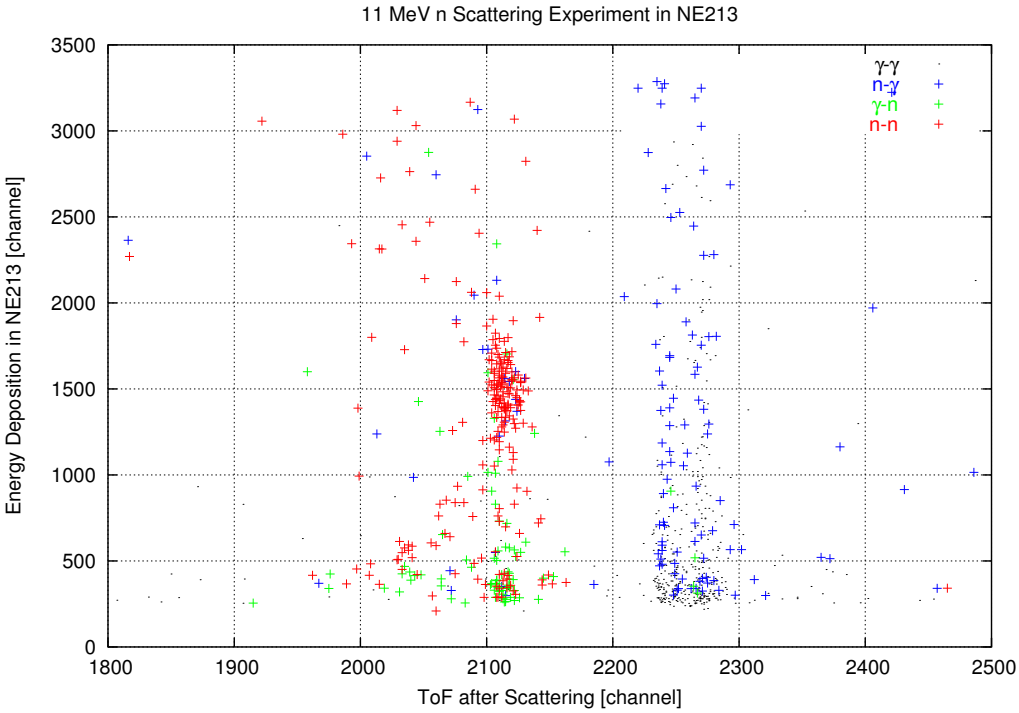

Figure 7.6: The NE 213 scintillator irradiated by neutrons and gammas originating in the hydrogen target, observed under 32° scattering angle. Compare with Figure 7.4.

spectrum of the Am-Be source indicates that the dominant gamma fraction comes from p(^{11}B,γ)^{12}C and thus leads to the Compton continuum of the first excited level of ^{12}C as in the case of the Am-Be source. Moreover, the fact that these spectra are similar together with the absence of the single Compton line (recoil electron from Compton scattering) in the central detector again supports the interpretation of beam correlated coincidences (together with the ToF argument mentioned above).

Figure 7.6 is the complement of Figure 7.4 with the Am-Be source replaced by the monoenergetic 11 MeV neutrons from the boron reaction (under a slightly different scattering angle). The change in the n-n event population (red crosses) due to the higher proton recoil energy is obvious (the energy calibration of the y-axis did not change). The faint tail of low energy neutrons from the reaction chamber following the t^{-2} law is clearly visible. Higher energy depositions than the hydrogen elastic recoil are attributed to multiple (hydrogen) scatters in the scintillator, leading to a longer ToF due to a higher energy loss of the scattered neutron. Similarly, lower (and part of the higher) energy depositions than the single hydrogen recoil can be well

Specific Gravity	Wavelength of Maximum Emission λ_{max}	Index of Refraction at λ_{max}	Principal Decay Constant	Pulse 10–90% Rise Time	Total Light Yield in Photons per MeV	Absolute Scintillation Efficiency for Fast Electrons
3.67	415 nm	1.85	0.23 μs	0.5 μs	38000	11.3 %

Table 7.1: Properties of NaI(Tl) [20]. The 10-90% "rise" time of the pulse refers to the principal decay constant.

explained by a combination of carbon and hydrogen scatters: the carbon cross section favors small angle deflections (undetected) leading to a smaller hydrogen deflection angle than that expected from single scattering from hydrogen. Hence the energy deposition seems to be smaller.

7.3 NaI(Tl) Detector with p(^{11}B,n)^{11}C Reaction

The next stage aiming at a multidetector system in a scattering setup is the recoil measurement in a well-known scintillator at room temperature with intrinsic decay times intermediate between that of the fast organic scintillators and that of the rather slow $CaWO_4$. This way also the trigger system can be tested in view of the the later setup where $CaWO_4$ will be investigated. We have chosen Thallium-doped Sodium Iodide NaI(Tl). The light output from the 2-inch scintillator was measured by a HARSHAW photomultiplier and digitized by an ORTEC ADC. Linearity of the NaI(Tl) electron recoil response was confirmed by calibration with Am-241, Na-22 and Cs-137 (Table 6.2).

The central trigger (see Subsection 6.5.4) was generated using the cross-over method (zero crossing of bipolar pulses from double differentiation). A complication of this trigger setup is arising from the light emission decay time τ in NaI(Tl) of 0.23 μs (Table 7.1) which is longer than that of NE 213. The PM pulse is filtered by a capacitor/resistor combination between PM anode (dynode) and preamplifier. It is integrated over several light decay times $RC \gg \tau$ in order to achieve proportionality between signal pulse height and collected charge [20]. Therefore, the signal rise time is determined by the light collection time within the detector itself. Thus the timing resolution is worse compared to that described in Section 7.2 where the Quenching factor of NE213 was measured. In addition, DAQ timing needs to be adapted

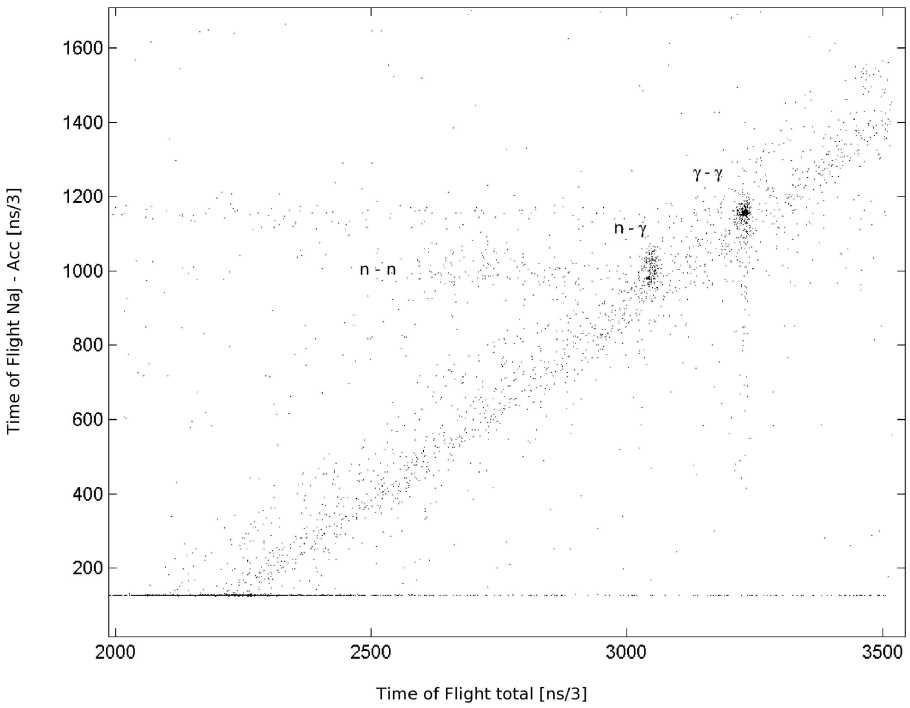

Figure 7.7: The NaI(Tl) scintillator irradiated by neutrons and gammas originating in the hydrogen target, observed under 90° scattering angle. ToF Accelerator–NaI(Tl) versus total ToF. The time is displayed in reversed direction due to the trigger realization: right to left and top to bottom, only time intervals are calibrated. Event categories see text.

to an operation involving different trigger generation and pulse amplitude digitization.

An aggravating circumstance is given by the fact that pulse-shape analysis in NaI(Tl) for neutron/gamma discrimination is much more complex than in NE 213 that was specifically designed for that purpose (Sections 7.1 and 7.2). So it was decided to manage the data acquisition and analysis without intrinsic particle identification in the central detector in contrast to the previous setups. Fortunately the cross-over trigger, being independent on amplitude, is still precise enough considering that the time jitter and the walk are smaller than the time resolution of the neutron ToF (see Chapter 2). Figure 7.7 shows the separation of neutrons and gammas by ToF when travelling between reaction chamber, central detector and neutron detectors. Hence these triggers still prove the feasibility of neutron/gamma identifica-

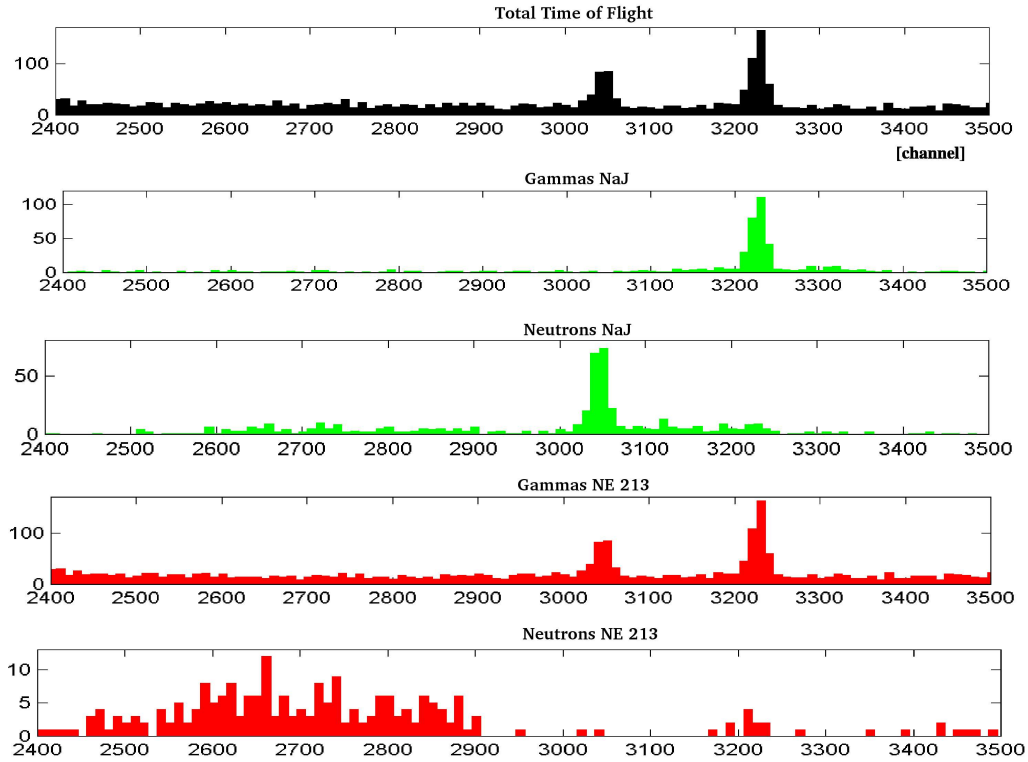

Figure 7.8: The NaI(Tl) scintillator irradiated by neutrons and gammas originating in the hydrogen target, observed under 90° scattering angle: Total Time-of-Flight histograms of gammas and neutrons between reaction chamber and NE 213 (via central detector NaI(Tl)). Top: All recorded events. Second: Events with γ ToF between reaction chamber and NaI. Third: Events with neutron ToF between reaction chamber and NaI. Fourth: Events with γ induced pulseshape in NE 213 (neutron detectors). Bottom: Events with neutron induced pulseshape in NE 213. Attention: the ordinate scale (number of counts) is varying.

tion in the central scatterer by the different particle ToF values between the reaction chamber and the NaI detector. By comparison of central detector timing with PSD in the neutron detectors, Figure 7.8 shows a clear event separation which depends on the type of particle interaction in both central and neutron detectors.

Figure 7.9 relates the energy deposition in the central detector to the total ToF for all event categories discussed in previous sections. Eight neutron detectors were mounted on a ring with radius 1.2 m and shielded by 0.5 m polyethylene in direct line-of-sight against the reaction chamber. The dis-

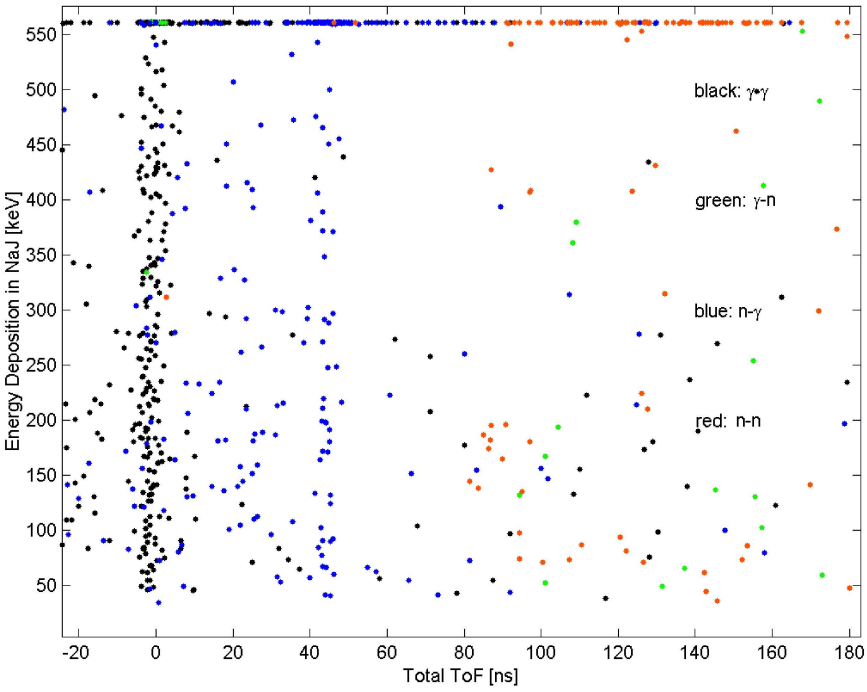

Figure 7.9: The NaI(Tl) scintillator irradiated by neutrons and gammas from the hydrogen target, observed under 90° scattering angle: energy deposition in the central detector versus total ToF. For realization of n/γ-discrimination see text. Compare this figure with Figure 7.6

tance between the reaction chamber and the ring center was 2.02 m resulting in a scattering angle of 90° in the laboratory frame and 2.35 m, as the crow flies. The same event classes as discussed in connection with the Figures 7.6 and 7.4 appear again: The Gamma-Peak, showed in black points, is set to zero in ToF. N-Gamma coincidences are displayed in blue points, their time separation from $\gamma - \gamma$ events is again mainly given by the distance of the central detector from the neutron source. Elastically scattered neutrons (red points) at a total ToF of 88 ns differ well from background.

Figure 7.10 is a selection of all n-n events from Figure 7.9. A table inset lists the cross sections of inelastic contributions expected at higher ToFs. It is apparent that elastic scattering is the dominant process both by sodium and iodide. Since the Quenching factor of iodide is too small to get signals from elastic scattering above the trigger threshold, the dominant reaction type leading to high neutron velocities is elastic scattering from sodium.

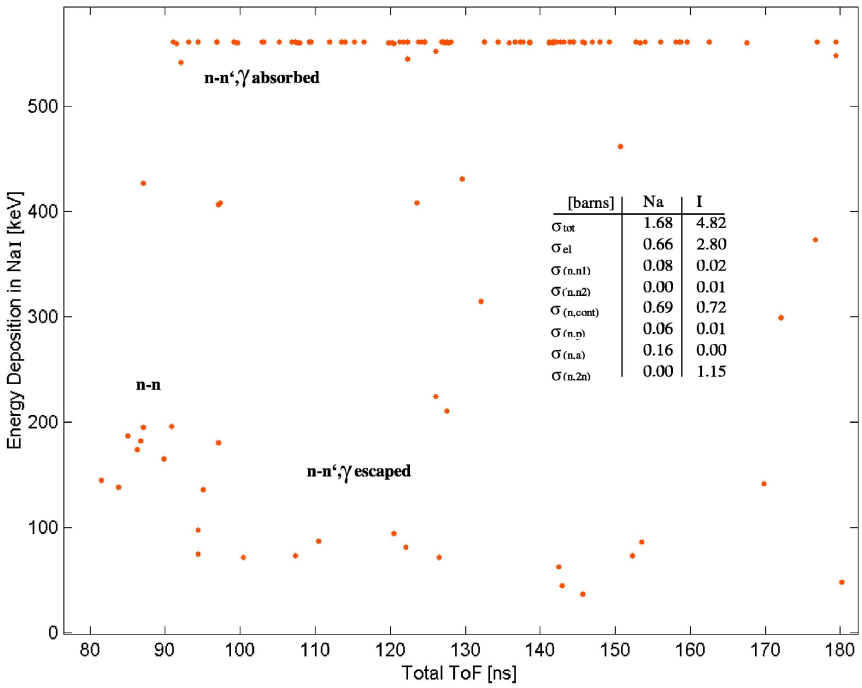

Figure 7.10: The NaI(Tl) scintillator irradiated by neutrons and gammas stemming from the hydrogen target, observed under 90° scattering angle.

The second prevalent process then is the production of a neutron continuum both from sodium and iodide. In the case when the accompanying gamma-ray escapes the crystal, these events form the low-energy tail attached to the group of elastically scattered neutrons by sodium. Most inelastic events with parallel γ-absorption populate the overflow region in this plot. Special attention deserves the fact that the elastic ToF region around 88 ns is free of any inelastic reactions, below and above the elastically scattered neutron region around 180 keV energy deposition. This is also seen even in the overflow pulses (as it is expected). Elastic contributions from iodine-127 are below the trigger threshold due to the high atomic mass of iodine. From the elastic recoil on sodium-23 with a calculated recoil energy deposition of 850 ± 34 keV yielding an electron equivalent amount of scintillation light of 180 ± 20 keV we derive a Quenching Factor of $Q = 0.21 \pm 0.04$ in very good agreement with the published value [40].

7.4 $CaWO_4$ Detector with p(^{11}B,n)^{11}C Reaction

This section deals with the determination of the Quenching factors of the elements in $CaWO_4$. The experimental setup was already described in Section 6.5. The first step in evaluating the data from the scattering experiment consists of the generation of a scatter plot common to all 40 neutron detectors where the energy deposition in the central detector is plotted versus the total ToF of scattered neutrons. For this purpose, the threshold and the n/γ discrimination of every single neutron detector had to be adjusted, often including drifts over the course of the measurement campaign (beamtime). Next their distance to the central detector as well as their scattering angle is considered. Finally, the individual position of the gamma peak in the ToF spectrum must be adjusted which often differs from the absolute time calibration of the TDC's by typically 1-2 ns. This adjustment is necessary since only the TDCs themselves are calibrated, whereas the experimental setup, including slightly different cable length from the detectors (cable length 4 m with a precision of about 1 ns in signal propagation) and accompanying coincidence electronics induce a further time delay which depends on individual PM channels. By accounting for individual shifts of the time spectrum by adjustment of the gamma-peak, this further time spread in the ToF measurement can be avoided.

7.4.1 Overview

Figure 7.12 shows a typical event distribution after application of the n/γ-cuts for all neutron detectors and conversion of the data to a reference distance and a reference scattering angle common to all neutron detectors. In practice, the neutron detectors are arranged in rows at different angles and distances such that the individual scattering angle and distance does not differ much from the mean scattering angle and distance of the group. By using this arrangement it is possible to investigate a possible dependence of the Quenching factors on recoil energy and comparing event rates with cross section predictions without the need of averaging cross sections or Quenching Factors over a large energy range. The collection of data from a sample of detectors arranged in rows that comprise two or three groups of detectors (according to the CAMAC unit grouping, see Subsection 6.4.2) is essential since individual event rates are low after application of all cuts.

Throughout various beamtimes, scattering angles of 80, 100, 108, 120 and 140 degrees were realized which roughly correspond to local maxima

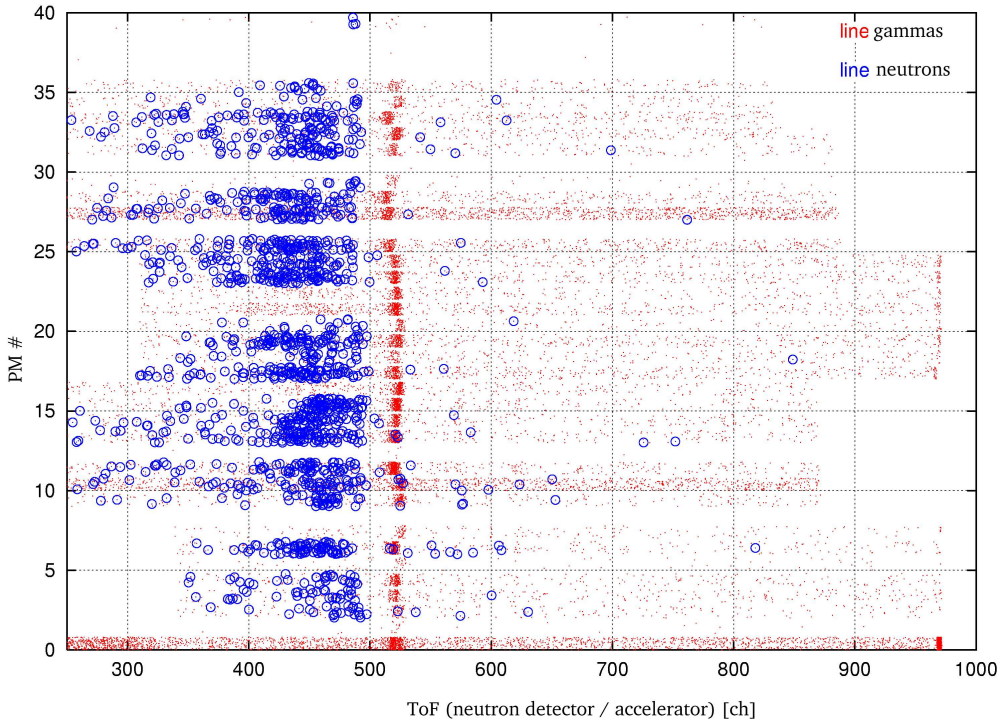

Figure 7.11: 11 MeV Neutrons scattered by $CaWO_4$: ToF and pulse shape discrimination of 40 neutron detectors before the final application of the calibrated alignment of gamma-peaks.

O-16	1095	1523	1684	1907	2209
Ca-40	452	636	707	806	943
W-nat	100	141	158	181	212
	80°	100°	108°	120°	140°

Table 7.2: Energy transfer in keV for 11 MeV neutrons scattered by the different elements in $CaWO_4$ for the specific observation angles (Lab-System) realized in various beamtimes (Fig. 3.7). Different tungsten isotopes are weighted according to their natural abundances (Table 3.1).

and minima of the elastic scattering cross sections of O, Ca and W for 11 MeV neutrons (cf. Figure 3.7). A typical distance of the $CaWO_4$ double detector from the hydrogen target is 10–20 cm, typical distances of the neutron detectors from the central detectors are 100–200 cm. This choice is a

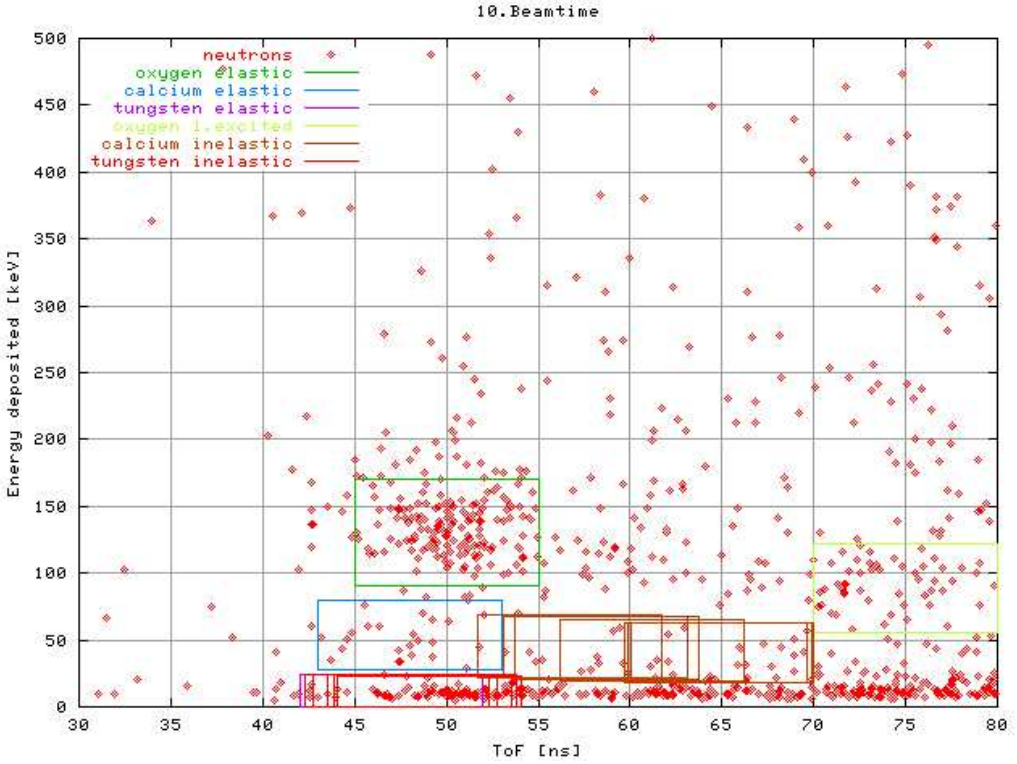

Figure 7.12: The $CaWO_4$ scintillator irradiated by neutrons originating in the hydrogen target, observed under 108° scattering angle: energy deposition in the central detector versus total ToF. Red diamonds show neutron events, differently coloured boxes indicate the predicted positions of those inelastic events where the neutrons do not lose much of their initial energy (see the key of this figure). More details see text.

compromise between ToF and angular resolution on the one side and a large solid angle, giving a high neutron flux, while avoiding pile-up in the central detector on the other side. Concerning the scattering angle, the maximum difference between detectors within one row is usually about 1 degree, and 20 cm as far as the length of the flight path is concerned.

The energy resolution of the $CaWO_4$ scintillator can be derived from the γ- and X-ray calibration decribed in Section 6.5. The ToF resolution (amin contribution from TDC's) is taken from the width of the neutron-peak obtained from the beam characterization (cf. Subsection 6.1.3). The predicted positions in ToF and resolutions both in energy and ToF are plotted in Figure 7.12 for all nuclear reactions that lead to fast scattered neutrons. With increasing ToF, the following features are apparent in plots of this

kind: neutron events emerge with a certain minimum time delay compared to the gamma-peak given by the geometry of the setup (not shown in Figure 7.12, but used to establish the ToF zero point). Neutrons lose least energy in elastic scattering, which moreover dominate for small ToF values since generally their cross section is higher than that for inelastic contributions. These elastic scattering events can be selected by an appropriate ToF window whose vertical position depends on assumed Quenching factors. Inelastic reactions from oxygen and calcium do not contribute significantly within this ToF window since neutrons lose too much kinetic energy, but inelastic reactions on tungsten with partial or full absorption of the corresponding γ-energies do contribute due to the small energy spacing in tungsten nuclei as discussed in Chapter 3.

The next step consists of the data reduction to physically "true" coincidences. Figure 7.13 shows the energy deposition in the $CaWO_4$ crystal versus the FPET onset, with the time delay between the neutron detectors and the FPET set to zero for physically true coincidences.

The total data set can now be reduced by the application of the following cuts:

- **baseline-cut**: applied if the slope of the baselines, recorded from the central detectors by a waveform digitizer, is too steep or too noisy or the pulses clip due to overflow
- **walk-cut**: reduction to the central bunch, i.e. rejection of accidental coincidences
- **n/γ-cut**: restriction to neutrons in the outer neutron detectors by PSD
- **ToF-cut**: restriction to those energies of the scattered neutrons that correspond to elastic scattering

7.4.2 Calcium and Oxygen

As described previously, scintillation light emission from the central $CaWO_4$ crystal is detected by two photomultipliers facing the crystal on opposite sides. Figure 7.14 shows the pulse heights of events in detector 2 versus detector 1 after application of all cuts mentioned above for two different detection angles, recorded during one single beamtime. The prominent clustering of events in the centre of the plot for 100° and in the top right quarter for 140° is due to elastic scattering of neutrons from oxygen. One smaller group of events is observed for each angle at lower energies and is attributed

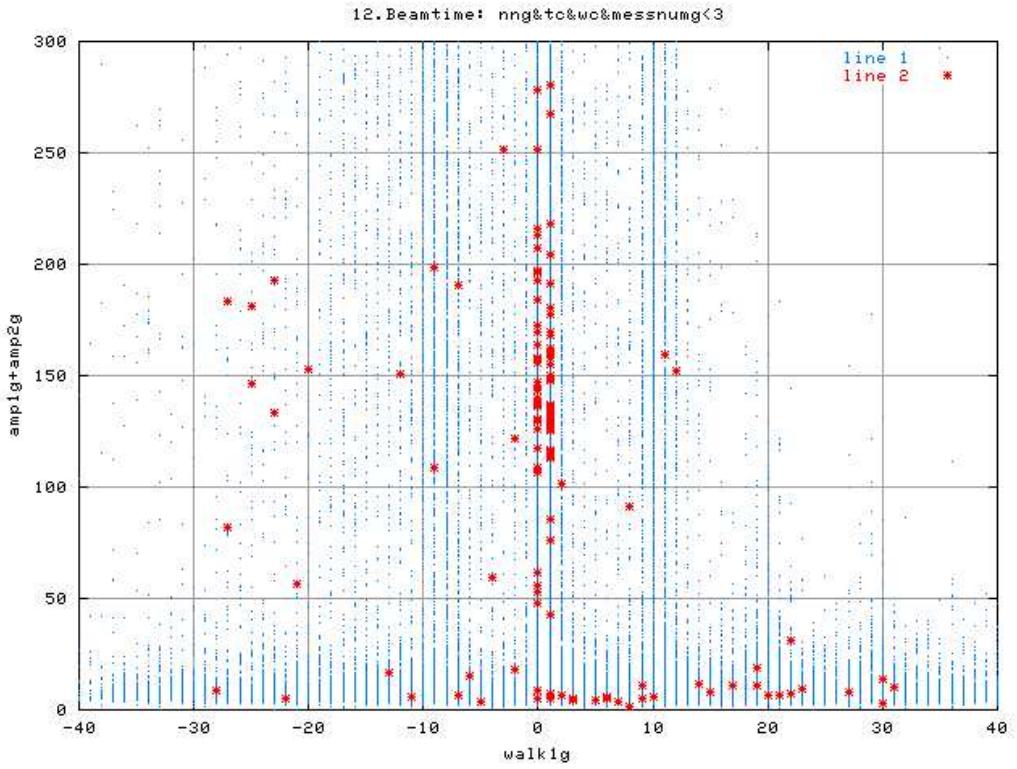

Figure 7.13: The $CaWO_4$ scintillator irradiated by neutrons originating in the hydrogen target, observed under 100° scattering angle: energy deposition in the central detector (amp := "amp1g+amp2g",[a.u.]) versus time delay between accelerator coincidence and $CaWO_4$-Trigger (here called "walk1g" [μs/3]). The accelerator bunch structure is observed in gamma-events in the neutron detectors ("line 1"). Elastically scattered neutrons ("line 2") concentrate at high energies to the central bunch at walk1g = 0. Here the upper part of the peak, roughly at $100 < \text{amp} < 200$, is attributed to elastic recoils of oxygen and the intermediate region at amp ≈ 50 to calcium recoils. For small energies the trigger onset smears towards longer ToF values due to the FPET walk.

to elastic scattering from calcium. In addition, all neutron events (only n/γ-cut applied) are displayed as blue dots. The majority of events at high pulse heights are distributed along the diagonal, i.e. both detectors received light in coincidence. At low energies where the blue dots accumulate mostly only one detector triggered. These events are the dark pulses described in Subsection 6.5.1.

The energy calibration was performed after summing the weighted pulse

E_{ee}[keV]	90 ± 1	123 ± 3	134 ± 6	142 ± 1	164 ± 6
# events	69	208	177	146	86
QF [%]	8.2 ± 0.1	8.1 ± 0.2	8.0 ± 0.4	7.5 ± 0.1	7.4 ± 0.3
angle	80°	100°	108°	120°	140°

Table 7.3: Measurements of the Quenching Factors of oxygen in $CaWO_4$ according to Equation 2.1 for the specific observation angles (Lab-System) realized in various beamtimes: electron-equivalent energy E_{ee} (measured) with statistical uncertainty (1σ), number of events, Quenching Factor (QF). For recoil energies see Table 7.2.

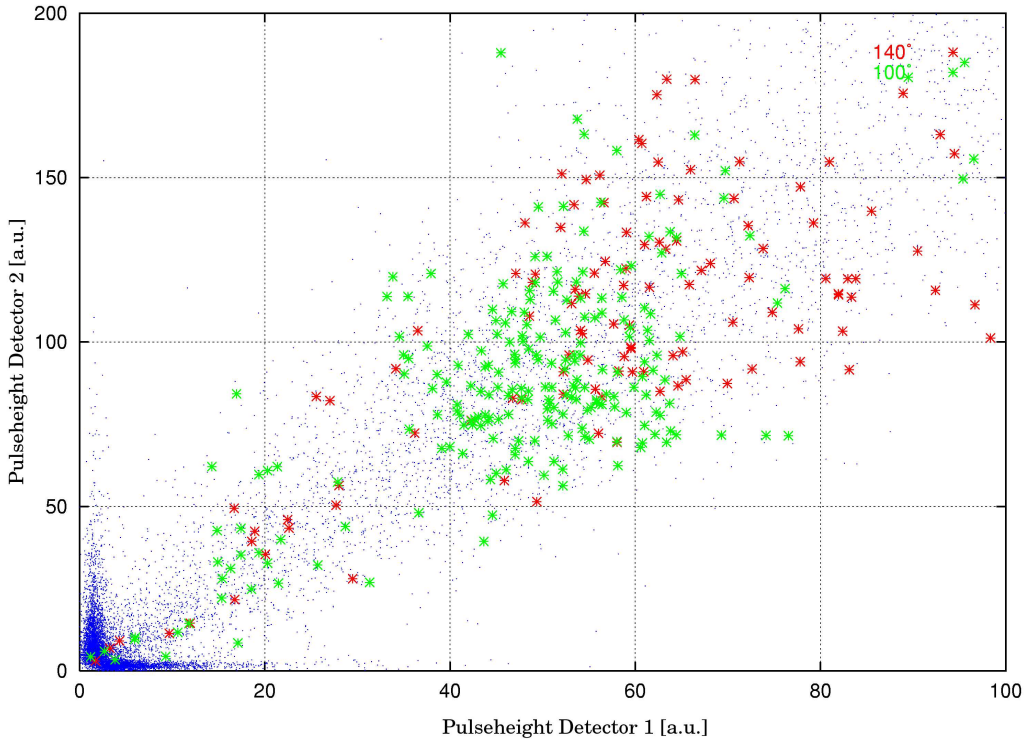

Figure 7.14: The $CaWO_4$ scintillator irradiated by neutrons from the hydrogen target, observed under 100° (green) and 140° (red) scattering angle. The plot shows the energy deposition in the central detector: pulse height of signals in detector 2 versus pulseheight of detector 1 after appication of all cuts (see text). The blue dots denote all neutron events without any cut.

E_{ee}[keV]	20 ± 3	50 ± 7	60 ± 9	56 ± 2	62 ± 6
# events	4	20	27	15	10
QF [%]	4.4 ± 0.7	7.8 ± 1.0	8.5 ± 1.2	7.0 ± 0.3	6.6 ± 0.7
angle	80°	100°	108°	120°	140°

Table 7.4: Measurements of the Quenching Factors of calcium in $CaWO_4$ according to Equation 2.1 for the specific observation angles (Lab-System) realized in various beamtimes: electron-equivalent energy E_{ee}, statistical uncertainty (1σ), number of events, Quenching Factor. Recoil energies see Table 7.2.

$d\sigma(Ca)/d\sigma(O)$ [%]	7.6	14	14	11	8.6
measured event ratio [%]	6 ± 3	10 ± 2	15 ± 3	10 ± 3	12 ± 4
angle	80°	100°	108°	120°	140°

Table 7.5: Predicted cross section ratios $d\sigma(Ca)/d\sigma(O)$ from Table 3.3 and measured ratios R between the number of counts of calcium N_1 and oxygen N_2 recoils from Tables 7.3 and 7.4 for the specific observation angles (Lab-System) realized in various beamtimes. The statistical uncertainty σ_R is calculated by $\sigma_R = \sqrt{N_1^{-1} + N_2^{-1}} \cdot R$.

heights from both detectors, the weights being determined by the resolution of each detector. This analysis was done for all scattering angles under investigation. Tables 7.3 and 7.4 list the number of recorded events, the measured energy and the calculated Quenching factors for oxygen and calcium. Figure 7.15 shows the Quenching measurements for different scattering angles as boxes indicating the statistical uncertainty together with the respective mean values of oxygen and calcium as solid lines. The calculated weighted average in dependence of the scattering angle fits the data reasonably well. Further conclusions about the energy dependence of the Quenching factor for different elements in $CaWO_4$ cannot be drawn since the systematic uncertainty of the measurement is not very well known (see below).

A comparison of the expected and measured numbers of elastic calcium recoils is performed in Table 7.5, where the expected numbers of calcium recoils are derived by multiplying the measured number of oxygen recoils by

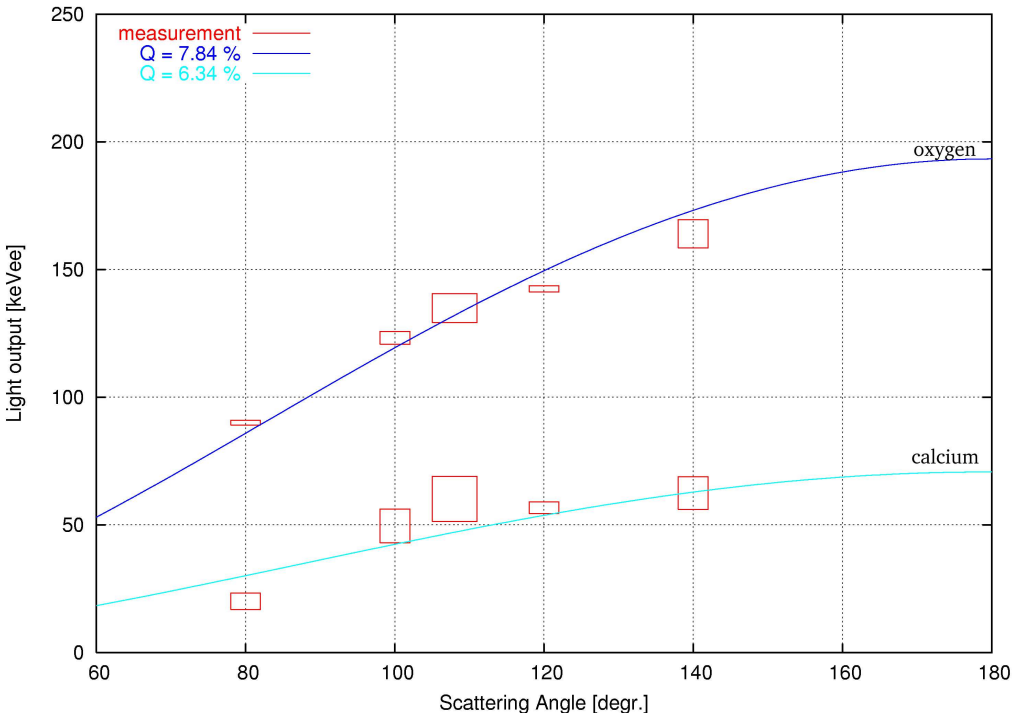

Figure 7.15: The $CaWO_4$ scintillator irradiated by neutrons stemming from the hydrogen target, observed under different scattering angles: energy deposition in the central detector in keVee versus scattering angle (Lab-System). The statistical uncertainties are quoted in Tables 7.3 and 7.4. The height of the boxes indicate the statistical uncertainty in the light output, the width is given by the angular resolution determined by the setup of the neutron detectors. The solid lines represent the angular dependent fit of the mean values for the light output from oxygen (dark blue) and calcium (light blue) recoils assuming that the Quenching factor Q is not dependent on energy on this scale. The Quenching factor is indicated in the top left legend.

the respective cross section ratios. The measurements show a good agreement between the prediction and the measurement.

The identification of oxygen and calcium recoil events is based solely on the occurrence of event clusters, e.g. a clustering in the measured energy deposition, after accounting for neutron events in the outer detectors that occur within a predefined ToF window. Two effects are likely to contribute to the systematic uncertainty of the results presented here:

- Neutrons, generated in the hydrogen target, that penetrate the shielding without interaction and directly hitting the neutron detector con-

tribute to about the same ToF window and give rise to accidental coincidences with a spectral shape as discussed in the previous section. These neutrons have to travel a slightly shorter way in the direct line-of-sight, they may not lose energy by scattering, but they are generated with less than 11 MeV due to the angular energy dependence of the production reaction.

- Inelastic reactions from neutron scattering on tungsten that lead to the absorption of the corresponding γ-photon in the central detector contribute to the spectra since the simultaneously detected nuclear recoil of tungsten emits much less light. Therefore, if the first nuclear level of ^{183}W (46 keV) is excited during de-excitation of higher-lying levels and all other gamma-rays escape the crystal, the simultaneous detection of this gamma together with the tungsten recoil leads to contributions in the energy range where elastic calcium recoils are expected, while the first excited levels of the even tungsten isotopes (100-123 keV) mainly contribute in the energy range of expected oxygen recoils (e.g., see Figure 3.4).

Both from cross section predictions of these reactions and the comparison of expected and measured recoil rates we find that these effects are small though not negligible. Figure 7.16 shows a combined spectrum from measurements at different angles by normalizing energies that are measured at one scattering angle to the appropriate oxygen recoil energy. The low energy part is discussed in the next chapter. The oxygen and calcium contributions are well separated and fit by a Gaussian distribution. The difference in cross sections and stoichiometric abundances lead to the high number of oxygen recoils (558) compared to calcium recoils (75) (cf. Table 7.5). The resolution of the light output of oxygen is equal to that expected from calibrations with gamma-ray sources, the resolution of the calcium peak is slightly worse than expected indicating a higher systematic uncertainty. The low-energy peak just above the detection threshold is discussed in Subsection 7.4.3.

7.4.3 Tungsten

Table 7.6 lists theoretically predicted event rates for elastic tungsten recoils at the different scattering angles under investigation. This number is always small, compared to the measured event rates at low energies, i.e. below the elastic calcium peak, except for the 80° angle. From the study of low energy events at different $CaWO_4$ trigger times ("walk") as displayed in Figure 7.13 (blue dots) we see that accidental coincidences are distributed quite homogeneously throughout the master acceptance window (trigger setup see

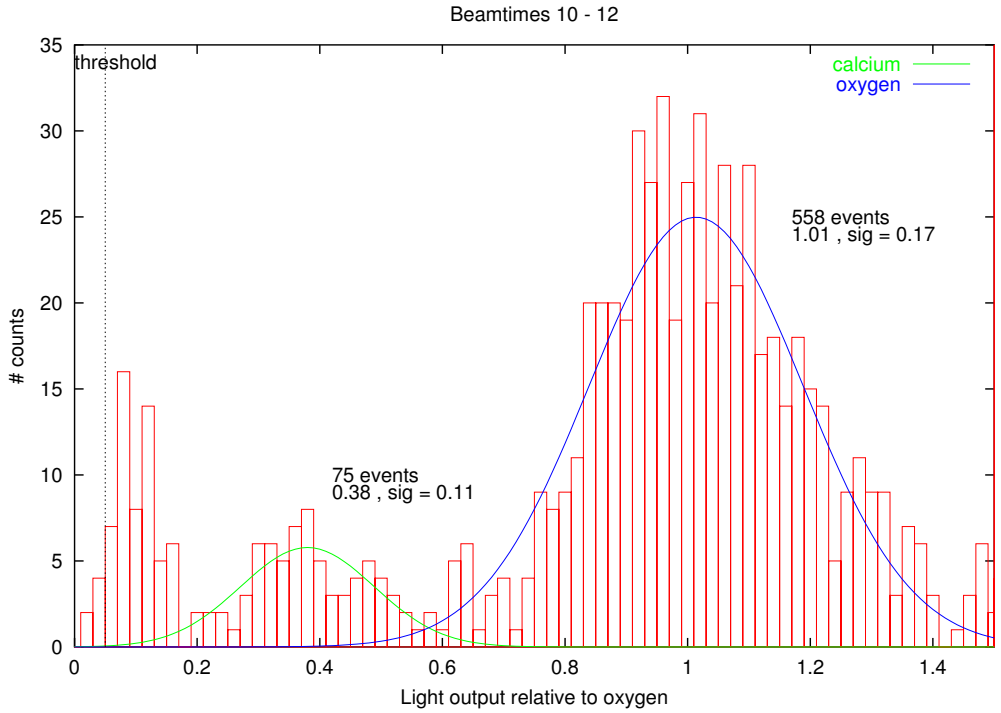

Figure 7.16: The $CaWO_4$ scintillator irradiated by neutrons from the hydrogen target. The results of the scattering angles between 100° and 140° were combined by normalizing to elastic oxygen recoils.

Subsection 6.5.4). It is clear that events that belong to the previous bunch cannot represent physically true coincidences. Events around the previous neighboring bunch within a walk-window of the same size as that of the central bunch serve for an estimation of the energy distribution of accidental coincidences in the central bunch. By subtracting their energy spectrum from the spectrum that was taken from the central bunch it is possible to account for this kind of background. This subtraction will be statistically significant if the number of background counts is of the same order as or smaller than the number of expected events.

An additional data reduction is provided if only coincidences between the two PMs viewing the central $CaWO_4$ crystal are considered. The measured numbers of events in Table 7.6 are given for coincidences of these two central PMs after the background subtraction described above for all scattering angles except 80°. The major drawback in requiring these coincidences is a higher threshold.

The investigation of low-energy events, without the requirement of coincidences between the two central PMs, reveals that their number is several

$d\sigma(W)/d\sigma(O)$ [%]	59	4.5	4.3	9.1	4.1
predicted number of events	27 ± 5	9 ± 3	8 ± 3	13 ± 4	4 ± 2
measured number of events	10 ± 5	8 ± 6	28 ± 9	16 ± 8	3 ± 3
QF [%]	< 3	< 6	< 9	< 6	< 8
	$80°$	$100°$ (b)	$108°$ (a)	$120°$ (b)	$140°$ (b)

Table 7.6: Predicted cross section ratios $d\sigma(W)/d\sigma(O)$ from Table 3.3, predicted and measured number of events for the specific observation angles (Lab-System) realized in various beamtimes. The uncertainty in the predicted number of events is due to the statistical uncertainty of the number of measured elastic oxygen recoils. The measured number of events at low energy is quoted after background subtraction (see text). The quoted uncertainty includes the statistical uncertainties of the number of background events and the residual number of events. (a) The measurement at 108° differs from the other measurements since no fast signal was recorded and hence no FPET could be evaluated. (b) The number of subtracted background counts was much higher than the residual number of counts.

times higher, after background subtraction, than predicted from cross-section ratios. These excess events have passed all previous cuts (except the central coincidence cut), i.e. they stem from neutrons that generate a signal in at least one of the central PMs within the right master trigger window and with appropriate ToF, without having scattered from tungsten nuclei. These events may be generated by the scattering of neutrons in the close vicinity of the $CaWO_4$ crystal, most likely in the photomultiplier glass window, giving rise to the emission of low-energy X-rays from the PM housing or scintillation light from the PM glass. There even might be an optical feedback between the two central PMs with or without the excitation of scintillation light by the $CaWO_4$ crystal. The analysis of signal pulse-shapes and PE distributions at low energies revealed no unambiguous identification of these events, so up to now there is no way to further subtract this kind of beam-correlated background.

While for all previous beamtimes, involving the scattering angles 100° to 140°, the total mass of the PM glass was several times higher than the mass of the $CaWO_4$ crystal, the measurement at 80° was performed using PMs with glass windows adapted to the crystal dimensions with a mass

comparable to that of the crystal. Furthermore the expected rate from elastic recoils of tungsten nuclei is an order of magnitude higher compared to the one at other scattering angles due to a local maximum in the cross-section. Although at 80° the recoil energy is smallest for all scattering angles realized in this experiment, the high number of predicted events combined with a considerable reduction of hits in the PM window allows the best limit in the determination of the Quenching factor of tungsten recoils (see Table 7.6). The quoted QF upper limit for tungsten does not depend on the predicted cross sections (taken from [23]), since the measured spectrum was evaluated without presetting the event rate. This is important to mention since [14] observe large deficits in the ^{127}I recoil count rates in NaI(Tl) in a similar neutron scattering setup.

7.4.4 Summary and Discussion

Table 7.7 summarizes the final results of the Quenching factors of O, Ca and W in $CaWO_4$ at room temperature in the quoted energy ranges. The high uncertainty in the Quenching factor of calcium may be due to a possible energy dependence (see Figure 7.15), i.e. a decrease of the Quenching factor with energy. As already mentioned, the systematic uncertainty is too high to pin down an energy dependence.

Neglecting for a moment the different energy ranges in which the Quenching factor has been measured, a trend of lower light yield with higher nuclear mass of the recoiling nucleus is suggested. This tendency is further supported by various observations done elsewhere in the CRESST collaboration:

- the direct bombardment of $CaWO_4$ crystals at room temperature with ions of different atomic mass shows Quenching factors which are fairly in agreement (Table 7.7), establishing a lower QF with higher atomic mass of the incident ion with high significance, while differences between QF_{bulk} and QF_{sf} may be due to the different energy range and the different location of recoil generation (a 15 nm penetration depth).

- in the temperature range of the CRESST $CaWO_4$ detectors, i.e. below 100 mK, protons have a QF of roughly 50-60% (measured with an Am-Be source via (n,p) reactions on Ca) , alpha-particles roughly 20% while oxygen recoils generated by neutron scattering show a QF of about 12% [7] (cf. Figure 2.1)

- heavy nuclei (e.g. ^{206}Pb) on the surface of $CaWO_4$ crystals, recoiling from α-decays, show below 100 mK a QF which is significantly lower than the oxygen QF [21], preliminarily about 2%

Element	QF_{bulk} [%]	Energy range	QF_{sf} [%]	Energy
oxygen	$\mathbf{7.8 \pm 0.3}$	1.0 – 2.2 MeV	7.0 ± 0.4	18 keV
calcium	$\mathbf{6.3 \pm 1.6}$	400 – 1000 keV	3.8 ± 0.3	18 keV
tungsten	$\mathbf{< 3.0\ (2\sigma)}$	100 – 200 keV	2.5 ± 0.2	18 keV

Table 7.7: Weighted average in percent of the Quenching Factors QF_{bulk} of oxygen, calcium and tungsten in $CaWO_4$ at room temperature in the quoted energy ranges, measured by neutron scattering. The weighting factors w_j are given by $w_j = \sigma_j^2/\sigma^2$, where $\sigma^{-2} = \sum_j \sigma_j^{-2}$ and σ_j are the uncertainties of the individual results from Tables 7.3 and 7.4. The quoted uncertainties for oxygen and calcium are the standard deviations of the individual results from Tables 7.3 and 7.4 neglecting a possible energy dependence. The Quenching factor of tungsten is taken from the 80° measurement and is valid for the quoted energy range if it does not depend on energy within this range. For comparison, the Quenching Factors QF_{sf} obtained from direct bombardment of ions with 18 keV energy at room temperature are also quoted [32].

- similar neutron scattering experiments that investigate scintillators composed of elements with distinctly different atomic masses show a similar dependency on the atomic mass, e.g. NE 213 [16] and NaI(Tl) [44].

Furthermore Birk's assumption on saturation effects at high specific energy depositions (Section 5.6) gives a qualitative explanation of this effect. While the total scintillation yield of nuclear recoils is neither simply proportional to the total ionization yield (cf. Figure 4.1) nor to the range of the ion cascade as predicted from Equation (5.5) (cf. Figure 4.2), a simple model of the mean longitudinal energy loss approximates the Quenching factors of calcium and tungsten in comparison to oxygen by the ratio of the total energy and the ion range (Table 4.4): if the mean oxygen energy loss of 1.2 keV/nm is referred to a Quenching factor of 7.8% (Table 7.7) and if the QF is inversely proportional to this energy loss, a QF of 5.9% for calcium and 2.0% for tungsten is predicted which is well within the uncertainty estimation of the measured Quenching factors.

Efforts are made towards a more detailed theoretical understanding of ion-induced luminescence which describe rather well the data in the range 10-100 MeV/A [27] where the energy loss to nuclear collisions is neglected. These models consider only an ionization column along the ion's track and assume the existence of a maximum energy density above which Quenching

dominates and the energy carrier density reaches a maximum constant value. Extensions of these models to lower energy ions (< 3 MeV/A) are published [8] but are still not capable of dealing with the complexity of interactions between the ion and the solid down to energies of interest for dark matter detectors.

Chapter 8

Summary and Outlook

A neutron scattering multidetector facility for the determination of the Quenching factor of detectors that use scintillation for direct WIMP searches has been set up. A well collimated monoenergetic neutron beam is obtained by using an inverse (p,n) reaction. The performance of this facility has been tested, and its capability to measure the Quenching factor of scintillation in NE 213 and NaI(Tl) has been proven. For the first time the Quenching factors at room temperature of oxygen, calcium and tungsten are measured separately within the bulk of $CaWO_4$ crystals which are currently used in the CRESST experiment.

In general, the Quenching of the light yield from nuclear recoils is a function of the recoil energy as well as of the temperature. It is well known that substances that show luminescence at room temperature exhibit a quenching of the luminescence at some higher temperature [22]. Vice versa, the efficiency increases as the temperature decreases (see Subsection 5.3.1), i.e. even many substances which are not luminescent at room temperature show this phenomenon at low temperatures. Unfortunately, few data are published concerning the temperature dependence of the Quenching factor of heavy ions (HI) in scintillators.

A survey of the HI Quenching dependence on recoil energy in many scintillators suggests a decrease down to the 10–100 keV recoil energy range followed by a re-increase at still lower recoil energies. This effect has been observed for, e.g., CsI(Tl) [51], CaF_2(Eu) [44], iodide at 100 keV and sodium at 10 keV in NaI(Tl) [44], carbon in NE 213 [16].

In summary, the lack of a reliable theoretical Quenching prediction emphasizes the need to measure the recoil Quenching Factor "in situ", i.e. with the same detector setup at the working temperature of this detector and with recoil energies expected from WIMP interaction. For this purpose, a dilution refrigerator from Oxford Instruments has been installed and is operated at

the experimental site in hall II of the MLL. The ^{3}He/^{4}He-mixture of this AST 50 refrigerator ("Advanced Sorption Technology") is pumped by two internal carbon sorption pumps with alternating pumping/recreation cycles with a cycle duration of about 20 minutes. Figure 8.1 shows the low-temperature insert.

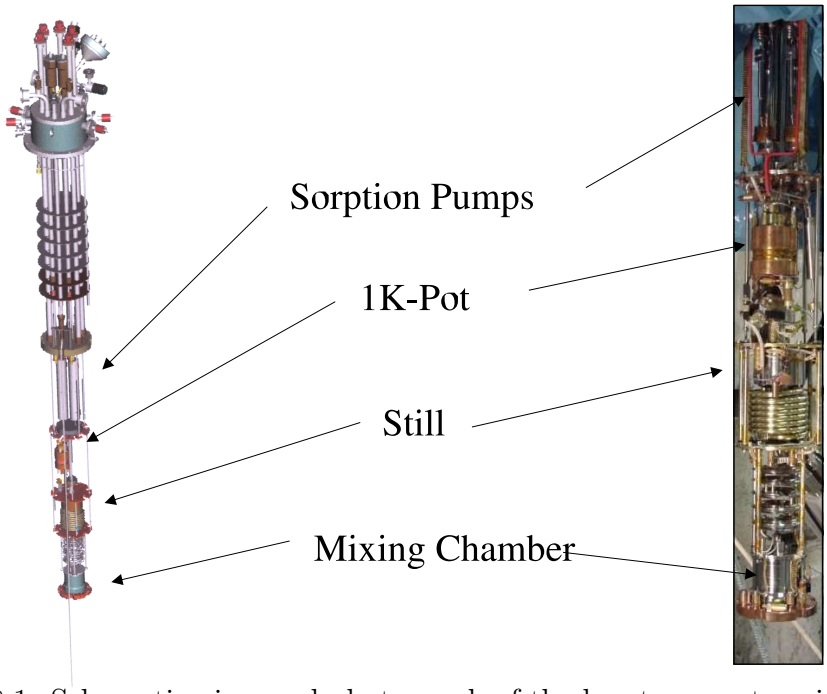

Figure 8.1: Schematic view and photograph of the low-temperature insert of an AST 50 refrigerator built by Oxford Instruments.

The advantage of the AST is the internal mixture circuit without the need of external gas handling. A serious drawback consists of mixing chamber temperature fluctuations of 5-10 % at 10 mK. The AST is completely controlled by computer via LabView programs. The extensive set of control parameters has been optimized, a dewar with reduced helium reservoir around the detector and a mobile suspension, isolated against vibrations, has been designed and mounted.

The rise of the scintillation decay time at low temperatures [22] will lead to even more sophisticated trigger conditions in the absence of a fast detector signal, and to lower reaction rates. The unavoidable installation of material, especially of Helium, in the vicinity of the detector will raise the number of accidental coincidences and multiple scattering events. On the other hand, the phonon energy will provide an additional cut to reject background events and identify elastic recoil events. The simultaneous measurement of the light

energy (see Chapter 2) will be a great advantage in providing the capability of neutron/gamma-discrimination in the central detector.

Appendix A

Kinematics

In the following sections we will discuss the correct relativistic kinematics which can easily be simplified to the classical Newtonian equations. This compilation of formulas will especially be useful for the discussion of the neutron generation and reaction cross sections. We restrict the treatise to two-particle reactions:

$$\mathrm{a}\,(p_1) + \mathrm{b}\,(p_2) \rightarrow \mathrm{c}\,(p_3) + \mathrm{d}\,(p_4) \tag{A.1}$$

where a, b, c, d are the names of the particles.

A.1 Energy, momentum and velocity

The particles (A.1) have got four-momenta [38], particularly useful for the collision treatment as each component of the total four-momentum is conserved and p_j^2 are invariants of the Lorentz transformation ($\mathbf{p}_j$ denotes the three-momentum and E_{0j} the rest energy of particle j):

$$p_1 = (E_1, ic\,\mathbf{p}_1) \qquad (c\,p_1)^2 = E_{01}^2 \quad \text{etc.} \tag{A.2}$$

For example, if we deal with neutrons (rest mass $E_0 = 940$ MeV) whose kinetic energy E_k is 11 MeV, this corresponds to a total energy E of

$$E = E_k + E_0, \tag{A.3}$$

$E = 951$ MeV. Thus the momentum $|\mathbf{p}|$ of these neutrons equals

$$c\,|\mathbf{p}| = \sqrt{E^2 - E_0^2} \tag{A.4}$$

which is 144 MeV/c. For comparison, this is in the order of the nuclear Fermi energy of 33 MeV and a nuclear Fermi momentum of 250 MeV/c, hence the

incoming neutron is about as fast as the bound nucleons. This condition favours the formation of a compound nucleus and disfavours direct reactions which dominate at higher impact energies.

For 11 MeV neutrons, the energy ratio γ, defined as

$$\gamma := \frac{E}{E_0} = \frac{1}{\sqrt{1-\beta^2}}, \tag{A.5}$$

equals $\gamma = 1.01$ and the velocity ratio β, defined as

$$\beta := \frac{v}{c} = \frac{\sqrt{\gamma^2-1}}{\gamma}, \tag{A.6}$$

is 15% of the speed of light ($c = 30$ cm/ns). Thus these neutrons are travelling with 4.5 cm/ns in the laboratory frame. γ also provides an estimation of the error of classical calculations which is in the range of one percent.

A.2 Center-of-mass System

Nuclear collisions are most easily derived in the center-of-mass system (CM system, CMS) whose energy and momentum are defined by their conservation:

$$p_{\mathrm{M}} = p_1 + p_2 = p_3 + p_4 \tag{A.7}$$

From these four-momenta two independent frame-invariant quantities can be derived, called Mandelstam variables:

$$s = c^2(p_1+p_2)^2 = c^2(p_3+p_4)^2 \tag{A.8}$$

$$t = c^2(p_1-p_3)^2 = c^2(p_2-p_4)^2 \tag{A.9}$$

t is the energy transfer squared, s is the total CMS energy squared, i.e. all kinetic and rest energies within the CMS.

From now on we will assume particle 2 to be initially at rest in the laboratory frame. Then

$$s = (E_{01}+E_{02})^2 + 2E_{02}E_{k1} \tag{A.10}$$

The velocity of the CM system is

$$V = \frac{|\mathbf{p}_{\mathrm{M}}|c^2}{E_{\mathrm{M}}}. \tag{A.11}$$

Then in a nonrelativistic calculation the kinetic energy of the CMS is given by

$$E_{k\mathrm{M}} = \frac{E_{01}E_{k1}}{E_{01}+E_{02}} \tag{A.12}$$

Energy and momentum are now transformed from the laboratory system into the CM system, their counterparts denoted by the shifted index (M). Lorentz transformations yield:

$$E_1^{(\mathrm{M})} = \frac{E_1E_{02}+E_{01}^2}{\sqrt{2E_1E_{02}+E_{01}^2+E_{02}^2}} \tag{A.13}$$

$$|\mathbf{p}_1^{(\mathrm{M})}| = |\mathbf{p}_2^{(\mathrm{M})}| = \frac{|\mathbf{p}_1|E_{02}}{\sqrt{2E_1E_{02}+E_{01}^2+E_{02}^2}} \tag{A.14}$$

The CMS momenta are particularly necessary for the evaluation of cross section data (Chapter 3). Their derivation may smartly be circumvented by directly using Mandelstam's parameters (Eqs. (A.8), (A.9)), exemplified by

$$s = E_{01}^2+E_{02}^2+2E_1E_{02} \tag{A.15}$$

$$t = E_{02}^2+E_{04}^2-2E_4E_{02} \tag{A.16}$$

In t, inelastic processes (Section A.4) are accounted for by incorporation of E_Q in E_{04}, see Eq. (A.24), as well as the dependence of E_4 on the scattering angle $\vartheta^{(\mathrm{M})}$.

A.3 Scattering angle

We define the expressions for γ_M and β_M in the same way as Eqs. (A.5) and (A.6), respectively, and furthermore the velocity ratio

$$\kappa_j = \frac{\beta_\mathrm{M}}{\beta_j^{(\mathrm{M})}} \tag{A.17}$$

Then the relationship between the scattering angle ϑ in the laboratory system and $\vartheta^{(\mathrm{M})}$ in the CM system is given by

$$\cos\vartheta_j^{(\mathrm{M})} = \frac{-\kappa_j\gamma_\mathrm{M}^2\tan^2\vartheta_j \pm \sqrt{1+(1-\kappa_j^2)\gamma_\mathrm{M}^2\tan^2\vartheta_j}}{1+\gamma_\mathrm{M}^2\tan^2\vartheta_j} \tag{A.18}$$

$$\tan\vartheta_j = \frac{\sin\vartheta_j^{(\mathrm{M})}}{\gamma_\mathrm{M}(\cos\vartheta_j^{(\mathrm{M})}+\kappa_j)} \tag{A.19}$$

The subscript j denotes the individual particle, all angles are defined with respect to the direction of the incident particle $\mathbf{e} = \mathbf{p}_1/|\mathbf{p}_1| = \mathbf{p}_\mathrm{M}/|\mathbf{p}_\mathrm{M}|$ (e.g. ϑ in Figure A.1). While for elastic collisions $|\mathbf{p}_1^{(\mathrm{M})}| = |\mathbf{p}_3^{(\mathrm{M})}|$, it is important to choose subscripts 3 or 4 for inelastic collisions since now $\kappa_1 \neq \kappa_3$ (see Eq. (A.17)).

From Eq. (A.18) an important feature of binary kinematics is revealed: If $\kappa_3 > 1$ two different solutions arise (for $\kappa_3 < 1$ only the positive sign holds for $\vartheta^{(\mathrm{M})} \in [0°; 180°]$) (see Section A.4). One example of $\kappa_3 > 1$ is elastic scattering under inverse kinematics ($E_{01} > E_{02}$, cf. Subsection 6.1.1), another example are endothermal reactions. More details will be given in Section A.4.

Nonrelativistically, κ_1 turns into the mass ratio k of the collision partners

$$k = \frac{E_{01}}{E_{02}} \tag{A.20}$$

and Eq. (A.18) simplifies for elastic collisions to

$$\cos\vartheta_j^{(\mathrm{M})} = -k\sin^2\vartheta_j \pm \cos\vartheta_j\sqrt{1-k^2\sin^2\vartheta_j} \tag{A.21}$$

For example, if $k = 1$, $\cos\vartheta^{(\mathrm{M})} = \cos 2\vartheta$ (same sign convention as for κ).

A.4 Two particle reaction

By using Eqs. (A.8) and (A.9), the energy of the reaction products in the laboratory frame can be expressed as

$$E_3 = \frac{s+t-E_{01}^2-E_{04}^2}{2E_{02}} \tag{A.22}$$

$$E_4 = \frac{E_{02}^2+E_{04}^2-t}{2E_{02}} \tag{A.23}$$

The energy E_Q of a reaction (Q-value) is defined as

$$E_Q = (E_{01} + E_{02}) - (E_{03} + E_{04}) = (E_{k3} + E_{k4}) - (E_{k1} + E_{k2}) \qquad \text{(A.24)}$$

Although the nonrelativistical expressions for E_3, E_4 turn out to be more complicated than the relativistic ones, focusing on nonrelativistic reactions with strong emphasis on endothermal reactions sheds light on the principal underlying process. Considering Figure A.1 which is drawn for the case $k > 1$, two velocities v_3 show up in the laboratory frame, observed under ϑ_3, where $v_3^{(M)}$ either adds to V or is subtracted from V (A.11). This is the case for any angle ϑ_3 where particles might be ejected. In this way two groups of particles with discrete energies will be observed. Further it is obvious that outside the cone with opening angle $\vartheta_{\max}$ no particles at all are observable in the laboratory frame. To investigate this further let us rewrite Eq. (A.22) in the classical approximation [25]:

$$\sqrt{E_{k3}} = r \pm \sqrt{r^2 + q} \qquad \text{(A.25)}$$

$$\text{given} \qquad r = \frac{\sqrt{m_1 m_3 E_{k1}}}{m_3 + m_4} \cos\vartheta \qquad \text{(A.26)}$$

$$\text{and} \qquad q = \frac{m_4 E_Q + E_{k1}(m_4 - m_1)}{m_3 + m_4} \qquad \text{(A.27)}$$

For a given negative Q-value and low enough E_{k1} the radicand in Eq. (A.25) gets negative. So at $\vartheta_3 = 0$ there is a threshold energy E_{th} where no particles are emitted for values of $E_{k1} \leq E_{\text{th}}$:

$$E_{\text{th}} = -Q \frac{m_3 + m_4}{m_3 + m_4 - m_1} \qquad \text{(A.28)}$$

The opening angle $\theta_{\max}$ can thus be described by

$$\sin^2 \vartheta_{\max} = \frac{m_2 m_4}{m_1 m_3} \left(1 - \frac{E_{\text{th}}}{E_{k1}}\right) \qquad \text{(A.29)}$$

From Figure A.1 for $\kappa < 1$ (Equation A.17) it is obvious that the relation between ϑ and $\vartheta^{(\text{M})}$ is one-to-one.

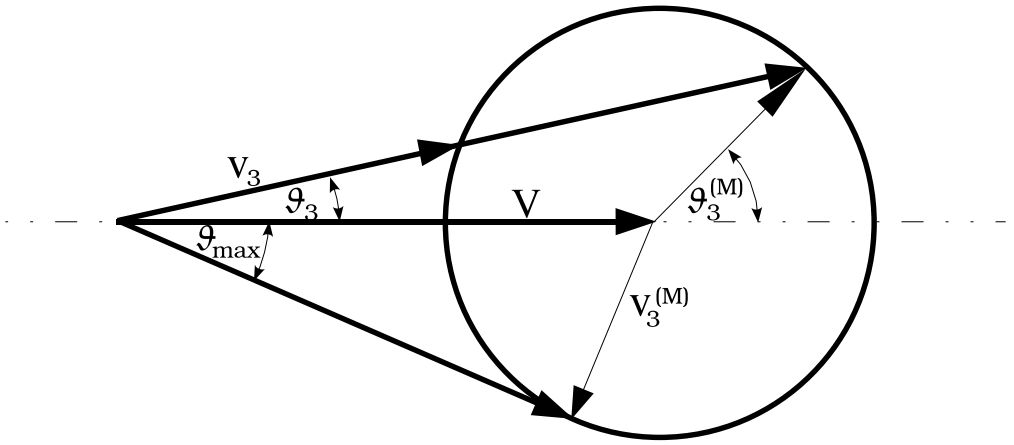

Figure A.1: Schematic nonrelativistic diagram of the velocity and angle relation between the CM and laboratory system for a kinematical condition $V > v_3^{(M)}$, where V denotes the velocity of the CM, and $v_3^{(M)}$ that of particle 3 (e.g. a produced neutron). The velocity of particle 3 in the laboratory frame is called v_3, i.e., $v_3 = V + v_3^{(M)}$. $\vartheta_3^{(\mathrm{M})}$ is the angle in the CMS of particle 3 relative to $\mathbf{V}$, and $\vartheta_{\max}$ is the maximum angle for particle 3 emission in the laboratory frame [5].

A.5 Elastic scattering

In the case of elastic scattering (A.22), (A.23) become:

$$E_3 = \frac{(E_1E_{02} + E_{01}^2)(E_1 + E_{02}) + E_{02}(E_1^2 - E_{01}^2)\cos\vartheta^{(\mathrm{M})}}{2E_1E_{02} + E_{01}^2 + E_{02}^2} \quad \text{(A.30)}$$

$$E_4 = E_{02}\left[1 + \frac{E_1^2 - E_{01}^2}{2E_1E_{02} + E_{01}^2 + E_{02}^2}(1 - \cos\vartheta^{(\mathrm{M})})\right] \quad \text{(A.31)}$$

The addend in (A.31) represents the recoil energy E_{R} of the struck particle, $\vartheta^{(\mathrm{M})}$ is the scattering angle in the CM system (Section A.3).

With the reduced mass

$$m_r\mathrm{c}^2 = \frac{E_{01}E_{02}}{E_{01} + E_{02}} \quad \text{(A.32)}$$

Eq. (A.31) simplifies in the non-relativistic case ($\gamma = 1$) to

$$E_{\mathrm{R}} = \beta^2\,\frac{m_r^2\mathrm{c}^4}{E_{02}}\,(1 - \cos\vartheta^{(\mathrm{M})}) \quad \text{(A.33)}$$

(Remember that $\vartheta^{(\mathrm{M})}$ is the scattering angle in the CMS, Eq.(A.18)). This equation describes the kinematics of the WIMP interaction (Section 1.5) as well as the kinematics of neutron scattering (Section 2.2) or the stopping of ions (Section 4.1).
Hence it follows that the maximum transferable energy for a head-on collision is given by

$$\Gamma = \frac{4E_{01}E_{02}}{(E_{01}+E_{02})^2} \tag{A.34}$$

If the projectile is a neutron or proton of rest mass u, Eq. (A.3) yields $E_{01} \approx \mathrm{uc}^2 + E_k$, and the maximum energy transfer to the target atom with $A \approx E_{02}/\mathrm{uc}^2$ can be written as

$$E_{\mathrm{R}}\Big|_{\max} = \frac{4A}{(1+A)^2}E_k \tag{A.35}$$

The maximum fractional energy transfer E_{R}/E_k decreases as the mass of the target nucleus increases.

In a scattering experiment with a continuous input spectrum (as e.g. discussed in Section 7.1) it is often necessary to calculate the input energy when only E_3 is measured. From Eq. (A.30) in the nonrelativistic case follows the inverse relation $E_1(E_3)$

$$E_{k3} = E_{k1} \cdot \frac{E_{01}^2 + E_{02}^2 + 2E_{01}E_{02}\cos\vartheta^{(\mathrm{M})}}{(E_{01}+E_{02})^2} \tag{A.36}$$

If the projectile is a photon with $E_1 = h\nu$ scattered by an electron $E_2 = m_e c^2$ (Compton scattering), then Eq.(A.31) in combination with Eq.(A.18) leads to

$$E_{k,e^-} = h\nu\left(\frac{(h\nu/m_e c^2)(1-\cos\vartheta)}{1+(h\nu/m_e c^2)(1-\cos\vartheta)}\right) \tag{A.37}$$

A head-on collision therefore leads to the Compton edge at

$$E_{k,e^-}\Big|_{\vartheta=\pi} = h\nu\left(\frac{2h\nu/m_e c^2}{1+2h\nu/m_e c^2}\right) \tag{A.38}$$

A.6 Solid angle and cross section

According to Eq. (6.7) also the solid angle $\mathrm{d}\Omega$ has to be transformed when changing between inertial frames, since

(1) the differential angles $\mathrm{d}\vartheta^{(\mathrm{M})}$ and $\mathrm{d}\vartheta$ are different in different frames,
(2) the radius of the altitude circle ($\sin\vartheta^{(\mathrm{M})}$) is different.

The solid angles transform as

$$\frac{\mathrm{d}\Omega}{\mathrm{d}\Omega^{(\mathrm{M})}} = \frac{\gamma_{\mathrm{M}}(1+\kappa\cos\vartheta^{(\mathrm{M})})}{(1-\cos^2\vartheta^{(\mathrm{M})}+\gamma_{\mathrm{M}}^2(\cos\Theta+\kappa)^2\,)^{3/2}} \tag{A.39}$$

Due to particle number conservation under system transformation similar equations hold for the cross sections

$$\frac{\mathrm{d}\sigma(\vartheta)}{\mathrm{d}\sigma(\vartheta^{(\mathrm{M})})} = \frac{\mathrm{d}\Omega^{(\mathrm{M})}}{\mathrm{d}\Omega} \tag{A.40}$$

Bibliography

[1] A. Alessandrello et al., *The thermal detection efficiency for recoils induced by low energy nuclear reactions, neutrinos or weakly interacting massive particles*, Physics Letters B **408** (1997), 465

[2] Amersham Buchler, *Technisches Bulletin 76/7*, (1979)

[3] R. Bernabei et.al., *Results from DAMA/NaI and perspectives for DAMA/LIBRA*, astro-ph/0311046

[4] J. B. Birks, *Scintillation Counters*, (1953)

[5] S. Chiba et. al., *The $^{1}H(^{11}B,n)^{11}C$ reaction as a practical low background monoenergetic neutron source in the 10 MeV region.*, NIM A **281** (1981), 581

[6] C. Cozzini, T. Jagemann, et al., *Detection of the natural alpha decay of tungsten*, nucl.-ex/0408006, submitted to Physical Review C

[7] G. Angloher et al., Limits on WIMP dark matter using scintillating $CaWO_4$ cryogenic detectors with active background suppression, astro-ph/0408006, submitted to Astroparticle Physics

[8] H.S. Cruz-Galindo, K. Michaelian, A. Martínez-Dávalos, E. Belmont-Moreno, S. Galindo, *Luminescence Model with quantum impact parameter for low energy ions*, NIM B **194** (2002), 319

[9] S.E. Derenzo, M.J. Weber, E. Bourret-Courchesne, M.K. Klintenberg, *The Quest for the Ideal Inorganic Scintillator*, NIM (2002)

[10] M. Drosg, *Novel monoenergetic neutron sources for energies between 2.5 and 25.7 MeV*, NIM A **254** (1987), 466

[11] M. Drosg, *1. Characteristics of accelerator based neutron sources – Monoenergetic neutron production by two-body reactions in the energy range from 0.0001 to 500 MeV*

[12] J. Ellis, R.A. Flores, Phys. Letters B **263** (1991), 259

[13] D. Errandonea, F. J. Manjón, M. Somayazulu, D. Häusermann, *Effects of pressure on the local atomic structure of $CaWO_4$ and $YLiF_4$: Mechanism of the scheelite-to-wolframite and scheelite-to-fergusonite transitions*

[14] J. Graichen, K. Maier, J. Schüth, A. Siepe, W. von Witsch, *Efficiency and directional effects in the detection of low-energy recoil nuclei in a NaI(Tl) single crystal*, NIM A **485** (2002), 774

[15] R.J. Gaitskell, *Direct Detection of Dark Matter*, Annu. Rev. Nucl. Part. Sci. **54** (2004), 315

[16] J. Hong, W. Craig, P. Graham, C. Hailey, N. Spooner, D. Tovey, *The scintillation efficiency of carbon and hydrogen recoils in an organic liquid scintillator for dark matter searches*, Astroparticle Physics **16** (2002), 333

[17] R. B. Firestone, *Table of Isotopes* (1996)

[18] R. Grasser, E. Pitt, A. Scharmann, G. Zimmerer, *Optical Properties of $CaWO_4$ and $CaMO_4$ Crystals in the 4 to 25 eV Region*, phys. stat. sol. (b) **69** (1975), 359

[19] S.F.A. Kettle, *Koordinationsverbindungen*, Physik Verlag (1969)

[20] G. F. Knoll, *Radiation Detection and Measurement*, Wiley (1989)

[21] J. König, Diploma thesis TU München (2004)

[22] F. A. Kröger, *Some aspects of the luminescence of solids*, Elsevier (1948)

[23] Los Alamos T-2 Nuclear Information Center, *http://t2.lanl.gov*

a) ENDF

(i) E. D. Arthur, *W-0 MAR82*, combined tungsten isotopic account for natural abundance, no direct contributions to inelastic scattering cross section

(ii) Arther, Young, Smith, Philis, *EVAL-DEC80 DIST-FEB90*, direct inelastic contributions for excitation of the first and second excited state

b) JENDL T. Watanabe, T. Asami, *KHI, NEDAC EVAL-MAR87*

[24] J. D. Lewin, P. F. Smith,, *Review of mathematics, numerical factors, and corrections for Dark Matter experiments based on elastic nuclear recoil.*, (1996)

[25] T. Mayer-Kuckuk, *Kernphysik*, Teubner 1994

[26] M. Y. Messous, *Calibration de détecteurs et recherche de matériaux luminescents pour la détection de la matière noire non bryonique*, Université Claude Bernard Lyon 1, Ph.D. thesis (1992)

[27] K. Michaelian, A. Menchaca-Rocha, *Model of ion-induced luminescence based on energy deposition by secondary electrons*, Physical Review B **49** Number 22 (1994), 15550

[28] V. Mürk, M. Nikl, E. Mihoková, K. Nitsch, *A study of electron excitations in $CaWO_4$ and $PbWO_4$ single crystals*, J. Phys.: Condens. Matter **9** (1997), 249

[29] G. Musiol, J.Ranft, R. Reif, D. Seeliger, *Kern- und Elementarteilchenphysik*, (1985)

[30] V. Nagirnyi et al., *Excitonic and recombination processes in $CaWO_4$ and $CdWO_4$ scintillators under synchrotron irradiation*, Radiation Measurements **29** (1998), 247

[31] M. Nikl et al., *Excitonic emission of scheelite tungstates AWO_4 (A = Pb, Ca, Ba, Sr)*, Journal of Luminescence **87-89** (2000), 1136

[32] J. Ninkovic, Max-Planck-Institut für Physik, Föhringer Ring 6, 80805 Munich, Germany, Ph.D. thesis (2004)

[33] V. Pankratov, L. Grigorjeva, D. Millers, S. Chernov, A.S. Voloshinovskii, *Luminescence center excited state absorption in tungstates*, Journal of Luminescence **94-95** (2001), 427

[34] C. Pastor, F. Benrachi, B. Chambon, D. Drain, *The Phostron: A Phoswich counter for neutron and charged particle detection*, Nuclear Instruments and Methods in Physics Research **227** (1984), 87

[35] B. Povh, Kl. Rith, Chr. Scholz, Fr. Zetsche, *Teilchen und Kerne* (1993)

[36] G. G. Raffelt, Proc. European School of High-Energy Physics, Menstrup (Denmark) (1997).

[37] L. Rohrer, H. Jakob, K. Rudolph, S.J. Skorka, *The Four Gap Double Drift Buncher at Munich*, NIM **220** (1984), 161

[38] E. Segrè, *Nuclei and Particles*, Berkeley (1980)

[39] E. Simon et al., *SICANE: a Detector Array for the Measurement of Nuclear Recoil Quenching Factors using a Monoenergetic Neutron Beam*, astro-ph/0212491 (2002)

[40] E. Simon, *Un multidétecteur pour l'étalonnage des bolomètres en énergie de recul par diffusion de neutrons dans le cadre de l'expérience EDELWEISS*, Université Claude Bernard Lyon 1, Ph.D. thesis (2001)

[41] D. Smith, R. Polk, T. Miller, *Measurement of the response of several organic scintillators to electrons, protons and deuterons*, Nuclear Instruments and Methods **64** (1968), 157

[42] M. Stark, Ph.D. thesis TU München (in preparation)

[43] P. Stassi, *Contribution à la mise au point du multidétecteur AMPHORA - Conception et réalisation de l'électronique*, Université Joseph Fourier Grenoble I, Ph.D. thesis (1989)

[44] D.R. Tovey, V. Kudryavtsev, M. Lehner, J.E. McMillan, C.D. Peak, J.W. Roberts, N.J.C. Spooner, J.D. Lewin, *Measurement of scintillation efficiencies and pulse-shapes for nuclear recoils in NaI(Tl) and CaF_2(Eu) at low energies for dark matter experiments*, Physics Letters B **433** (1998), 150

[45] M. J. Treadaway, R. C. Powell, *Luminescence of calcium tungstate crystals*, The Journal of Chemical Physics **61** No. 1 (1974), 4003

[46] SRIM Lab-2, http://www.srim.org, United States Naval Academy, Annapolis, MD, USA

[47] Y. Uwamino, K. Shin, M. Fujii, T. Nakamura, *Light output and response function of an NE-213 scintillator to neutrons up to 100 MeV*, Nuclear Instruments and Methods **204** (1982), 179

[48] S. Waller, *Monte Carlo Simulation der Energiedeposition hochenergetischer Neutronen in $CaWO_4$*, diploma thesis TU München (2002)

[49] W.v. Witsch, J.G. Willaschek, *High-pressure gas target for the production of intense fast-neutron beams*, Nuclear Instruments and Methods **138** (1979), 13

[50] L. A. Page, *The Wilkinson Microwave Anisotropy Probe*, Carnegie Observatories Astrophysics Series, Vol. 2: *Measuring and Modeling the Universe*, Cambridge **2003**

[51] Q. Yue, *Neutron Beam Test for Measuring Quenching Factor of CsI(Tl) Crystal*, IHEP, Beijing

[52] Y. Zhang, N. A. W. Holzwarth, R. T. Williams, *Electronic band structures of the scheelite materials $CaMoO_4$, $CaWO_4$, $PbMoO_4$, and $PbWO_4$*, Physical Review B **57** 20 (1998-II) 12738

[53] J. F. Ziegler, J. P. Biersack, U. Littmark, *The Stopping and Range of Ions in Solids*, Volume 1, Pergamon Press (1985)

[54] L. van der Zwan, K.W. Geiger, *The $^{11}B(p,n)^{11}C$ cross section from threshold to 4.9 MeV*, Nuclear Physics **A 306** (1978), 45

[55] F. Zwicky, Helv. Phys. Acta **6** (1933) 110.

Danksagung

Mein erster Dank gilt Prof. Dr. Franz von Feilitzsch für die Möglichkeit, diese interessante und vielseitige Arbeit anfertigen zu können. Sein Interesse am Fortschritt dieser Arbeit, die hervorragende freundliche Arbeitsatmosphäre am gesamten Institut, die charmante und gleichzeitig unbeirrbare Hartnäckigkeit im Umgang mit Firmen, die nicht rechtzeitig liefern (und das aus gutem Grund!) und der physikalische und physik-politische Weitblick werden mir immer in Erinnerung bleiben und als Vorbild dienen.

Dem geistigen Vater des Streuexperimentes, Prof. Dr. Josef Jochum, gebührt mein ganzer Respekt und Dank. Er ist der Initiator, Gesprächspartner, Ideengeber und Koordinator des gesamten Experimentes und dieser Arbeit. Seine Kompetenz, das theoretische und praktische Know-how, die Vielfalt an Ideen und Lösungsvorschlägen, gepaart mit einem unvergleichlichen Enthusiasmus und einer ansteckenden Freude am physikalischen Arbeiten nehmen es mit jedem Problem und experimentellen Rückschlag auf. Seine stete Freundlichkeit und sein Humor machen ihn in meinen Augen zum perfekten Doktorvater in den ersten drei Dimensionen (die vierte ist eine Problemdimension).

Für die sehr sorgfältige Durchsicht dieser Arbeit und die zahlreichen und wertvollen Tips, Anregungen und Kommentare bin ich besonders Dr. Walter Potzel und Dr. Wolfgang Rau dankbar, ebenso wie für ihre tatkräftige und kompetente Unterstützung in allen Aspekten des Streuexperimentes und darüber hinaus.

Weiterhin bin ich Prof. Dr. Lothar Oberauer und Prof. Dr. Eckehart Nolte für die beratende Begleitung dieser Arbeit dankbar.

Ohne Walter Carli, den Chef-Operateur am MLL, wäre dieses Beschleunigerexperiment irgendwo zwischen Bor-Pille und Cup2 Halle II stecken geblieben. Ein besonderer Dank an ihn für sein Engagement. Ebenso danke ich Hans Jakob für seinen persönlichen Einsatz und seine Hilfe in allen Fragen der Pulsung. Ohne ihn wäre eher ein unregelmäßiger Gleichstrom als ein sauberer Bunch am Experiment angekommen. Ebenso danke ich allen Operateuren, Mitarbeitern und der Werkstatt vom MLL.

Dr. Gunther Korschinek und Dr. Peter Thierolf haben mich in vielen Fragen zum Beschleuniger und damit verbundener Technik beraten. Ohne die Unterstützung von Hermann Hagn hätten unsere Messungen vermutlich niemals SPE-Sensitivität erreicht, vielen Dank für seine "magische" Unterstützung.

Allen Mitarbeitern unseres Instituts möchte ich danken für die Mithilfe bei nunmehr insgesamt ca. 130 Tagen Strahlzeit, in der sie in vielen Arbeitsschichten, Früh- und Spätschichten, mitgeholfen haben: Michael Stark, Dr. Michael Huber, Jean-Côme Lanfranchi, Tobias Lachenmaier, Dr. Hesti Wulandari, Ludwig Niedermeier, Doreen Wernicke, Dr. Marco Razetti, Christian Grieb, Christian Lendvai, Dr. Johann Schnagl, Stefan Waller, Klemens Rottler und allen beteiligten Werkstudenten.

Für die Beratung in allen Computerfragen danke ich insbesondere Dr. Marianne Göger-Neff und Wolfgang Westphal.

Je suis reconnaissant à Messieurs Bernard Chambon et Daniel Drain, professeurs à l'Université Claude Bernard, Lyon 1, pour leur aide, intérêt et me conseiller, ainsi que Melle Maryvonne De Jésus, Gilles Gerbier et Eric Simon.

Ich danke unseren Damen im Sekretariat, Beatrice van Bellen und Alexandra Füldner für die umsichtige Erledigung aller administrativen Mühseligkeiten.

Ein besonderer Dank an Erich Seitz und Harald Hess für die Ausführung der mechanischen Arbeiten.